AN ABSTRACT OF THE DISSERTATION OF

Daniel Jackson Ching for the degree of Doctor of Philosophy in Materials
Science presented on March 12, 2018.

Title: Developing a Methodology to Study the Effects of Adhesive Flow
Penetration on Wood Adhesive Bond Performance by using Micro X-ray
Computed Tomography (XCT) and Digital Volume Correlation (DVC)

Abstract approved:

_____

Frederick A. Kamke

Wood composites are an important renewable structural material which can be
a net carbon sink when used in combination with sustainable forest
management practices and high rates of log utilization. Adhesive bondlines are
an essential part of composites, and for wood composites, they determine the
moisture durability and mechanical performance of these products. This
dissertation is part of a decades long effort to understand how the properties of
the wood adhesive system influences the performance of wood composites.
Specifically, the relative importance of the shape of the cured adhesive *in situ* is
not well understood. Since adhesives are the most expensive part of wood
products by mass, insights into the performance of the wood adhesive system
could lead to cost savings of some kind. This dissertation describes the
methods for *in situ* mechanical loading and moisture induced swelling
experiments of wood composites using the combination of x-ray computed
tomography and digital volume correlation to make full field strain
measurements. Since this is the first time these methods have been applied to

study the wood composite system many suggestions for improved methods are made. Software tools were also created to assist with segmentation of wood adhesive bondlines and to simulate x-ray computed tomography data acquisition. These tools may assist in making future experiments better. The influence of adhesive flow on the mechanical performance of wood adhesive bonds is inconclusive either because specimen variability was too high or metrics for measuring bond performance insufficient. The local influence of adhesive bondlines on moisture induced swelling was measured for adhesives of different precure molecular weights, and no effect of the precure molecular weight was observed. However, it was observed that the wood and adhesive influence the moisture induced swelling of one another, and adhesive fracture during swelling may limit the ability of the adhesive to constrain wood swelling.

Developing a Methodology to Study the Effects of Adhesive Flow Penetration on
Wood Adhesive Bond Performance by using Micro X-ray Computed Tomography
(XCT) and Digital Volume Correlation (DVC)

by
Daniel Jackson Ching

A DISSERTATION

Submitted to

Oregon State University

in partial fulfillment of
the requirements for the
degree of

Doctor of Philosophy

Presented March 12, 2018
Commencement June 2018

Doctor of Philosophy dissertation of Daniel Jackson Ching presented on March 12, 2018.

APPROVED:

_____

Major Professor, representing Materials Science

_____

Director of the Materials Science Program

_____

Dean of the Graduate School

I understand that my dissertation will become part of the permanent collection of Oregon State University libraries. My signature below authorizes release of my dissertation to any reader upon request.

_____

Daniel Jackson Ching, Author

ACKNOWLEDGEMENTS

CONTRIBUTION OF AUTHORS

Brian Bay – Guidance in using digital volume correlation as a technique. Some advice about mechanics of materials.

Chuck Frihart – Planned moisture swelling experiments.

Warren Grigsby - Planned moisture swelling experiments.

Doğa Gürsoy – Thought of the XDesign concept. Applied for funding. Provided design input and feature requests. Proposed applications for XDesign. Interpreted beam coverage results. Contributed to XDesign source code.

Chris Hunt – Bonded brominated phenol formaldehyde loblolly pine specimens; Planned moisture swelling experiments.

Joseph Jakes – Collected XCT data for moisture swelling experiments. Designed moisture swelling experiments.

Frederick Kamke – Designed lap shear experiment. Applied for funding. Helped collect XCT data and interpret results.

Linda Lorenz – Synthesized brominated phenol formaldehyde; planned moisture swelling experiments.

Paige McKinley – Created some lap shear specimens; helped collect single lap data.

John Nairn – Provided FEA model software and advice on how to best interpret FEA model data. Helped design lap shear experiment. Provided advice on how to best implement MPM model in the appendix. Suggested future ways to improve and expand on that model.

Dan Yelle - Planned moisture swelling experiments.

Xianghui Xiao – Operates the 2BM beamline the Advanced Photon Source at Argonne National Laboratory. Set up the beamline for all x-ray experiments and assisted with data collection.

Michaela Zauner – Designed and constructed mechanical testing device for lap shear experiment. Helped collected single-lap XCT data

TABLE OF CONTENTS

TABLE OF CONTENTS (Continued)

TABLE OF CONTENTS (Continued)

TABLE OF CONTENTS (Continued)

TABLE OF CONTENTS (Continued)

LIST OF FIGURES

LIST OF FIGURES (Continued)

LIST OF FIGURES (Continued)

LIST OF FIGURES (Continued)

LIST OF TABLES

1   INTRODUCTION

1.1 Motivation

With contemporary concerns over the carbon foot print and life cycle assessment of buildings and construction, wood composites are renewable structural materials that have regained relevance as possible alternatives for low and mid-rise commercial, residential, or mixed-use buildings. Shams, Mahmud, and Al-Amin (2011) showed that switching to lumber, glass, and bricks from steel and concrete in the construction of a five-story building reduced the embodied energy by 52 %. Products like cross laminated timber and laminated veneer lumber could provide the structural members of these buildings with possible net carbon capture over their lifetimes. These products could eventually become entirely renewable if soy-based adhesives replace fossil derived ones and metal connections and fasteners are replaced with adhesive connections. However, major challenges to widespread adoption of wood-based materials for large scale construction exist in three main areas: moisture durability, mechanical load transfer, and fire resistance. Of these three issues, moisture durability and mechanical load transfer are directly related to the properties of the wood adhesive bonds which hold these products together.

The wood adhesive system which bonds together smaller pieces of wood into these larger engineered members is a key component of wood composite materials. However, the specifics of how these bonds function (the relative importance of various micro- and nano-scale adhesion mechanisms, for example) is uncertain, so developing reliable methods for studying how these systems behave is important for understanding how they fail and improving them for the future.

One key tool for investigating wood adhesive bond performance *in situ* is the combination of micro x-ray computed tomography (XCT) and digital volume correlation (DVC). Since no one has applied digital volume correlation to

investigate the wood adhesive interface before, it is important to try and establish good practices, set realistic expectations about what types of information can be extracted, and seek new insights (when possible) about the performance of adhesive bonds in wood composites.

1.2 Goals and Scope

The goal of this research was developing **methodology and tools** to study the effects of **adhesive flow and morphology** on wood adhesive **bond performance** using micro x-ray computed tomography (XCT) and digital volume correlation (DVC). In this context, m**ethodology** means the procedures followed to collect measurements and experimental setup, and **tools** means software tools developed to execute the procedures of the methodology or analyze and improve future methods. **Adhesive flow** means the micron-scale flow of adhesive across the surface of bond plane; into the lumens of tracheids, vessels, resin canals, and rays; and through pits and other openings. **Morphology** means the shape of the adhesive after curing as determined by adhesive flow and the formation of bubbles. **Bond performance** refers to two mechanisms: the shear load transfer across the bonded interface, and the way in which the interface responds to moisture-induced swelling. Neither of these two mechanisms have a quantitative descriptive metric.

In summary, we want to know if XCT and DVC can be used to determine the effect of adhesive flow on the mechanical performance of wood adhesive bond lines, what are some best practices for utilizing XCT and DVC with wood materials, and how might we improve these practices? To achieve this goal, the following objectives were set:

1. Determine the measurement uncertainty of digital volume correlation for micro x-ray computed tomography of wood adhesive bonds.

2. Determine the best data acquisition practices for x-ray computed tomography of wood adhesive bonds which is to be used for digital volume correlation.

3. Measure the effects of micro scale adhesive flow on the load transfer performance of wood adhesive bonds.

4. Measure the effects of micro scale adhesive flow on moisture swelling of wood adhesive bonds.

1.3 Dissertation Structure

To achieve these objectives, a series of works were completed. First, in Chapter 2, the literature is reviewed. Then, in Chapter 3, "Methodology for comparing wood adhesive bondline load transfer using digital volume correlation", the expected measurement uncertainty of DVC in wood textures is estimated for objective 1. Then there is discussion of some sources of uncertainty and error which may be reduced in future experiments to address objective 2. Finally, an attempt to quantify the load transfer performance and relate it to the adhesive morphology is made to address objective 3. Quantifying the load transfer performance of the adhesive bonds is also discussed in the appendix. Next, in Chapter 4, "X-ray computed tomography observations of Moisture swelling in wood adhesive bondlines", the effects of moisture swelling are discussed for objective 4.

Chapters 5 and 6, "XDesign: an open-source software package for designing x-ray imaging phantoms" and "The effect of procedure coverage on tomographic reconstruction quality of scanning probe microscopy" describe the development and utilization of a computed tomography simulation tool which may lead to better choices of scanning and reconstruction parameters for x-ray computer tomography of wood composites; this is related to objective 2.

2   LITERATURE REVIEW

2.1 Wood Composite Structure

2.1.1 Wood anatomy

Wood is a hierarchical structure mostly composed of cellulose, hemicelluloses, and lignin. The present work concerns mechanisms involving micron scale structures and morphology which corresponds to the cellular and cell wall scales of Figure 2.1. At this scale, cells whose longitudinal (vertical axis of the tree) length is on the order of millimeters, whereas the radial and tangential dimensions are 10s of microns. Ray cells, which run perpendicular to the longitudinal direction (radial direction), and small micron-size openings called pits, connect neighboring cells to each other are visible in Figure 2.2. In softwood species, most of the longitudinal cells are tracheids, which are 3 to 4 millimeters in length and have a layered cell wall. Tracheids are arranged into growth rings, which are groups of cells with either thick or thin cell walls caused by seasonal growing changes. Regions of thin-walled tracheids are called earlywood, and regions of thick-walled tracheids are called latewood. For a good resource on wood anatomy, the reader is referred to (Hoadley 1990).

2.1.2 Adhesives

Important adhesive systems for wood composite products include formaldehyde-based aqueous adhesives, such as urea-formaldehyde (UF), melamine-formaldehyde (MF), and phenol-formaldehyde (PF). An important nonpolar resin system is polymeric methylene-diphenyl-diisocyanate (pMDI), which is composed of 100% adhesive solids. Another common adhesive for bonding wood is a water-based emulsion of polyvinyl acetate (Stoeckel, Konnerth, and Gindl-Altmutter 2013). Each of these adhesives have unique fluid properties and interact physically and chemically with wood in distinctly different ways.

2.1.3 Adhesion mechanisms

When two pieces of wood are adhered, the boundary may be any combination of earlywood and latewood. The adhesive may flow into the wood cell material flowing through pits or cut openings into cell lumens (empty space in the center of tracheids and ray cells) or it may diffuse directly into cell walls at the molecular level. These two mechanisms for penetration are called adhesive flow and adhesive infiltration, respectively.

Three main adhesion mechanisms exist: mechanical interlocking, covalent bonding, and secondary electrostatic forces. Of these, secondary electrostatic forces are the dominant mechanism (Kamke and Lee 2007). Adhesive flow should influence all three main adhesion mechanisms because it determines the amount of bonding surface area and the mechanical interlocking of the bond.

2.2 X-ray computed tomography

X-ray computed tomography (XCT) is a method by which an image volume is reconstructed from a series of two-dimensional projections through the volume. Briefly, by taking a series of x-ray images (radiographs) from different views around the outside of a specimen, the inside structure of the specimen can be estimated from the unique information that each view provides Figure 2.3. In the case of XCT, this information is mainly x-ray attenuation information, but sometimes diffraction, scattering, and florescence information may also be used.

For a detailed primer about the application of XCT to microstructural and mechanical studies, the reader is referred to (Ketcham and Carlson 2001; Sause 2016).

2.2.1 Preprocessing methods

Image distortions (Figure 2.4) may appear in the reconstructed images because of various reasons (Boas and Fleischmann 2012). Ring removal and

phase reconstruction are two pre-reconstruction algorithms which are used to mitigate some of these distortions.

A miscalibrated x-ray detector with pixels that are more sensitive or less sensitive than average may cause rings of incorrectly high and low brightness appearing in the reconstructed image around the rotation axis of the specimen. A popular ring removal algorithm uses wavelets to remove frequencies containing the rings from the Fourier transform of the sinogram (Münch et al. 2009).

Phase contrast x-ray imaging is a method which artificially improves image contrast between materials of different attenuations. Because light will change phase when crossing the interfaces of two materials with different refractive indices, the phase of x-rays becomes unsynchronized while passing through the specimen. If the x-ray detector is far enough from the specimen, then interference between x-rays will appear as periodic intensity variations on the detector. Either the detector can be moved closer to the specimen to prevent wave interference or the interference may be used to artificially boost the apparent contrast between materials in the reconstructed image.

2.2.2 Reconstruction Methods

Recently there have been two initiatives to enable researchers to easily use and modify various tomographic reconstruction algorithms and preprocessing methods. These include TomoPy (Gürsoy et al. 2014) and the ASTRA toolbox (Pelt et al. 2016). The reconstruction methods available in these tools fall into two categories: back projection and iterative methods.

Filtered back projection (FBP) and gridrec (Marone and Stampanoni 2012) are two back projection methods. These methods reconstruct the image by adding the result of smearing all 2D projections back across the volume (Figure 2.3). These algorithms are simpler and faster, but less accurate than iterative methods. Iterative reconstruction methods, such as algebraic reconstruction

technique (ART) (Gordon, Bender, and Herman 1970), simultaneous iterative reconstruction technique (SIRT) (Gilbert 1972), etc. use an internal model of the field of view and iterate through each 2D projection while updating the model so it agrees with the 2D projections. The disadvantage of iterative algorithms is that they are slower, but they have a reduced sensitivity to noise compared with back projection methods.

The reader is referred to Chapter 25 of Strauss (2000) for a more detailed discussion of reconstruction methods.

2.2.3 Simulated X-ray Computed Tomography

Models and simulated experiments are useful tools for developing novel imaging techniques (e.g. the setup, properties, and movement of the detector and light source) at lower cost. Some open-source software tools for simulating non-X-ray imaging systems include GATE (Jan et al. 2004), STIR (Thielemans et al. 2012), and k-Wave (Treeby and Cox 2010). There are also open-source tools that focus on developing and making accessible new reconstruction methods: TXM wizard (Liu et al. 2012), MMX-I (Bergamaschi et al. 2016), ASTRA (van Aarle et al. 2015) and TomoPy (Gürsoy et al. 2014).

2.2.4 Reconstruction Quality Measures

There are three classes of image quality metrics: full reference, partial reference, and no reference. Full reference metrics measure the amount of shared information between a reference and distorted image. The importance of different types of information: edge intensity, color, contrast is weighted differently in various methods, and the result is only applicable to a particular image. Partial reference metrics are used when the full reference exists but is not reliably accessible. No reference methods often try to measure the highest resolvable frequency or noise content of an image capturing system by using a

standard test pattern; these quantities are believed to predict the quality of all images captured by a system.

2.2.4.1 No Reference Image Quality Metrics

The current most-popular type of quality metrics for developers and users of x-ray computed tomography is no reference. This type of metric includes, noise power spectra, spatial frequency response, modulation transfer function, estimates of the signal to noise ratio, and subjective image quality. Sometimes a physical standard with a special pattern is used to help calculate these metrics.

Noise power spectra (NPS) use a Fourier transform of uniform area in the reconstruction to give information about the frequency composition of the noise. This approach is better than signal to noise ratio (SNR) because NPS assesses the degree of coarse or fine noise. 2D images produce a 2D noise power spectrum, but the 2D spectrum can be reduced to a histogram by binning radially. Figure 2.6 shows the NPS for the reconstructed image in Figure 2.5.

Spatial frequency response (SFR) and modulation transfer function (MTF) commonly use a slanted edge or standard pattern of lines at increasingly smaller intervals to measure how the fidelity of an image decreases as the frequency of a signal increases. The ability of an imaging system to accurately capture high frequency signals is related to the sharpness of images it creates. Figure 2.8 shows the MTF curve for the image in Figure 2.5.

2.2.5 Full and Partial Reference Image Quality Metrics

Full and partial reference metrics are currently unused by developers and users of x-ray computed tomography because they require a ground truth for comparison. These metrics, developed by the computer vision community, are convolution-based metrics originally used for comparing images to their

originals after transmission or compression. Popular full reference metrics include MS-SSIM, FSIM, and VIF. For an example of a reference and distorted image pair qualified by a full reference metric, see Figure 2.7 and Figure 5.8.

The multiscale structural similarity index (MS-SSIM) measures differences in "luminance, contrast, and structure" at multiple levels of detail (Wang, Simoncelli, and Bovik 2003). Each of these three qualities is calculated from a combination of the local mean, standard deviation, and covariance of images. Using local means and standard deviations calculated from Gaussian filters, it is possible to calculate a contour map of image quality at multiple resolution scales. Similarity overall is calculated by averaging the structural similarity index over the entire image and at each scale.

The feature similarity index (FSIM) measures the similarity of images using gradient magnitude and Fourier phase congruency (Zhang et al. 2011). Because high phase congruency had been correlated with image features important to the human visual system (HVS), this method weights the importance of each gradient magnitude depending on phase congruency. Since the gradient magnitude is only a measure of edges, this method ignores whether luminance is correctly captured, but that might not be important for some users.

The visual information fidelity in the pixel domain (VIFp) measures shared information between a reference and distorted image using a framework based on natural scene statistics (Sheikh and Bovik 2006). It uses Gaussian scale mixtures and wavelet analysis. It directly compares the intensity information in the images at different scales by separating it into levels using Gaussian filters of different sizes. Because it uses wavelets, the accuracy of this quality metric is dependent on the depth of the wavelet transform.

2.3 Multi-phase segmentation

Multi-phase segmentation seems to be a neglected topic because most algorithms only address two-phase segmentation. However, the soil sciences community has much experience segmenting multi-phase systems in the study of oil, water, soil, air systems. A comprehensive guide to segmented multi-phase XCT was published by (Schlüter et al. 2014). They suggest a workflow for segmentation and use oil, water, and soil mixtures to show the effects of various segmentation methods on the topology of the segmented volumes.

One of the preliminary steps of most image processing is noise reduction. The idea that median filtering is somehow exempt from the edge destroying effects that linear filters exhibit seems to plague the science community; however, as (Arias-Castro and Donoho 2009) show, this idea is false, and median filters are only comparatively more edge preserving than linear filters if they are used iteratively at multiple scales.

2.3.1 Tagged-Adhesives

Typical wood adhesives, e.g. phenol-formaldehyde and polymeric methylene-diphenyl-diisocyanate, do not provide enough x-ray attenuation contrast to be segmented from the main constituents of wood, cellulose and lignin, in x-ray images. Special adhesives tagged with iodine were developed by (Paris, Kamke, and Xiao 2015) to improve the contrast between the adhesive and the wood cells.

2.3.2 Measuring Adhesive Penetration and Morphology

Visible light microscopy and electron microscopy have been used for serial sectioning of adhesive bond planes; however, the disadvantage of serial sectioning is that it is destructive. Instead, X-ray computed tomography may be used for non-destructive imaging of adhesive bond planes in 3D.

Others have used x-ray computed tomography to investigate wood anatomy, but (Kamke et al. 2014) was the first to use two metrics, EP and WP, to quantify adhesive penetration. These two metrics are defined in Equations 2-1 and 2-2.

$$EP = \frac{\sum A_i}{X_{image}} \qquad \text{2-1}$$

$$WP = \sqrt{\frac{\sum Y_i^2 A_i}{\sum A_i}} \qquad \text{2-2}$$

Where A_i is the volume of a given adhesive object, X_{image} is the width of the image, and Y_i is the perpendicular distance from the centroid of an adhesive object to the bond plane. EP is the local planar density of adhesive and should ideally match the applied density of adhesive if there is no cell wall penetration, squeeze out, or other source of adhesive volume loss. WP is a measure of how far the adhesive has travelled from the bond plane. Both EP and WP are applied to 2D images, where the bondline is oriented horizontally across the width of the image.

(Kamke et al. 2014) showed statistical agreement between adhesive penetration measured with 2D cross- sections and 3D tomography. Their data showed the expected differences between PF and pMDI adhesive penetration and was also able to capture effects not visible in 2D, such as adhesive bubbles, adhesive traversing cell lumens and rays that intersect the bond plane, and adhesive cracking that occurred during curing.

2.4 Digital Volume Correlation

First reported by (Bay et al. 1999), digital volume correlation (DVC) is the 3D extension of digital image correlation (DIC). Originally developed for studying trabecular bone, it has since been adopted in other fields, in materials science such as geology and composite materials. In DVC and DIC, points in a reference image are matched with points in a deformed image by comparing

information in the correlation window, the region surrounding each point. Correlating points between images of the same object at different states of deformation shows how the object deformed. This displacement field can then be used to calculate strain fields and other quantitative measures of deformation.

For a review of in-situ testing of materials using x-ray computed tomography (XCT), the reader is referred to (Sause 2016).

2.4.1 Digital Volume Correlation Implementation Details

Most DVC algorithms perform subvolume matching of some kind. Recommendations for optimizing this process can be found in the dissertation by (Gates, Lambros, and Heath 2011). However, there are two other methods which have also been developed. Fourier based DVC performs global optimization on the entire volume in Fourier space (Bar-Kochba et al. 2015). Finite element based DVC uses a finite element mesh to regularize the computed displacement field (Leclerc et al. 2011).

2.4.2 Uncertainty Quantification

Correlation between volumes (or images) requires features or texture i.e. varying colors across the volume that provides each point with a unique neighborhood. According to (Estrada and Franck 2015) "Denser, more gray-valued speckle patterns generally correlate better, providing higher spatial displacement resolution and sensitivity compared to repeat patterns or large areas of constant intensity". The precision of DVC is determined by the size of the features in the texture and the size of the correlation window. In the case of DIC, surfaces may be artificially patterned to meet these requirements, but for DVC, existing natural texture must be used for correlation. Larger correlation windows give lower uncertainty with lower spatial resolution and smaller correlation windows can resolve higher frequency displacements but with

higher uncertainty according to the well-known power law relationship between correlation window size and measurement uncertainty (Bornert et al. 2009; Reu et al. 2009; Leclerc et al. 2011). Previous works which have characterized the effects of texture and correlation parameters are summarized by (Roberts, Perilli, and Reynolds 2014).

Ring artifacts, which cause false rotation to be measured, and thermal expansion of lab scale x-ray sources, which causes false translation and or expansion to be measured (Pan 2013; Limodin et al. 2011) are also sources of uncertainty. A method for mitigating reconstruction artifacts due to sample movement between projections of the same scan has also been suggested (Sasov, Liu, and Salmon 2008); though it does not tie back to image correlation. There have been no previous works about the effect of reconstruction method choice on correlation uncertainty.

There are two popular techniques for quantifying the uncertainty associated with image correlation experiments. First, simulated deformations on actual or artificial textures are used for quantifying bias and uncertainty from the correlation algorithm itself. (Palanca et al. 2015) used this method to compare various DVC algorithms on XCT of bone and showed that coupling DVC with finite element methods reduces uncertainty by an order of magnitude compared to direct matching and FFT methods. (Pan 2013) used this method to show that low pass filtering can reduce interpolation bias. Second, a noise floor from multiple images of a static object or one that has been displaced by a known vector (Reu et al. 2009; Gillard et al. 2014) is used to quantify uncertainty from other sources such as detector and sample motion, detector noise, image artifacts, etc. (Bornert et al. 2009; Reu et al. 2009; Reu 2013). (Tozzi et al. 2017) used this method to show that local structural changes influence the measurement uncertainty for bone.

2.4.3 Previous studies of anisotropic, cellular, or composite materials

There have been a few studies of cellular and composite materials using digital volume correlation, but none of them have been in tension along the fiber direction (Brault et al. 2013; Tran et al. 2013; Germaneau, Doumalin, and Dupré 2008). Two studies using digital volume correlation or affine registration to study wood are Forsberg et al. (2010) and Derome et al. (2011). Forsberg et al. (2010) showed that wood structures could be correlated perpendicular to the grain in a three-point bending experiment. They noted "anomalous deformation patterns [that] can be traced back to the wood structure." Derome et al. (2011) also showed correlations perpendicular to the grain in hysteretic moisture swelling experiments. A summary of reported scanning resolutions and measurement uncertainties for these studies is shown in Table 2.1.

(Zauner et al. 2012) developed a mechanical testing device (also used in this study) for step loading of wood in compression without blocking the detector in a beamline. However, the collected images were only used qualitatively. In a related study, (Zauner and Niemz 2014) investigated potential size effects on the strength of wood by compressing *Picea abies* specimens of four different sizes while making surface measurements using DIC.

(Kamke et al. 2014) outlined a methodology for integrating computational modeling and experimental data for investigating the effect of adhesive penetration and morphology on bond strength. As part of this proposed methodology, (Matthew Schwarzkopf and Muszyński 2015) collected surface DIC data of lap shear specimens for validation of computational models based on static XCT images of the same bond planes.

(Baensch 2015) has also conducted step loaded tensile tests of two-layer composites of *Picea abies*. However, quantitative measurement was conducted using acoustic emission and the focus of the study was crack propagation not the influence of adhesive morphology.

2.5 Visualization of Multidimensional Data

Visualizing tensor data in a two or three-dimensional space is extremely challenging, but there has been some work in recent years for medical and engineering visualization.

2.5.1 Glyphs

Glyphs are geometric tokens whose shape, color, scale, and/or orientation change according to variables in a data set. In Figure 2.9, and example is shown of colored elliptical glyphs. In this example, these glyphs could represent the relative magnitude and direction of the Eigenvalues of a 2 by 2 matrix. Starting in the upper left, both values are positive, but one becomes decreases in magnitude. In the middle row, one value becomes negative. In the middle of the middle row, the eigenvalues are equal and opposite. At the bottom right, the values are both negative and have the same magnitude.

Glyphs are useful because they can convey multiple parameters from a dataset simultaneously. (Ropinski, Oeltze, and Preim 2011) suggest six best practices when using glyphs:

- Parameter mapping functions should visually emphasize important variables, incorporate the range of values, guide the user's focus of attention to encode relevance, incorporate semantics of the data, be mentally reconstructable based on visualization
- Glyph placement should be well-balanced and avoid unwanted glyph aggregations in image space, e.g. by applying jittering or relaxation procedures
- Glyph shapes should be unambiguously perceivable and independent of viewing direction
- Glyph visualizations should support quantitative analysis in the attentive phase.

- Hybrid visualization should be exploited to provide anatomical context
- When using glyph size to convey information, perspective projection should be avoided.

Various glyph shapes have been proposed, so choosing the best one depends on the application. (Hashash, Yao, and Wotring 2003) summarize five different types of glyphs and discuss their advantages and weaknesses.

2.5.2 Color Usage

There are optimal color scales for representing data in color. According to (Levkowitz and Herman 1992) optimal color scales maximize the number of noticeably different colors. To do this, the color scale should have a constant saturation and progress from a given color to the color 180 degrees away in hue (complementary colors in the RGB model). While grayscale outperformed their optimal color scale, the authors suspect that may not have been true for different background colors. Additionally, viewers may have trouble distinguishing between green and red (color blindness), or they may be printing images in grayscale. Color scales which consider all these factors are called perceptually uniform. There are many free to use perceptually uniform color maps available through Matplotlib (Hunter 2007), and other sources.

2.6 Tables

Table 2.1 Reported measurement uncertainty and scanning resolutions for previous mechanical studies of cellular and anisotropic materials

Author	Material	Uncertainty (voxels)	Scanning Resolution
(Brault et al. 2013)	carbon fiber composite	0.04	52 μm/voxel
(Tran et al. 2013)	wood fiberboard	not given	18 μm/voxel
(Germaneau, Doumalin, and Dupré 2008)	copper particles in polymer	0.049, 0.037	60 μm/voxel
(Derome et al. 2011)	wood	not given	0.7 μm/voxel
(Forsberg et al. 2010)	wood	0.0346, 0.0937	1.75 and 3.5 μm/voxel

2.7 Figures

Figure 2.1 The hierarchical structure of wood from macroscale to nanoscale. Taken from Dufresne (2013) without permission.
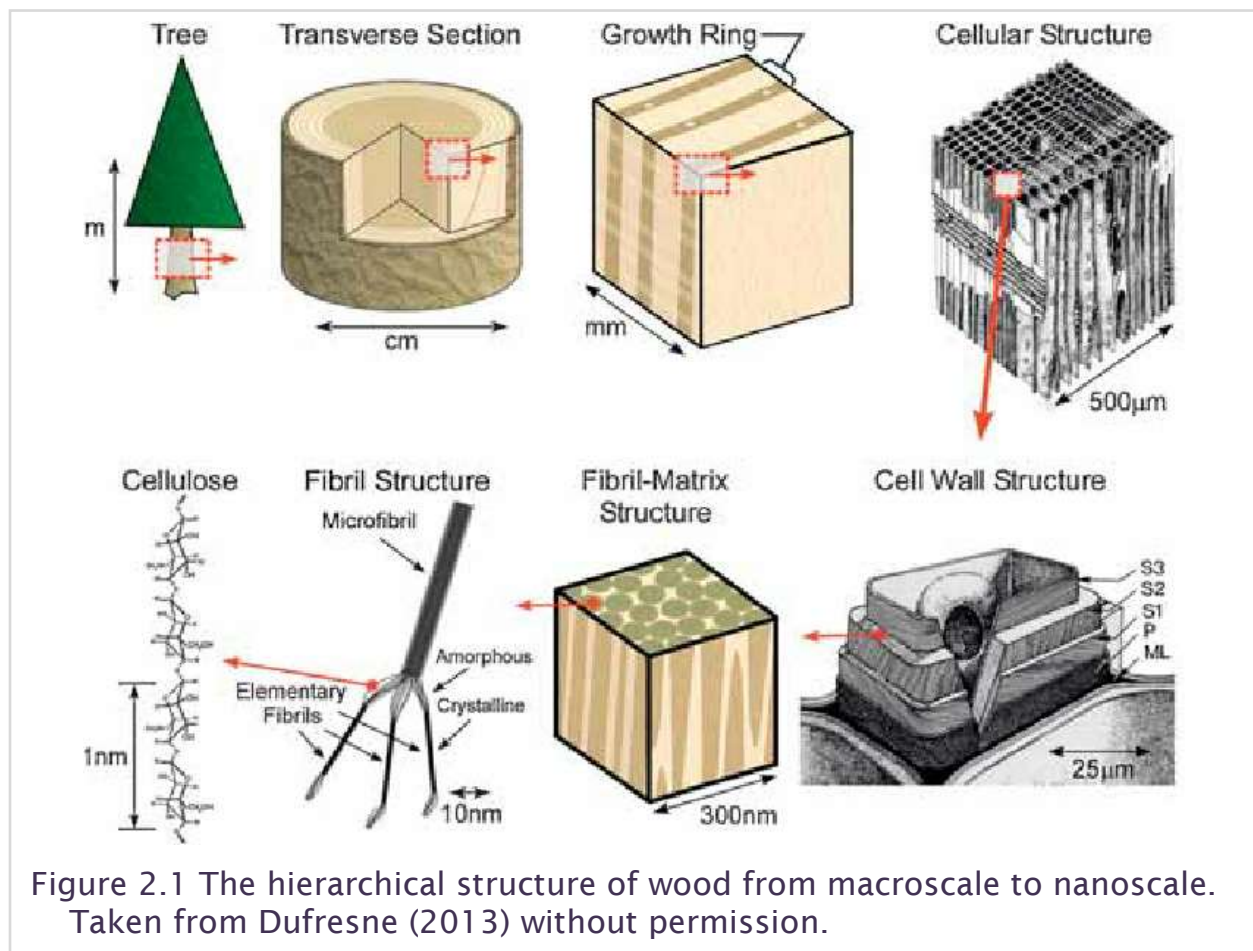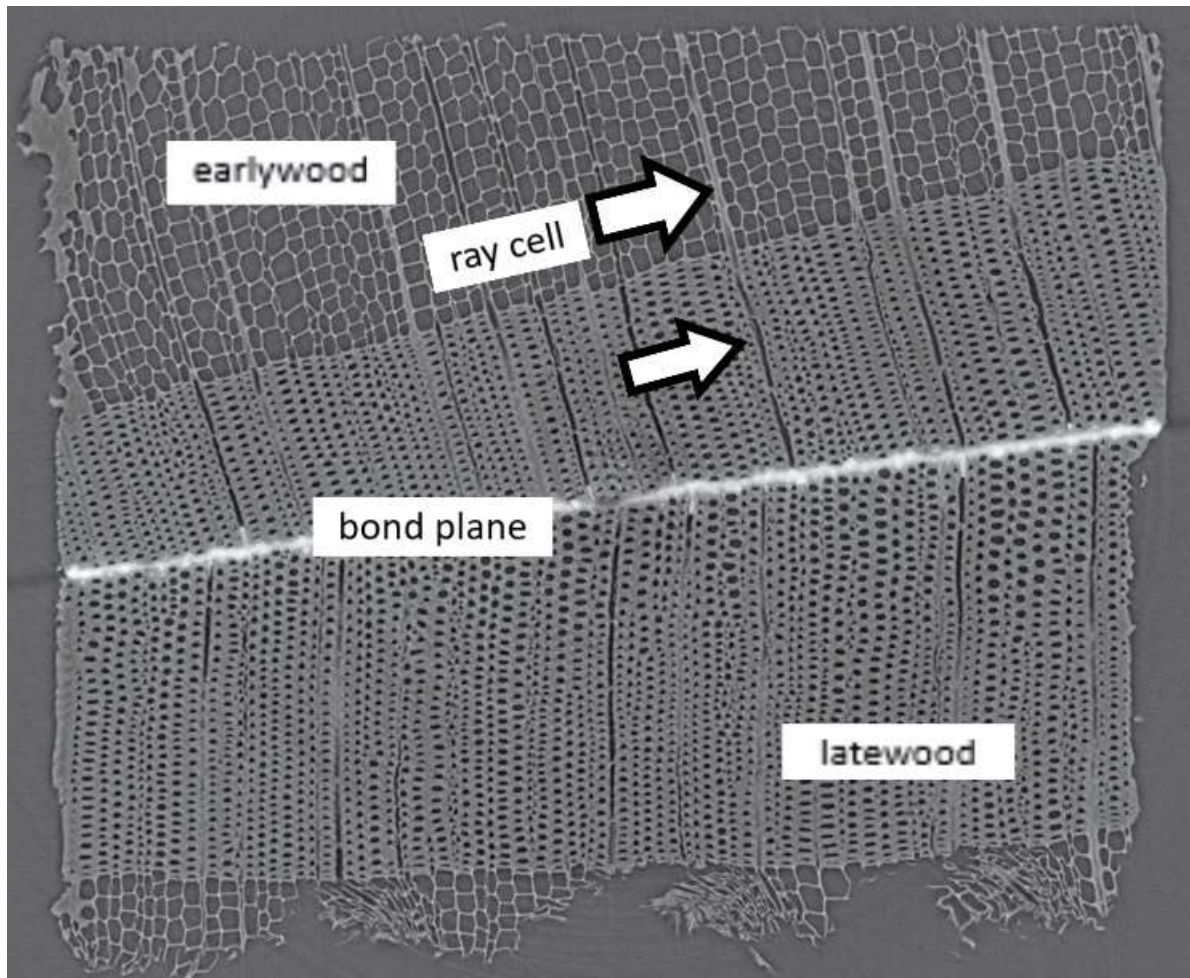
Figure 2.2 Cross section of latewood-latewood Douglas-fir bond plane.

Figure 2.3 Figure from (Strauss 2000) showing how multiple views can reconstruct an image.
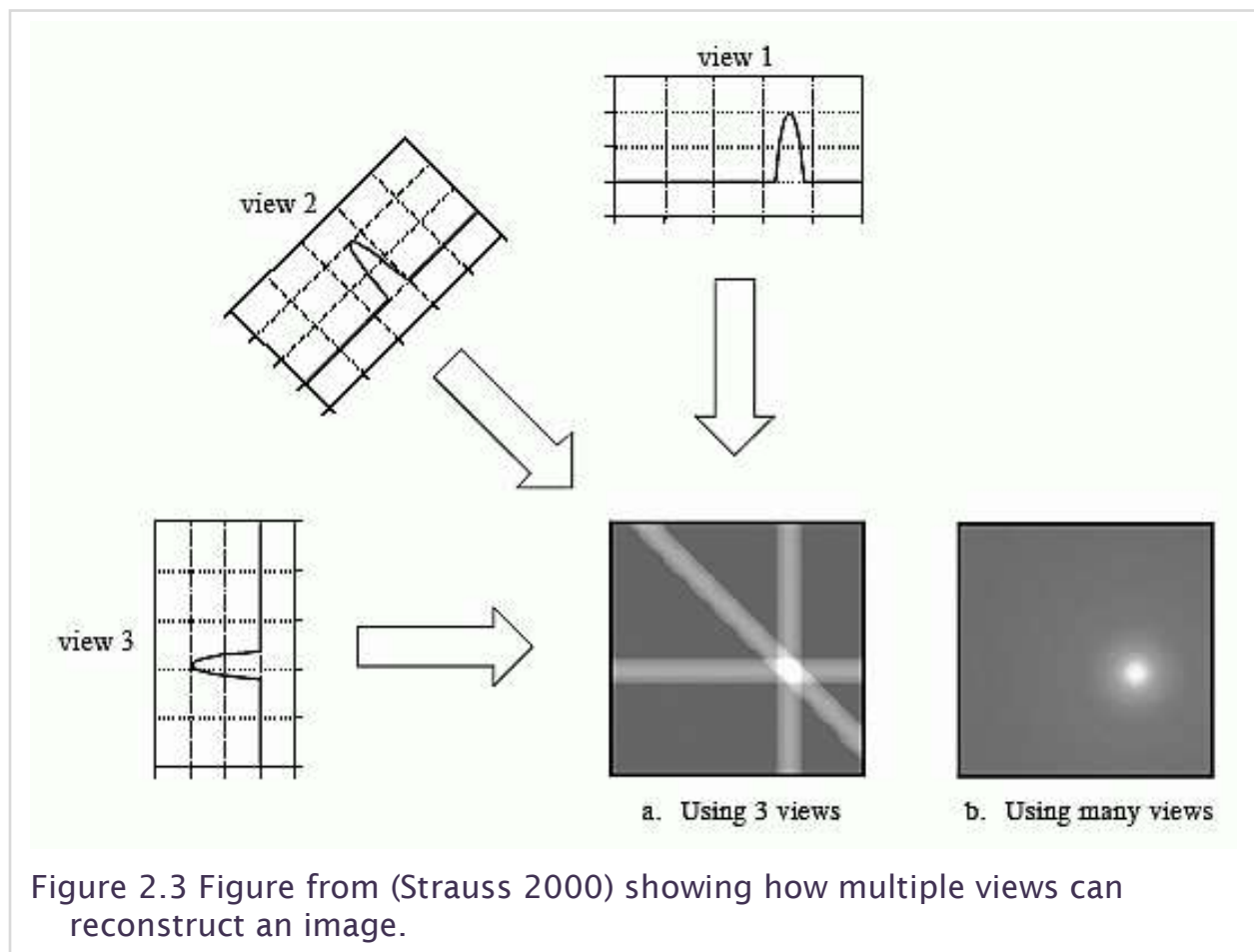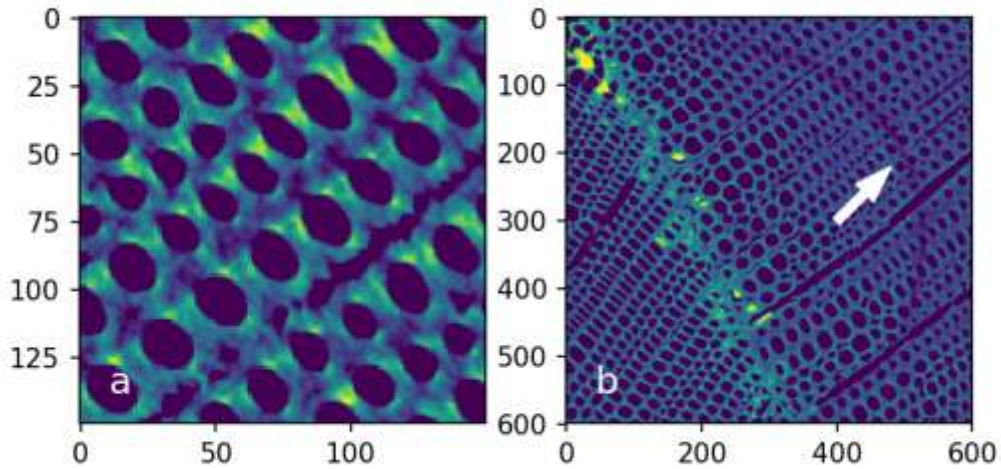
Figure 2.4 Figure showing various artifacts in XCT data of softwood species; illustration of phase contrast (a) and a ring artifact (b).
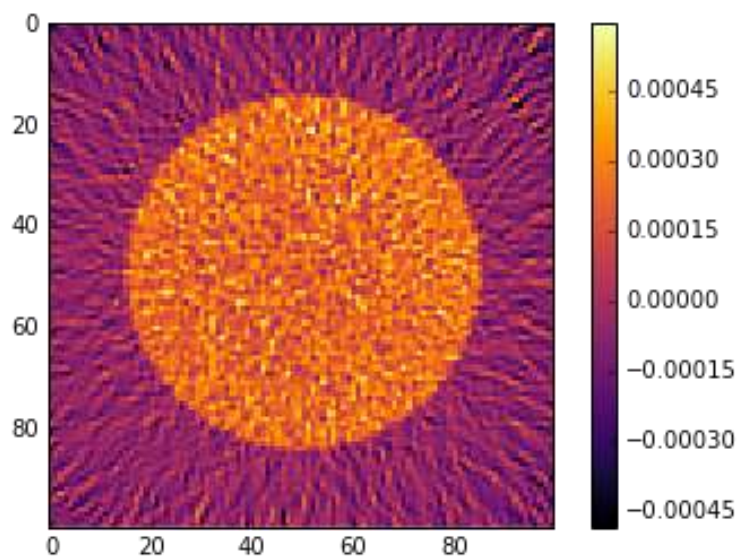
Figure 2.5 A gridrec reconstruction of a single circle with additive noise. The quality of this image is quantified by the metrics in Figure 2.6 and Figure 2.8.
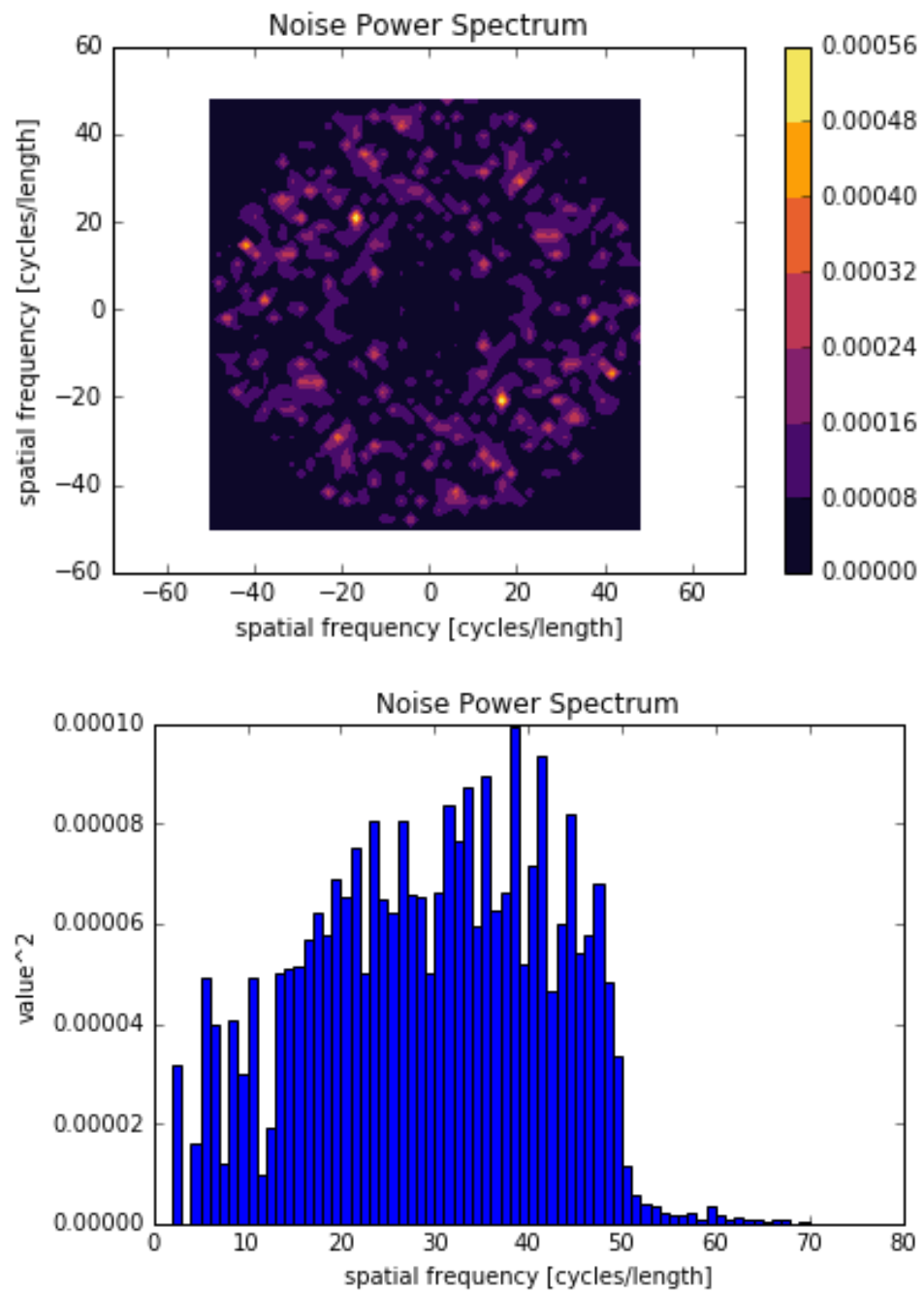
Figure 2.6 The 2D noise power spectrum (top) and 1D radially binned noise power spectrum (bottom) of the unit circle in Figure 2.5.

Figure 2.7 The reference image, camera man, is distorted in various ways using crop, salt and pepper noise, Gaussian smoothing, and unsharp masking.
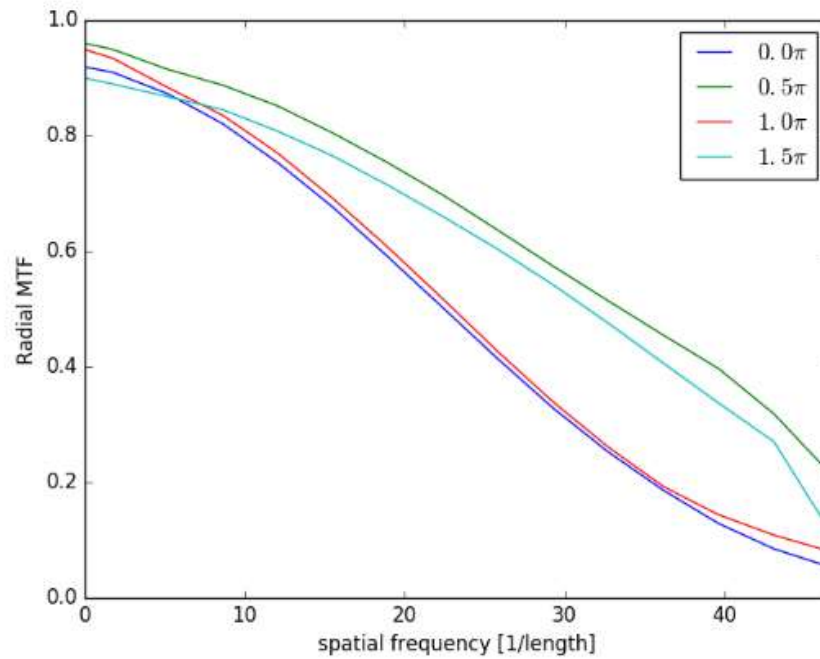
Figure 2.8 The modulation transfer function of the unit circle in Figure 2.5.
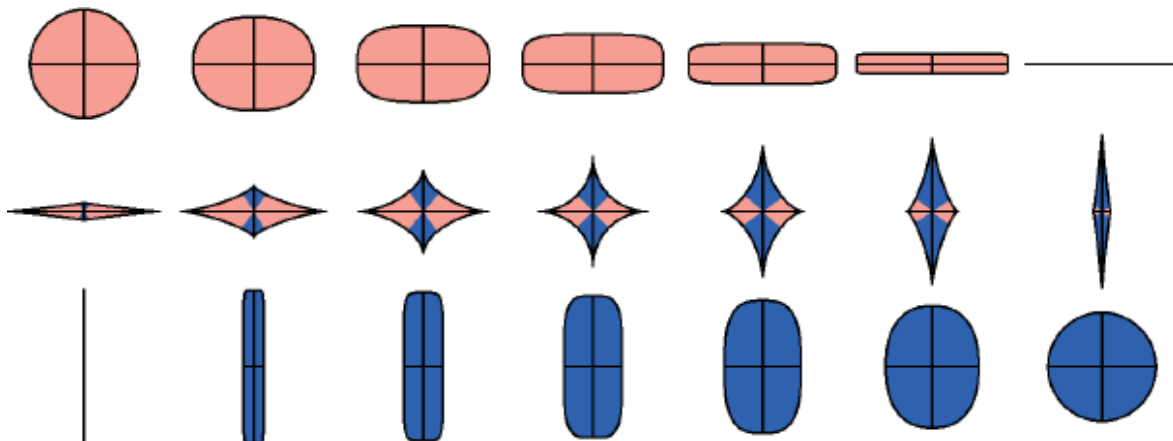
Figure 2.9 Some examples of 2D glyphs for representing second order tensors from (Schultz and Kindlmann 2010).

3 METHODOLOGY FOR COMPARING WOOD ADHESIVE BONDLINE LOAD TRANSFER USING DIGITAL VOLUME CORRELATION

D. J. Ching · F. A. Kamke · B. K. Bay

The steps followed to study the micromechanics of wood adhesive bond planes using x-ray computed tomography (XCT) and digital volume correlation (DVC) are described. A special adhesive was formulated to provide x-ray contrast between the wood cell material and the adhesive. Specimens were mechanically loaded and scanned in a step-loading procedure. DVC was applied to natural texture, and the accuracy and precision of DVC for wood texture was characterized. XCT imagery was segmented and the morphology of the adhesive was compared with the load transfer characteristics. Challenges to be addressed for performing in situ experiments with natural texture and digital volume correlation are discussed. The results show measurable effects of the microstructure on strain distributions, but determining whether there is a significant link between adhesive morphology and bond performance requires further study.

3.1 Introduction

There is a lack of fundamental knowledge about the role which adhesive flow and infiltration plays in the micro-mechanical performance of wood adhesive bonds. Here, adhesive flow means the micron-scale flow of adhesive into opening in the cell wall, and adhesive infiltration means diffusion into the cell wall substance. With the spatial and temporal resolution of X-ray computed tomography (XCT) now reaching from the micron to the nanoscale and from tens of minutes to minutes, there is new opportunity to study this phenomenon. In this publication, for the first time, the combination of XCT,

image segmentation, and image correlation was used to study directly the relationship between adhesive flow and the micro-mechanics of wood adhesive bonds.

3.1.1 Digital Volume Correlation

First published by Bay et al. (1999) as a method to study the mechanics of bone, digital volume correlation (DVC) is the three-dimensional extension of the two-dimensional digital image correlation (DIC) method. In DVC and DIC, points in a reference image are matched with points in a deformed image by comparing information in the correlation window, a defined region surrounding each point. Correlating points between images of the same object at different states of deformation shows how the object deformed. This displacement field can then be used to calculate strain fields and other quantitative measures of deformation (Smith, Bay, and Rashid 2002).

In a digital image, correlation between images requires texture, where texture is represented by patterns of pixel (or voxel) intensity within the correlation window. DIC and DVC require that each point is identified within a unique neighborhood (Bay 2008). The precision of computed displacement and strain values is mostly determined by the size of features in the texture and the size of the correlation window. According to Estrada and Franck (2015), "denser, more gray-valued [texture] generally correlate better, providing higher spatial displacement resolution and sensitivity compared to repeat[ing] patterns or large areas of constant intensity". In the case of DIC, surfaces may be artificially patterned to meet these requirements, but for DVC, existing natural texture must be used for correlation. In the latter case, larger correlation windows will provide lower uncertainty at the cost of lower spatial resolution and smaller correlation windows may resolve higher frequency displacements at the cost of higher uncertainty according to a well-known power law relationship

between correlation window size and measurement uncertainty (Bornert et al. 2009; Reu et al. 2009; Leclerc et al. 2011).

There are two popular techniques for quantifying the uncertainty associated with image correlation experiments. First, simulated deformations on actual or artificial textures are used for quantifying bias and uncertainty from the correlation algorithm itself. Palanca et al. (2015) used this method to compare various DVC algorithms on XCT of bone and showed that coupling DVC with finite element methods reduces uncertainty by an order of magnitude compared to direct matching and FFT methods. Pan (2013) used this method to show that low pass filtering can reduce interpolation bias. Second, a noise floor from multiple images of a static object or one that has been displaced by a known vector (Reu et al. 2009; Gillard et al. 2014) is used to quantify uncertainty from other sources such as detector and specimen motion, detector noise, image artifacts, etc. (Bornert et al. 2009; Reu et al. 2009; Reu 2013). (Tozzi et al. 2017) used this method to show that local structural changes influence the measurement uncertainty for bone.

3.1.2 Previous micromechanical studies of fiber composites

There have been a few studies of anisotropic composite materials using DVC and XCT, but none of them have studied loading in tension along the fiber direction (Brault et al. 2013; Tran et al. 2013) or proposed a metric for measuring shear load transfer across adhesive bond planes.

Two studies using DVC/DIC to study wood are Forsberg et al. (2010) and Derome et al. (2011). Forsberg et al. (2010) was the first to demonstrate DVC on natural wood texture with a three-point bending experiment. They noted that natural texture could cause anomalies in correlation results. Derome et al. (2011) performed correlations in the transverse plane (perpendicular to the grain) for hysteretic moisture swelling experiments.

Zauner et al. (2012) developed a mechanical testing device (also used in this study) for step-loading of wood in compression without blocking the detector in a beamline. However, the collected images were only used qualitatively. In a related study, Zauner and Niemz (2014)investigated potential size effects on the strength of wood by compressing *Picea abies* specimens of four different sizes while making surface measurements using DIC.

Kamke et al. (2014) outlined a methodology for integrating computational modeling and experimental data for investigating the effect of adhesive penetration and morphology on bond strength. As part of this proposed methodology, Schwarzkopf and Muszyński (2015) collected surface DIC data of lap shear specimens for validation of computational models based on static XCT images of the same bond planes.

Baensch (2015) has also conducted step loaded tensile tests of two-layer composites of *Picea abies*. However, quantitative measurement was conducted using acoustic emission and focus was crack propagation not the influence of adhesive morphology.

3.1.3 Bond Quality Metrics

There have been two previous works involving the measurement of shear strains in wood lap shear specimens of which the author is aware. The first (Gindl-Altmutter, Müller, and Konnerth 2012) investigated specimen size effects and adhesive stiffness on the measured shear strength of specimens and the stress concentration factor (SCF), the ratio between the peak stress and minimum stress inside the overlap (Equation 3-1).

$$SCF = \frac{\max \epsilon_{xy}}{\min \epsilon_{xy}}$$ 3-1

Gindl-Altmutter et al. assumed linear elastic behavior and used their strain measurements to directly compute the SCF. Their strain measurements were collected from the surface of their specimens using electronic speckle pattern

interferometry (ESPI) which is like image correlation, but the pattern is generated by using lasers to track the movement of surface roughness. The reasoning behind this metric may be that bonds with a lower SCF are better because concentrated stresses are likely to cause failure.

Another work measuring the strain distribution at the notch of a single lap shear specimens using image correlation was conducted by Schwarzkopf and Muszyński (2015); this study proposed using the shear strain histogram around the notch as a metric for bond quality (Equation 3-2).

$$\sum(1 \; if \; \epsilon_{xy} > \epsilon_{critical})$$ 3-2

Specimens whose distributions have less material with strains above some threshold are deemed more efficient. This reasoning is like that of Gindl-Altmutter et al., by way of higher strains being bad, but in this case, the threshold is absolute instead of relative.

3.2 Materials and Methods

Small single-lap shear specimens were prepared using adhesives specially designed to improve x-ray attenuation contrast. A custom mechanical testing device was used to step load the lap shear specimens in situ at the 2-BM beamline at the Advanced Photon Source (APS) at Argonne National Laboratory, Illinois, USA. X-ray tomography was reconstructed and segmented. DVC measurement uncertainty was estimated. Quantitative measurements of the deformation were calculated. Strain measurements were compared with a FEA model for a simplified homogeneous bonded system.

3.2.1 Specimen Preparation

Specimens in this study were comprised of different adhesives (phenol-formaldehyde and poly-[methylene diisocyanate]), wood types (earlywood and latewood from softwood species, diffuse porous hardwood species), and different species (loblolly pine *Pinus taeda*, Douglas-fir *Pseudotsuga menziesii*,

and hybrid poplar *Populus deltoides x Populus trichocarpa*). Table 3.1 summarizes the quantities of each type of specimen scanned at the APS.

3.2.1.1 Adhesive Synthesis

Two adhesives were prepared according to methods developed by (Paris, Kamke, and Xiao 2015). These special adhesives were covalently bonded to iodophenol or triiodophenol in order to provide sufficient attenuation contrast between wood cell material and the adhesives. Without iodine, the polymers which make up the wood cell material have a similar X-ray attenuation to the polymer adhesives and cannot be segmented.

Iodinated phenol-formaldehyde IPF was obtained from Arclin in Springfield, Oregon. The adhesive was formulated entirely from iodophenol and had a theoretical and measured iodine weight fraction of approximately 40 % (Paris et al. 2014). The adhesive was stored at $-10°C$ while not in use to minimize further polymerization before bonding.

Iodinated poly methylene diphenyl diisocyanate IpMDI was synthesized according to (Paris, Kamke, and Xiao 2015) with triiodophenol. Commercially produced pMDI was reacted with triiodophenol to yield 24 % by weight iodine content. To maintain low viscosity, the IpMDI was mixed with anhydrous tetrahydrofuran (THF) before application to the wood. The adhesive was used within one week of synthesis and stored at $5°C$.

3.2.1.2 Substrate Preparation

Production of the specimens required precise control over a bonded interface 2 mm by 5 mm in size, so planning began with the careful selection of wood planks for bonding. Wood blocks of the desired species were cut into planks to obtain a tangential surface, with grain parallel to the bonding surfaces. The size of the planks was approximately 10 cm by 15 cm. The planks were planed down to 4 mm thickness such that they were thin but still

workable. Planks were matched into pairs such that final specimens had the desired interfaces: earlywood-earlywood, earlywood-latewood, or latewood-latewood. There was no distinction between earlywood and latewood with the hybrid poplar specimens. Planks with knots, cracks, or other irregularities were discarded.

3.2.1.3 Hot Pressing

The hot press was preheated to 185°C for phenol-formaldehyde adhesives and 50°C for pMDI adhesives. Lower temperature was used for pMDI because of the presence of THF in the iodinated adhesive mix. Planks were freshly planed before applying adhesive. The mass and surface area of one half of each plank pair was measured. The adhesive was dropped from a pipette onto one of the bonding surfaces until the adhesive solids loading was 120 gm^{-2}. A steel roller was used to spread the adhesive.

The plank was reweighed and more adhesive was added until the final desired weight was reached. This adhesive spreading was done quickly because volatiles in the adhesives evaporate at room temperature. Plank pairs were pushed together and wrapped with aluminum foil to catch the adhesive that squeezes out of the composite during hot pressing. The composite was pressed at 690 kPa for Douglas-fir and pine and 420 kPa for poplar. The press time was 8 min for phenol-formaldehyde adhesives and 14 h for pMDI adhesives.

3.2.1.4 Composite Shaping

After the large sandwich composites were pressed, they were sanded on both sides until they were approximately 2 mm thick. A small table saw was used to cut the composites into slivers of 30 mm length and 2 mm width. Then a small band saw was used to cut two notches on opposite sides of the bond plane 5 mm apart. Next, a sledge microtome was used to cut the specimens to a 2 mm by 2 mm cross section. Finally, the specimens were glued into threaded

metal holders using two-part epoxy (Devcon Home 5-min Epoxy, part number: 21045, Hartford, Connecticut) and a jig to hold the specimens in alignment with the metal holders while the epoxy set over 12 h. A schematic of specimen geometry may be seen in Figure 3.1a.

3.2.1.5 Preliminary Mechanical Testing

A small selection of specimens was used to predict the load and displacement performance of each specimen type prior to XCT scanning. The preliminary specimens were used to calculate the average engineering stress and strain for 30% of ultimate, 60% of ultimate, and ultimate load. These metrics were then used to determine the loading procedure during the XCT scans.

3.2.2 Scanning for X-ray Computed Tomography

The specimens were imaged at beam line 2-BM at the Advanced Photon Source, Argonne National Laboratory. A mechanical testing device developed by Zauner et al. (2012) was installed inside the experiment hutch and used to apply a tensile load to the specimens while they were scanned. Each specimen was ideally scanned five times: one reference scan, two scans in the elastic deformation regime, one scan in the plastic deformation regime, and one scan post-failure.

3.2.2.1 Mechanical Testing

The mechanical testing device (Zauner et al. 2012) is a gear driven displacement controlled tensile machine with two threaded sockets. A transparent (to x-rays) tube is used to support the top socket while the bottom socket moves vertically in the base. The purpose of this geometry is to allow the testing device to rotate in the X-ray beam, with the specimen, without blocking the detector. Our specimens (

Figure 3.1a) were designed to screw into the device such that they can be pulled in uniaxial tension.

To collect the five scans, the specimen was first screwed into the mechanical testing device, preloaded with a few Newtons of force, and one reference scan was obtained. Next, with a crosshead movement of 5 µms^{-1}, specimens were loaded to 30 % of their predicted ultimate load. Because the mechanical testing device exhibited stress relaxation, it was allowed to relax for a few minutes before beginning the scan. Next, with a crosshead movement of 5 µms^{-1}, the specimen was loaded to 60 % of predicted tensile load. Again, the mechanical testing device was allowed to relax for a few minutes before beginning the scan. Next, with a crosshead movement of 0.2 µms^{-1}, the operator watched the load displacement curve for the elastic plastic transition and attempted to stop the mechanical testing device for the fourth scan. Again, the mechanical testing device was allowed to relax for a few minutes before beginning the scan. Finally, with a crosshead movement of 0.2 µms^{-1}, the specimen was loaded until failure and scanned a final time. An example displacement and force vs time plot of this loading scheme may be seen in Figure 3.2.

3.2.2.2 Scanning Parameters

The XCT scan consisted of 1500 projections taken over a 180° rotation. The scanning parameters were not the same as used by Paris et al. (2015) when the adhesive system was developed. The change of scanning parameters was implemented to improve image contrast between adhesive and cell wall and reduce scan time. Beam energy was increased and exposure time was reduced for the purpose of reducing overall scan time, thus reducing the potential for specimen motion during a scan. The specimen to scintillator distance was increased to accommodate the physical dimensions of the mechanical test

device and to enhance the effect of x-ray diffraction. A comparison of the scanning parameters is shown in Table 3.2.

3.2.3 Image Reconstruction and Processing

The 3D volumes were reconstructed from the 2D tomographic data collected at the APS. They were also segmented in order to perform morphological analysis of the adhesive bond planes.

3.2.3.1 Reconstruction with TomoPy

The tomographic data was reconstructed using version 0.0.3 of TomoPy (Gürsoy et al. 2014). TomoPy is an open source Python module for tomographic reconstruction and artifact mitigation available through GitHub. The sinograms were first normalized to reduce artifacts due to detector irregularities and beam inconsistencies. Next, they were modified with the phase contrast method to boost contrast between the adhesive and cell wall. The regularization parameter used for phase contrast was 2×10^{-4}. Some specimens had ring artifacts reduced using the ring removal tool. Finally, the gridrec reconstruction algorithm was used for reconstruction.

3.2.3.2 Segmentation

The adhesive was segmented from the wood cell material using distribution fitting. The expectation maximization algorithm was used to fit a mixture of normal distributions to the color intensity histogram of the tomography. By assuming each peak belongs to one component of the specimen (cell wall, adhesive, air, etc.), each pixel in the image may be assigned to its most probable component based on color alone.

3.2.3.3 Morphological Quantification

Two metrics, effective penetration (EP) and weighted penetration (WP), were used to describe the morphology of the adhesive in the bond planes. These metrics developed by (Sernek, Resnik, and Kamke 1999; Paris et al. 2014)

are summarized in Equations 3-3 and 3-4, where V_i is the volume of a given adhesive voxel, $A_{bondplane}$ is the area of the bond plane, and d_i is the distance from the bond plane to the center of a given adhesive voxel.

$$EP = \frac{\sum V_i}{A_{bondplane}}$$

<div align="right">3-3</div>

$$WP = \sqrt{\frac{\sum d_i^2 V_i}{\sum V_i}}$$

<div align="right">3-4</div>

All the segmentation and morphological quantification of the specimens was performed using scripts written with MATLAB. These scripts are available on GitHub at carterbox/wpart.

3.2.4 Digital Volume Correlation

The reconstructed data was analyzed using Vic-Volume, a digital volume correlation software (Correlated Solutions, Inc., Colombia, SC). Two other DVC softwares were tried. All three have their drawbacks, but Vic-Volume was chosen because of its ease of use, speed, lower memory requirements, and most complete user interface.

3.2.4.1 Uncertainty Quantification

To quantify the uncertainty of DVC measurements in natural wood texture, a single specimen was scanned twice without applying any deformation. Next, these two volumes were correlated using the parameters shown in Table 3.3. Correlation window size was found to be the dominating parameter. Figure 3.2 shows the uncertainty (one standard deviation) of the computed strains as a function of window size for all six strain components. The uncertainty for both is well behaved and decreases exponentially with increasing correlation window size. From these measurements, a correlation window size of 150µm was chosen. Slightly larger correlation volumes are

supported by Vic-Volume, but processing time is a cubic function of correlation window size.

3.2.5 Load Transfer Analysis

The strain fields were downsampled to a 50µm grid and reoriented such that the basis vectors aligned with the plane of the bond plane, where the radial direction, R, is perpendicular to the bond plane; the longitudinal direction, L, is the loading direction; and the tangential direction, T, is orthogonal to the other two directions. The smoothest strain field from the linear elastic region of each specimen was selected for comparison between specimens. As a consistency check, the shape of the strain fields were compared with a simple finite element model (Figure 3.3 Comparison of (a) finite element and (b) digital volume correlation strain fields.) of a homogeneous, single-lap shear specimen created using NairnFEA (John A. Nairn 2014).

The two metrics, SCF and the strain threshold method of Schwarzkopf and Muszyński were implemented. For SCF, the results are shown in Figure 3.4. For the Schwarzkopf and Muszyński method, a region of interest up to 0.5 mm on both sides of the bondline, up to 1.5 mm from the notch, and averaged along the longitudinal direction was extracted. Then the strains were divided by the nominal tensile stress experianced by the specimen. These normalized shear strains ranged from 0 to 0.1 GPa^{-1}. A threshold of 0.05 GPa^{-1} was selected for the results shown in Figure 3.5.

$$\epsilon_{xy} = ax^k + c \qquad \qquad \text{3-5}$$

A third metric, newly proposed here to measure the load transfer efficiency of each specimen was used also. The bond quality was parameterized by fitting a power function (Equation 3-5) to the mean shear strain within a 0.5 mm region on either side of the bond line from the notch to the center of the specimen (Figure 3.6). A power law equation was chosen because it fit the shape of the curves well. Strains in the tangential direction were averaged. The

finite element model predicts that bonds which effectively transfer load from one adherend to another have a rapid drop in shear strain moving away from the notch. The exponent coefficient, k, in the power function describes this drop, and the leading coefficient, a, and trailing coefficient, c, scale the data to account for different loads applied to each specimen. The comparison of EP and WP with this metric is shown in Figure 3.7.

3.3 Results

Figure 3.1, Figure 3.8, Figure 3.9 show a sampling of specimens analyzed with DVC. Part a shows the location of the analyzed region in the larger specimen. Part b shows two slices of the tomography in the RT and LR planes. Part c shows the maximum adhesive concentrations projected onto the RT and LR planes. Part d shows the average shear strain projected onto the RT and LR planes normalized to the largest magnitude strain. Strain fields mostly follow what is predicted by the FEA model for a single-lap shear specimen; there is a higher compliance at the notch and along the bond plane. Deviations may be explained by misalignment of specimens in the testing device resulting in a bending moment and the natural variation of the wood cellular structure.

The relationships between shear strain drop coefficient, k, SCF, and fraction below threshold were compared with EP and WP for each of the specimens (Figure 3.7, Figure 3.4, Figure 3.5). None of metrics showed correlation with EP or WP. The data was also visually inspected for instances when the structure of the wood or adhesive overtly influenced the strain distribution during loading. Examples of this are seen in

Figure 3.1, where an adhesive filled resin canal creates a depression in the strain field; Figure 3.8, where the high strain region is skewed left following the left skewed adhesive penetration; and Figure 3.9, where the high strain region moves left to follow a more compliant earlywood region adjacent to the latewood-latewood interface.

3.4 Discussion

3.4.1 Specimen Fabrication and Mechanical Testing

Upon reviewing the reconstructed data sets it is clear that specimens should have been more thoroughly controlled. In some specimens, the edges were not cut parallel to the bond plane (Figure 3.10a). In some specimens, not all the notches were cut all the way through the bond plane (Figure 3.10b); if the adhesive region is not completely severed at the notch, then the behavior in the lap is more tensile than shear. Some specimen surfaces were contaminated with the two-part epoxy (Figure 3.10c), which was used to adhere the specimens to the mechanical testing device; the displacement fields of these specimens suggested that there was unexpected load transfer occurring because along the epoxy. Tape could have been used to protect the region of interest from contamination during assembly. Some specimens did not have the desired wood type along the entire bond plane (Figure 3.10d); this is impossible to see before scanning, but surplus specimens could have been mounted and rejected or accepted after the first scan.

At the beamline, specimens should have been more carefully aligned with the field of view. On some specimens, the field of view did not contain as much of the region of interest as possible; sometimes this is due to specimen movement from its initial position, other times it was poor placement by the operator. If for each scan, the field of view were realigned with the notch, larger strain fields could have been calculated for all specimens. To help operators keep the area of interest inside the field of view for each scan, painting the outside of the specimen with references marks (e.g. dots of metallic paint) could be helpful.

Alternatively, the field of view could be increased. The correlation window size of 150 microns leaves room for the pixel size to increase between two and three times without losing salient details in the wood texture that are important

to correlation. Some detail in the adhesive flow may be lost, but those details do not need to be tracked dynamically and could be captured at higher resolution in a pre-deformation scan. Additionally, collecting a larger field of view scan of each specimen could be helpful for generating boundary conditions in computational models of the specimen. Models starting with XCT of the entire specimen can implement accurate geometry of the specimen and account for differences in the behavior between earlywood and latewood. The only things that would be lost by increasing the pixel size are some of the details such as pits and small flows of adhesive through them. However, the ability of XCT to capture diffusion of the adhesive into the cell wall is not good anyways because of contrast issues.

3.4.2 Attenuation Contrast

The x-ray scanning parameters for this study were changed (Table 3.2) from those used by (Paris, Kamke, and Xiao 2015). Exposure time was decreased by increasing beam energy. This was favorable due to the time sensitive nature of the experiments; however, the phase contrast effect from additional specimen to detector distance did not make up for the loss in attenuation contrast which results from the wood cell and adhesive becoming more transparent to x-rays at higher beam energies.

Figure 3.11 compares contrast between IpMDI and cell walls for the work done by (Paris, Kamke, and Xiao 2015) and the work of this study. The result was that segmentation of the adhesive from wood cell walls was made more difficult for IPF adhesives, and all IpMDI bonded specimens had poor contrast. Consequently, the IpMDI specimens were dropped from the study. An investigation was conducted to determine whether the IpMDI adhesives were formulated correctly and if the iodine remained covalently bonded to the cured adhesive. Energy dispersive X-ray spectroscopy (EDS) showed iodine present in appropriate regions of the IpMDI-bonded specimens (McKinley et al. 2016).

3.4.3 Uncertainty with Natural Texture

Most image correlation research focuses on two-dimensional applications where textures may be customized and images are easily captured and processed in large quantity. In the case of DVC, however, researchers are now trying to use image correlation on natural textures from data collected from a limited number of synchrotron facilities where time is limited or expense is prohibitive. Thus, procedures are not well established, and sources of uncertainty are not well controlled.

In the literature, DVC algorithms are tested on artificial textures or specially made standards whose properties mimic the applied ideal textures of DIC. For idealized materials, where texture is uniform and isotropic, these tests may also be applicable. However, they may not accurately represent the expected uncertainty for natural textures which are anisotropic, inconsistent, and/or corrupted with noise unique to computed tomography. (Forsberg et al. 2010) and (Tozzi et al. 2017) noted these inconsistent measurements from natural texture, but made no mention of how to mitigate them. Because natural textures are not ideal and current options are limited for optimizing data acquisition and correlation parameters, quantifying expected measurement uncertainty by using a noise floor is imperative.

The present study observed two mechanisms through which measurement uncertainty was affected. First, measurement uncertainty was shown to be orthotropic in the same way as the underlying texture. This is shown in Figure 3.2, where the measurement uncertainty in the longitudinal direction of wood is higher than the radial and tangential directions for all correlation window sizes. One might expect that if the measurement uncertainty of a texture is anisotropic for isotropic correlation windows, an anisotropic correlation window may provide an isotropic measurement uncertainty. The advantages could be a smaller correlation volume because only

some dimensions of the window are increased to lower measurement uncertainty. However, this is not presently an option in any commercially available DVC software.

Second, orientation and scale changes in the natural texture of wood influenced the measurement uncertainty. This lead to local differences in the uncertainty from region to region in the specimen. Ideally, measurement uncertainty would be uniform across an area of interest, but natural textures change orientation and scale. For each region in Figure 3.12a the anisotropy and magnitude of the three-dimensional measurement uncertainty is shown as a glyph (Figure 3.12b). Each spoke of these glyphs represents the measurement uncertainty (σ_{TT}, σ_{TR}, σ_{RR}, σ_{RL}, σ_{LL}, and σ_{LT}) of the six unique strain tensor values. Although the measurement uncertainty in the longitudinal direction, σ_{LL}, is dominant for most of the texture, a region in the middle of the specimen has almost isotropic uncertainty. Since every specimen is unique, ideally, local uncertainties should be calculated for each specimen and correlation window dimensions should be chosen locally; however, in this study, one wood specimen, scanned after the primary data set was collected was used as a proxy to estimate correlation uncertainty and proper correlation settings for all specimens. Perhaps a method for locally adapting correlation window sizes to natural texture would provide uniform measurement uncertainty across the entire specimen.

3.4.4 Computed Shear Strains

Although structural elements of the adhesive do affect the strain distribution within the specimens, there were no observed correlations between EP, WP, and the three metrics of bond quality applied here. These methods may be inconclusive due to the variability of wood and small quantity of data. A larger number of specimens, with improved control over the geometry of the specimens, should be tested to determine whether there are actual relations

between micron-scale adhesive penetration and the load transfer characteristics of wood adhesive bonds, but also, it may be that bond quality cannot be reduced to a single parameter. Reducing the complexity of the experiment to one wood type would also improve the chances of observing a relationship between penetration and load transfer.

3.5 Conclusion

Lap shear wood composite specimens were fabricated for three different wood species and two specially formulated adhesives. The specimens were step loaded and scanned using XCT at the Advanced Photon Source using a custom mechanical testing device. A change in the scanning parameters from previous works caused a decrease in image contrast, which made the resulting data sets difficult to segment. Datasets were reconstructed and correlated using digital volume correlation. Two challenges for image correlation methods were identified. First, the measurement uncertainty was found to be orthotropic for natural texture. Second, the measurement uncertainty was found to be inconsistent across the specimen. The effect of adhesive penetration on load transfer across the bonding interface is inconclusive. It is unclear if the results were inconclusive due to lack of a relationship between adhesive penetration and stress transfer, or if the natural variability of wood texture, less than optimum specimen preparation, and small number of specimens obscured a relationship.

3.6 Tables

Table 3.1 Summary of scanned specimens by type

Species	Adhesive	Interface	Quantity
hybrid poplar	IPF	diffuse porous	3
pine	IPF	earlywood-latewood	4
Douglas-fir	IPF	earlywood-earlywood	2
Douglas-fir	IPF	earlywood-latewood	5
Douglas-fir	IPF	latewood-latewood	4
Douglas-fir	IpMDI	earlywood-latewood	2

Table 3.2 Comparison of scanning parameters used at beamline 2-BM in October 2014 and in previous studies by Paris et al. (2014)

Scanning Parameter	This Study	Paris et al.
beam energy	25keV	15.3keV
exposure time	150ms	250ms
number of images per scan	1504	1504
approximate scan time	7min	20min
specimen to scintillator distance	50mm	8mm
total rotation	180	180°
image resolution	1.3μm/voxel	1.45μm/voxel

Table 3.3 Vic-Volume (Correlated Solutions, Colombia, SC) settings for digital volume correlation

Strain filter size	9
Step size	16
Window size	115
Interpolation	Optimized 4-tap
Window weights	Uniform
Correlation	NSSD
Consistency [pixels]	0.1
Confidence [pixels]	0.02
Matchiness [pixels]	0.01
Strain calculation	LaGrange

3.7 Figures
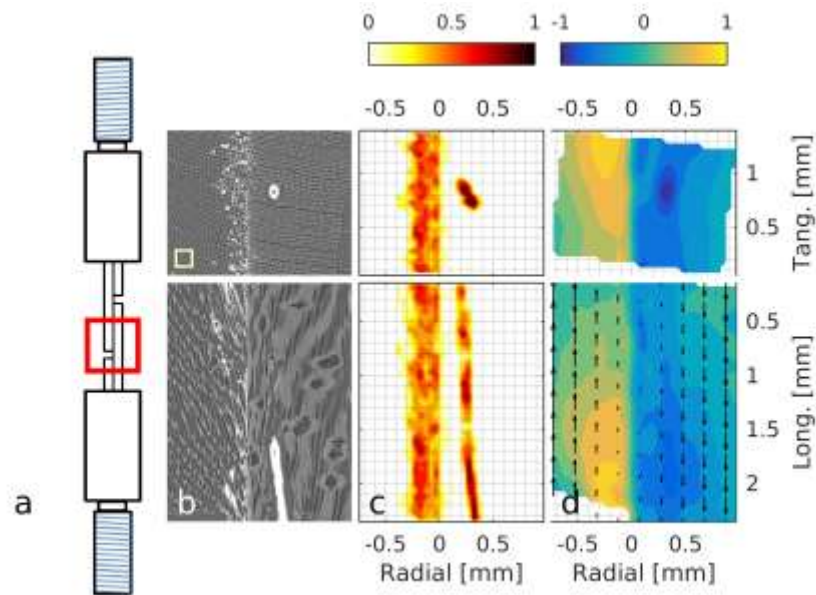
Figure 3.1 Segmentation and shear strain field of an earlywood-latewood southern yellow pine specimen. (a) Schematic of a lap shear specimen [mm] showing ROI (b) Tomographic cross section through the center of the ROI in the radial-longitudinal and tangential-radial planes. Correlation window size shown in lower left. (c) The maximum adhesive volume fraction through the cross section. (d) Shear strain at one time-step normalized to the range [-1, 1] and averaged through the cross section. The shear strain (d) is depressed in a region around a resin canal filled with adhesive (b).
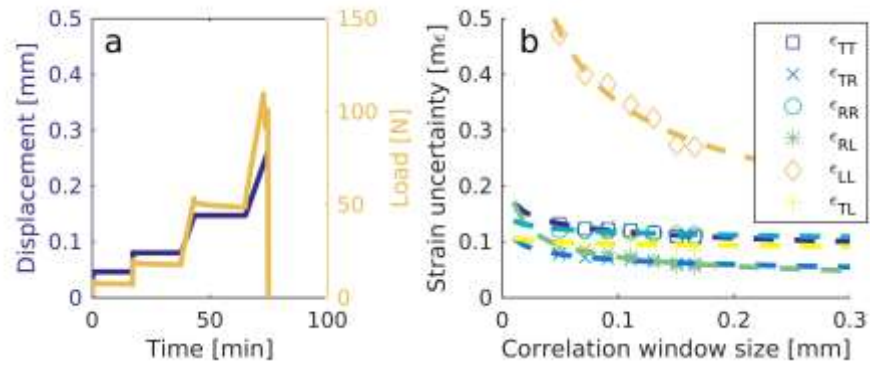
Figure 3.2 (a) Example loading scheme for five scans during step-loading. Specimens were scanned at each of the three plateaus in the displacement curve (left) as well as before loading and after failure. Stress relaxation of the testing device is visible in the force curve (right) at each plateau in the displacement. (b) Measured uncertainty as a function of correlation window size.
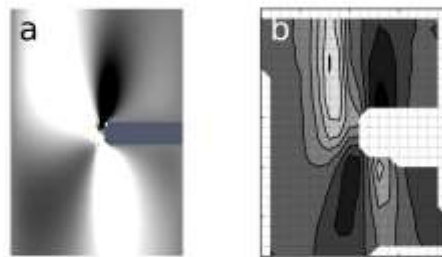
Figure 3.3 Comparison of (a) finite element and (b) digital volume correlation strain fields.
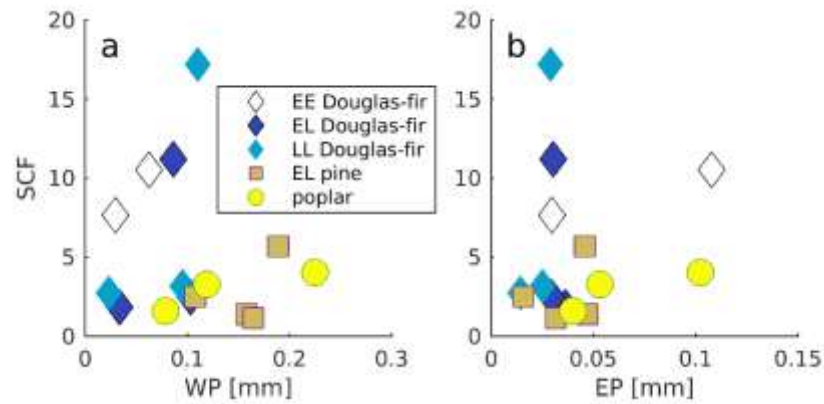
Figure 3.4 Figure Weighted penetration and effective penetration versus strain concentration factor for each specimen.
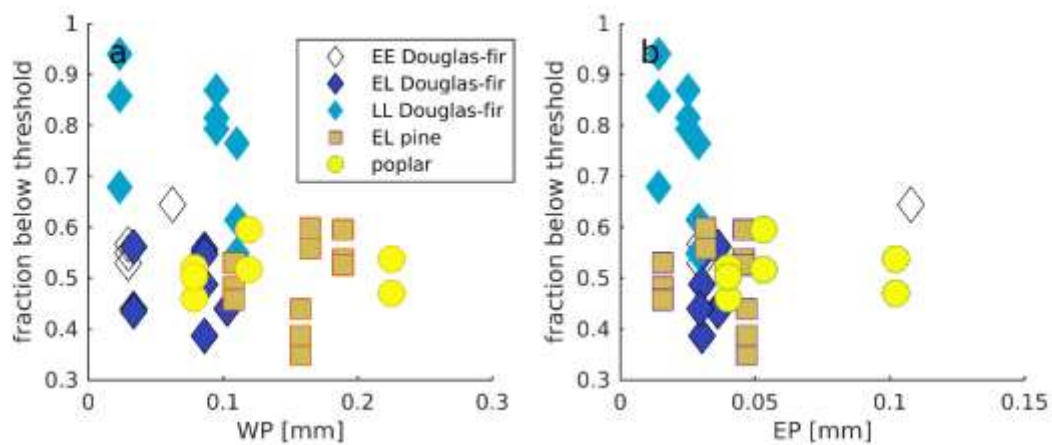
Figure 3.5 Figure strain thresholding metric suggested by Lech versus weighted and effective penetration for the threshold of 0.05 strain GPa[-1]. Every step is shown for each specimen. It doesn't even matter because there is no trend.
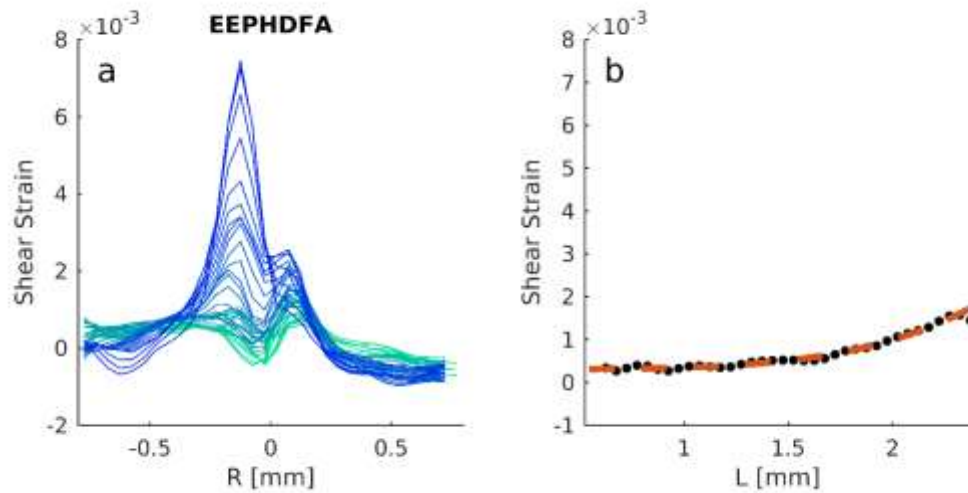
Figure 3.6 (a) Measured shear strain for each longitudinal slice. Darker contours are closer to the notch and lighter contours are farther way. (b) The power law function is fit to the mean shear strain within 0.5mm of the bondline for each longitudinal slice.
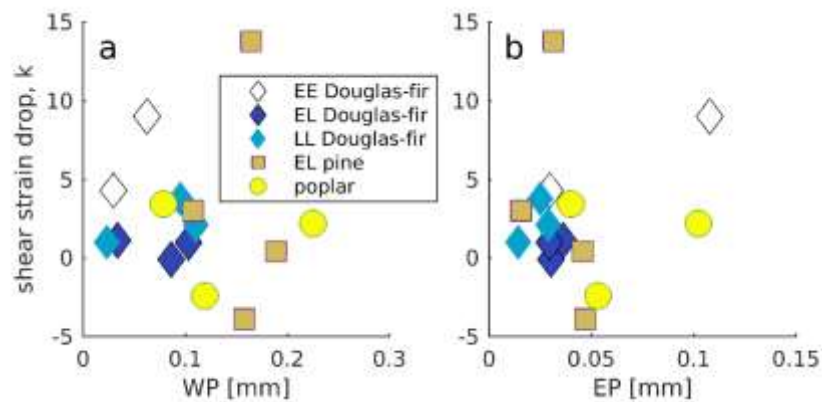
Figure 3.7 Weighted penetration and effective penetration versus shear strain drop, k, for each specimen.
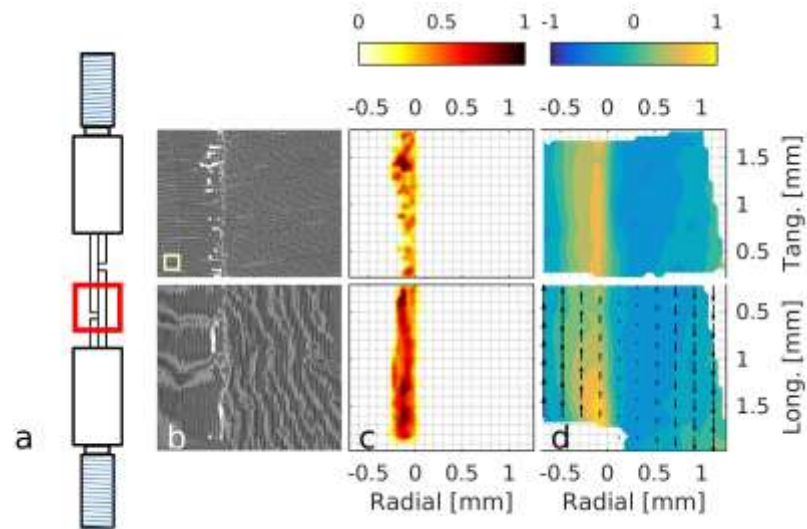
Figure 3.8 Segmentation and shear strain field of an earlywood-latewood Douglas-fir specimen. (a) Schematic of a lap shear specimen [mm] showing the ROI. (b) Tomographic cross section through the center of the region of interest in the radial-longitudinal and tangential-radial planes. Correlation window size shown in lower left. (c) The maximum adhesive volume fraction through the cross section. (d) Shear strain at one time-step normalized to the range [-1, 1] and averaged through the cross section. The shear strain (d) skews to the left to follow the more compliant earlywood region (b).
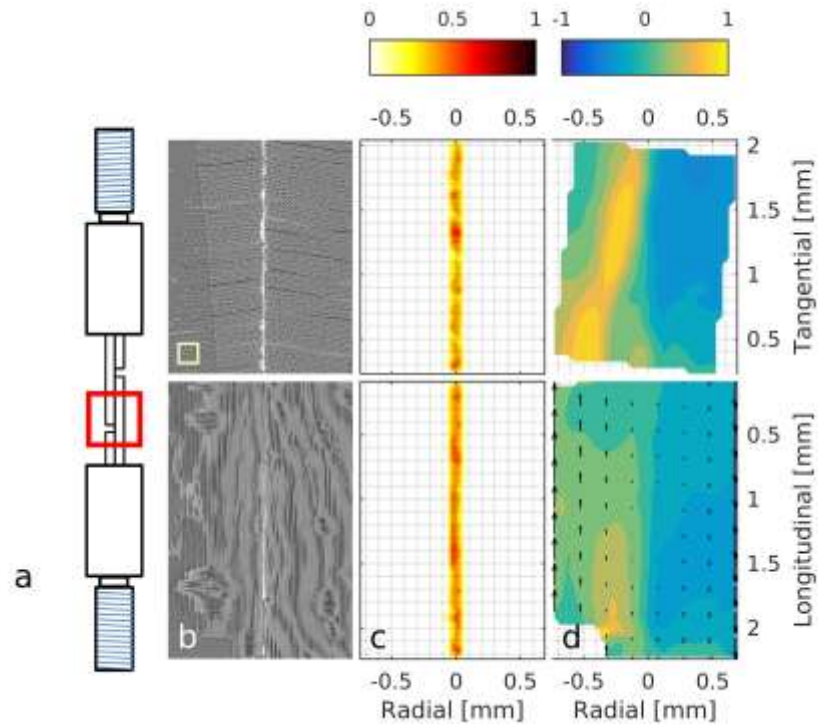
Figure 3.9 Segmentation and shear strain field of a latewood-latewood Douglas-fir specimen. (a) Schematic of a lap shear specimen [mm] showing the ROI. (b) Tomographic cross section through the center of the region of interest in the radial-longitudinal and tangential-radial planes. Correlation window size shown in lower left. (c) The maximum adhesive volume fraction through the cross section. (d) Shear strain at one time-step normalized to the range [-1, 1] and averaged through the cross section. The shear strain (d) skews to the left to follow the more compliant earlywood region (b).
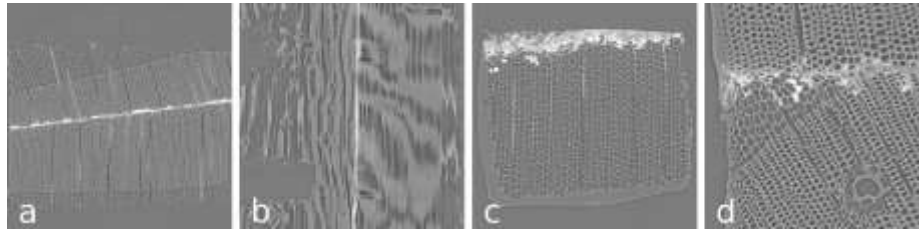
Figure 3.10 Various manufacturing defects in lap shear specimens. (a) Bond plane misaligned with edges of specimen. (b) Notch does not cut through to the bond plane. (c) Two-part epoxy contamination of the region of interest. (d) Desired wood type does not cover the entire bond plane.
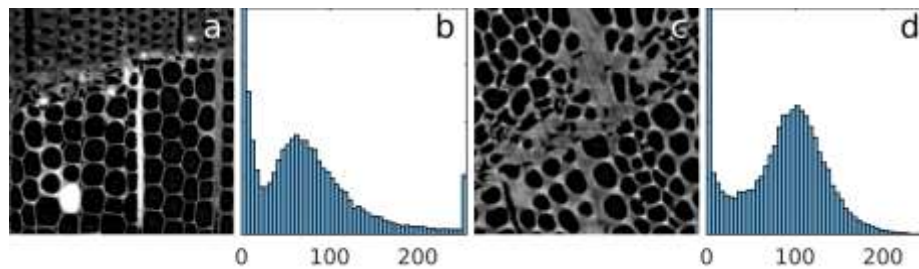
Figure 3.11 Adhesive contrast for Douglas-fir and IpMDI specimens scanned by (Paris, Kamke, and Xiao 2015) (a, b), and by this study (c, d) (McKinley et al. 2016).
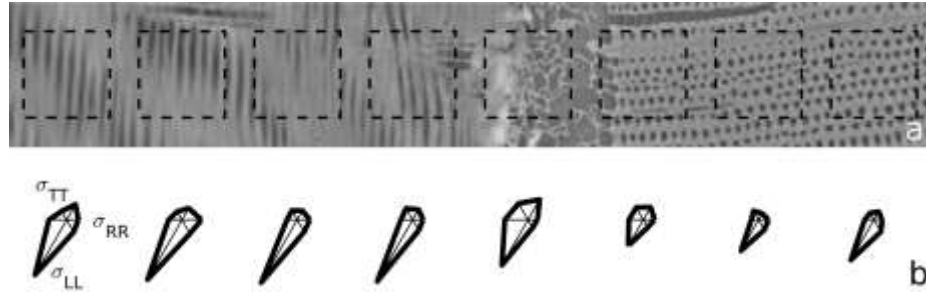
Figure 3.12 Regional changes in strain measurement uncertainty in a cross laminated Douglas-fir specimen; radial surface is at left and transverse surface at right. (a) Wood texture. (b) Glyphs representing the strain uncertainty anisotropy.

4   X-RAY COMPUTED TOMOGRAPHY OBSERVATIONS OF MOISTURE SWELLING IN WOOD ADHESIVE BONDLINES

D. J. Ching · J. Jakes · F. A. Kamke · C. Frihart · C. Hunt · D. Yelle · L. Lorenz · W. Grigsby · X. Xiao

Moisture swelling of wood adhesive bondlines is important because their behavior affects the moisture durability of all wood composite products: furniture, wood flooring, composite structural lumber, etc. It has been observed that water resistant adhesives, such as phenol-formaldehyde (PF), provide some resistance to moisture-induced swelling, and it is proposed that adhesive penetration may influence moisture resistance. However, *in situ* observations of swelling in bondlines are lacking. In this study the volume change in bonded specimens and one clear control specimen were examined using x-ray computed tomography and an *in situ* relative humidity chamber. Several PF adhesives, with varying degree of polymerization, were studied. The study measured local volume changes around the bondlines using digital volume correlation in each of the specimens at the 10-micron scale, characterized the wood cell geometry to explain the observed transverse swelling anisotropy, measured the volume change of the *in situ* segmented adhesive, and attempted to measure the local effects of ray cells on the swelling. The results suggest that the adhesive degree of polymerization is less important than adhesive flow distance for determining the influence of adhesive on moisture swelling. Adhesive suppression of moisture induced swelling was only observed in the radial direction near the bondline (direction perpendicular to the bondline) and in the tangential direction near adhesive filled rays (direction perpendicular to the adhesive filled rays). There is evidence that expansion mismatch between the wood and adhesive caused the adhesive to break inside ray cells; this may be the reason that swelling was only observed perpendicular to the rays.

4.1 Introduction

The growing forest products market depends on adhesives, and these products are exposed to changes in moisture content in route to their destination, during installation, and in service. Cyclic moisture-induced swelling is a cause of bond failure for improperly utilized wood products (Bucur 2011; Frihart and Wescott 2008), so determining how wood-adhesive interphases behave during moisture-induced swelling is important to the development of durable wood products, which will inevitably experience changes in moisture content over their service life (Ormarsson and Gíslason 2016).

This manuscript is one of a series about multiscale characterization techniques for wood adhesive bondlines (Kamke et al. 2014; Jakes et al. 2015; McKinley et al. 2016; M. Schwarzkopf et al. 2016; Kamke et al. 2016; McKinley et al. 2018), with emphasis on characterizing moisture effects. In particular, this manuscript focuses on measuring the influence of the adhesive bondline on softwood latewood bonded with a Br-labeled phenol-formaldehyde (BrPF) adhesive of various molecular weight distributions.

4.1.1 Moisture-induced swelling anisotropy in softwoods

Boutelje (1962) gave an in-depth review of the anisotropy in moisture-induced swelling and elasticity of softwoods. The author concluded that cellular geometry is responsible for the bulk anisotropy of moisture-induced swelling and elasticity of wood. This conclusion was based on large scale 2D models of an earlywood cross-section that was made from plexiglass. The plexiglass model was compressed along the radial and tangential directions to show that

it had elastic anisotropy. While this experiment shows that cellular geometry alone can be responsible for elastic anisotropy, Boutelje incorrectly conflated elasticity and moisture-induced swelling to draw the conclusion that because the elastic anisotropy exists, the same structure will have moisture swelling anisotropy. Any cellular structure made of isotropically expanding material will also expand isotropically. For a cellular structure to expand anisotropically, the cell wall substance must also expand anisotropically.

Supporting this theory, Derome et al. (2011) and Patera et al. (2013) observed moisture-induced swelling in Norway spruce (*Picea abies*) with x-ray computed tomography. Based on this initial work, finite element models of cellular structures were created (Rafsanjani, Derome, and Carmeliet 2012; Rafsanjani et al. 2013). They showed that the anisotropic moisture-induced swelling in wood cells is caused by a combination factors, including anisotropic swelling of the cell wall substance in the parallel- and perpendicular-to-wall surface directions, and cell geometry parameters, such as ratios between radial and tangential wall lengths (ξ), cell wall thickness (t), and angle between radial and tangential walls (θ). Following this modeling, Rafsanjani et al. (2014) directly observed transverse anisotropy of the cell wall substance in sections cut from the S2 layer of Norway spruce using x-ray computed tomography. This is not to say that the S2 layer alone is responsible for parallel- and perpendicular-to-wall anisotropy; the S1 and S3 layers are also thought to contribute to the anisotropy (Schulgasser and Witztum 2015). The cause of swelling anisotropy within the layers of the cell wall substance is not the focus of this paper; rather, we are interested in the behavior on the 10-micron scale.

4.1.2 The influence of ray cells on moisture-induced swelling anisotropy

Boutelje (1962) also investigated whether ray cells had a measurable effect on the local moisture-induced swelling of softwoods. They concluded that uniseriate rays in softwoods most likely do not have a significant effect on the

swelling anisotropy of bulk wood because they are not large enough to influence the surrounding cells. This conclusion was based on an experiment where they cut small transverse (earlywood and latewood) sections of Scots pine (*Pinus sylvestris*), and using optical microscopy, measured swelling anisotropy with and without ray cells present. The results showed the same trend for the two types of specimens.

However, recently Patera et al. (2017) used x-ray computed tomography to research earlywood-latewood interactions in moisture-induced swelling. They concluded that ray cells could have a measurable local restraint on moisture-induced swelling in the tangential swelling of softwood earlywood.

4.2 Materials and methods

4.2.1 Specimen Preparation

One loblolly pine (*Pinus taeda*) latewood specimen and six brominated phenol-formaldehyde (BrPF) bonded specimens prepared for a previous study (Jakes et al. 2015) were used. For the wood substrates, pristine tangential–longitudinal surfaces were prepared using a disposable microtome blade in a sledge microtome. In the adhesive formulation, phenol was replaced with 3-bromophenol. Although not measured quantitatively, BrPF with different molecular weight distributions were obtained by removing aliquots 45, 85, 115, 135, 155, or 175 minutes after the commencement of the condensation stage of the reaction; longer time in the condensation state was expected to create phenol formaldehyde (PF) with a shift toward a higher molecular weight distribution. Bondlines were made by applying enough BrPF adhesive to the pristine surfaces of two substrates to ensure abundant squeeze-out. After 5 min open assembly time, two substrates were clamped together using an office binder clip. After an addition 5 min, the assemblies were placed in a 155°C oven and cured for 45 min. The samples were then cut down to a 2 mm by 2 mm cross-section and a 10 mm length with the bondline centered in the cross-

section for the bonded specimens. Specimens were selected to be latewood on both sides of the bondlines; however, the 45-min and 115-min specimen also contain some earlywood away from the bondline in order to maintain the 2 mm cross section. The earlywood section of the 45-min specimen was used for some analysis where noted. No other specimens contain earlywood.

4.2.2 X-ray computed tomography

All the specimens were taken to beamline 2-BM of the synchrotron facility in the Advanced Photon Source (APS) at Argonne National Laboratory, Lemont, IL, USA, where they were imaged by x-ray computer tomography (XCT) using the parameters in Table 4.1. The relative humidity (RH) of the specimen environment was controlled during imaging using a custom-built humidity chamber (Figure 4.1). The chamber consisted of 6.3 cm length of Kapton© tube with 127 μm thick walls and 4.45 cm outside diameter (Precision Paper Tube Company, Wheeling, IL, USA) with machined aluminum caps at each end. The bottom cap had a ThorLabs™ (Newton, NJ, USA) kinematic mount to attach the chamber to the rotation stage. The bottom cap also had an air inlet through which compressed air, humidified with an InstruQuest (Coconut Creek, FL, USA) HumiSys™ HF humidity generator, flowed. The top cap had the air outlet. The RH inside of the chamber was continuously monitored by a Sensirion (Staefa, Switzerland) SHT1x sensor.

4.2.2.1 Dynamic absorption and desorption series

Three time-series of specimens absorbing and desorbing moisture were collected. The first series captured the dynamic desorption behavior of the unbonded latewood loblolly pine specimen. The specimen was conditioned at 96% relative humidity (RH) for 24 hr prior to imaging at 96% RH. Then the RH was decreased to 0% RH and consecutive sinograms were taken over the next 6

hr. Within 1 min of the RH decrease, the chamber RH decreased to less than 2% RH.

The second and third series captured the dynamic sorption behavior of the 135 min BrPF bondline. The specimen was conditioned at 99% RH initially and then the RH was decreased to 0% and sinograms collected periodically over the next 6 hr. After the step change to 0% RH, it took about 2 min for the chamber RH to decrease to less than 2% RH. After the imaging at 0% RH for 6 hr, the RH was increased to 99% and sinograms were taken over the next 3 hr. During the step change to 99% RH it took about 2 min for the chamber RH to reach 97% RH.

4.2.2.2 Non-dynamic absorption

A BrPF bondline from each of the six aliquots were conditioned under ambient humidity (13%) for 24 hr and imaged at 13% RH in the XCT RH chamber. Then they were conditioned for about 16 hr at 96% RH in an external RH chamber before being imaged at 96% RH in the XCT RH chamber.

4.2.3 Segmentation

Images were reconstructed into tomograms using TomoPy (Gürsoy et al. 2014), then segmented into 4 phases: air, wood, wood-adhesive mixture, and pure adhesive using the methods described by (McKinley et al. 2016).

4.2.4 Digital Volume Correlation (DVC)

Strains in specimens caused by moisture sorption were evaluated using digital volume correlation (DVC). The reconstructed XCT volumes were correlated using Vic-Volume by Correlated Solutions Inc. (Columbia, SC). The correlation parameters are shown in Table 4.2. Using two separate scans of the same unchanged specimen as a noise floor measurement, one standard deviation of the measurement uncertainty is expected to be below 0.4×10^{-3}

strain for the transverse directions, and 0.85×10^{-3} strain for the longitudinal direction (Figure 4.2).

4.3 Results and Discussion

4.3.1 Volume change in unmodified loblolly latewood

The bulk measured swelling of all known softwood lumber is observed to be larger in the tangential direction than in the radial direction (Glass and Zelinka 2010), so it was unexpected to observe that the radial swelling was twice that of tangential swelling in both the unmodified latewood specimen (Figure 4.3) and the latewood in the adhered specimens (Figure 4.4 and Figure 4.5). However, this swelling anisotropy is explained by the anisotropic cellular materials finite element model developed by (Rafsanjani et al. 2013); the results of this model are summarized in Figure 4.6. Because of the large angle between the radial and tangential walls (θ) and the low aspect ratio (ξ) for the specimens in this study, the model predicts a larger bulk radial expansion than tangential expansion in the latewood regions and the opposite trend in the earlywood region. To confirm that the observed behavior was predicted by this model, the cell wall geometry of our specimens was measured (radial lengths, tangential lengths, angles, cell wall thickness) in cross sections of the tomography. The only assumption of the model which was not confirmed in the present study is that the moisture-induced swelling of the cell wall is ten times larger in the perpendicular-to-cell-wall-surface than the parallel-to-cell-wall-surface (and not longitudinal) directions. The reader is referred to Rafsanjani et al. (2013) for more details of the model. A comparison of the model predictions and measured bulk anisotropy of specimens from Derome et al. (2011) and the present study are shown in Table 4.3.

The average radial and tangential strains along the longitudinal direction, shown in (Figure 4.7), revealed that the outside edges of the specimen shrink before the center. This was expected, and it occurs because the moisture

desorption is a diffusion limited mechanism. Below fiber saturation, moisture may travel through the wood either along the cell wall as bound water or along the lumens as a gas. For more information about moisture transport in wood, the reader is referred to (Time 1998).

4.3.2 Local effect of ray cells on volume change

Volume change from wet to dry was calculated from DVC strain results for first and last scan of the unbonded loblolly pine specimen. The measured effect of the presence of ray cells is show in Figure 4.8. Fitting a linear model to the data predicts there is an average of 0.0488 *less* contraction around the ray cells when compared with non-ray regions during drying. This effect is only visible when looking at the tangential strain component of large fusiform rays (Figure 4.9a). There was no visible effect of any type of ray on the radial swelling of the wood (Figure 4.10e,f); this agrees with the findings of (Patera et al. 2017). For small rays, the effect is not large enough to be visible in the data (Figure 4.9b). The authors suggest the influence region of a uniseriate ray may be smaller than the sensitivity of digital image correlation because a correlation window size around 50 microns cannot resolve deformations only 10 microns wide when their magnitude is an order smaller than their surroundings.

4.3.3 Volume change in BrPF bonded specimens

The local strains in the radial, tangential, and longitudinal directions for the BrPF bonded specimens at each curing time are shown in Figure 4.4 and Figure 4.5. Like in the unbonded loblolly latewood specimen, the radial moisture-induced swelling is larger than the tangential moisture-induced swelling.

While there is no evidence of condensation time dependence, Figure 4.4 and Figure 4.5 show that the adhesive locally reduces the moisture-induced swelling. Interestingly, both tangential and radial strains show an effect of local

adhesive volume fraction, but the radial swelling is the only one strongly affected by bondline proximity. Radial expansion of the wood was greater than tangential expansion, so moisture expansion mismatch between the isotropic adhesive and the anisotropic wood may cause some of the effect. However, the shape of the strain fields in the bonded specimens suggest that the morphology of the adhesive has a significant effect on local moisture induced swelling.

Figure 4.10a-d show sections of bondline from some of the bonded specimens. In Figure 4.10a,c, you can see that the area of low radial strain (these specimens are swelling) follows the contours of the adhesive. We can see that the low strain region bulges out with adhesive filled rays. Figure 4.10b,d show tangential strains around adhesive filled ray cells. The tangential strains are reduced along the entire length of the rays unlike the radial strains effect which only extends from the bondline along the rays part way. Notably, in most cases the radial strain effect along the ray terminates at a bubble in the adhesive. This leads the authors to believe that bubbles and swelling induced adhesive fracture may also limit the ability of the adhesive to restrain swelling over long distances. Evidence of cracks is shown in Figure 4.11 where the adhesive from an adhesive filled ray cell appears to develop cracks in three places during expansion. It seems that the adhesive is effective at depressing the swelling across its narrow dimension, but not along the length dimension. In rays, it effectively resists tangential swelling but not radial swelling, and at the bondline, it effectively resists radial swelling, but not tangential swelling.

4.3.4 Adhesive volume change

Measuring the swelling of the adhesive in situ has proven difficult; multiple methods were attempted, but none proved satisfactory to the authors. Digital image correlation cannot be used because the adhesive is structure is

too featureless and interwoven with the wood structure to be accurately correlated.

$$dV = \frac{\left(v_{final} - v_{initial}\right)}{v_{initial}}$$

4-1

Measuring volume change directly by using the total numbers of voxels tagged as adhesive only in the segmented before and after tomography also proved unsatisfactory. Using Equation 4-1, the volume change, dV, was calculated by using v_final, the number of voxels tagged as adhesive in the dry specimen, and $v\_initial$, the number of voxels tagged as adhesive in the wet specimen. The results of this calculation are shown in Figure 4.12 as a function of condensation time for each of the BrPF specimens. Assuming isotropic expansion, the linear expansion of the adhesive, α_l, can be estimated from the volumetric expansion, α_v, of the adhesive using Equation 4-2. This conversion is shown on the right axis of Figure 4.12 for better comparison between other strain data in this paper.

$$(1 + \alpha_l)^3 = 1 + \alpha_v$$
$$\alpha_l = \sqrt[3]{1 + \alpha_v} - 1$$

4-2

Only the 300 microns of distance on either side of the bondline were used for the calculation because the volume change was shown to converge at this region size. Using this method, the magnitude of the volume change is opposite of expected. These specimens are undergoing absorption, so the volume of the adhesive is expected to increase along with the wood cell material.

The authors suggest two possible explanations for this behavior. First, the changing density of all the materials as they uptake moisture causes a shift in their x-ray attenuation. This changes the attenuation threshold between the cell wall material and the adhesive. In particular, it shifts the histogram of the tomography to lower intensities; this is the expected behavior because wet cell

wall material is less dense than dry cell wall material (Siau 1984). Because of this shift, using the same threshold for both images would cause less adhesive voxels to be identified in the wet image, which would lead to a negative volume change of adhesive. However, even segmenting each before and after image independently leads to the unexpectedly opposite adhesive contraction, so it seems that segmentation uncertainty due to changing density is too high to make this measurement.

Second, the adhesive in the lumens of tracheids and ray cells, which make up a majority of the segmented adhesive, could be under compression in the wet state. We already know that the cell wall material expands more perpendicular-to-cell-wall-surface than in the parallel-to-cell-wall-surface directions, and in a personal communication, Joseph Jakes stated that the lumen space of latewood loblolly pine shrinks as the cell uptakes water. However, for the wet cell wall to compress the wet adhesive, the modulus of the cell wall would need to be greater than the modulus of the adhesive. The elastic modulus for phenol-formaldehyde in the literature is approximately 3.5 GPa ("Phenol Formaldehyde (PF, Phenolic)" n.d.; EFunda 2018). Then, let's assume that the radial and tangential moduli of the cell walls are approximately one half of the longitudinal moduli as Brandt et al. (2010) observed when they nanoindented *Pinus sylvestris L.* latewood. Jakes et al. (2015) measured the moduli of our specimens to be about 15 GPa in the longitudinal direction of wood at 78% relative humidity, so the moduli is 7 GPa or less in the tangential or radial directions. This means that plausibly, the wood cell material in our specimens could be compressing the adhesive in the cell lumens.

The final attempt to measure the volume change of the adhesive was by directly measuring dimensional changes of specific objects of adhesive in the tomography. Two methods were utilized. First, adhesive objects in lumens and ray cells located between two bubbles were measured along their longitudinal

and radial lengths respectively. The results in Table 4.4 appear to show that linear measures of adhesive object dimensions follow closely with the dimensional changes of the bulk wood. However, unconstrained, the adhesive is expected to exhibit isotropic swelling, which is contrary to the measured result, so it appears that the adhesive in the rays and lumens is affected too highly by the adjacent cell walls to get a fair measurement of the adhesive alone. The dimensional change of the adhesive in these regions, measured using this method and the previous method, is biased by the dimensional change of the wood cell walls. Second, the change in volume of adhesive bubbles, which were located at the bondline between substrates, but not touching either, was measured. We expect that if these bubbles are located at the bondline, and are not touching the wood cell material, they will expand isotropically because they would be unaffected by compression stresses created by interaction with the wood. The 25 bubbles that were located at the bondlines and not touching wood cell material have a large variance, but their mean linear expansion of 23 x 10^{-3} is a much more reasonable estimate of the adhesive expansion because it doesn't closely match the bulk wood expansion. There are not enough bubbles in the specimens to measure the adhesive expansion more confidently, and even this method may be influenced by the surrounding wood cell material. A better method for measuring the adhesive moisture-induced swelling would be preferable.

4.4 Conclusions and future direction

A method for measuring the effects of adhesive bondlines on moisture-induced swelling of wood structure *in situ* has been demonstrated.

The spatial limitations of current DVC methods prevented detection of any influence of uniseriate ray cells on the moisture-induced expansion of the wood structure. However, adhesive-filled rays, and large fusiform rays, clearly created local reductions of moisture-induced swelling in the tangential direction.

The results suggest that the condensation stage of the reaction (by proxy the molecular weight) of the PF adhesive used in this study does not affect the wood swelling because it was approximately the same for all specimens.

Swelling reduction from the adhesive was observed only to occur radially near the bond plane and tangentially near adhesive-filled rays. The strain maps suggest that breaks in the adhesive due to bubbles and adhesive fracture prevent the adhesive from arresting swelling along its longest dimension. Also, the local effect of the adhesive bond on the wood was less than the effect of the earlywood-latewood transition.

Depending on the method of measurement, moisture-induced swelling of adhesive was different than the wood cell wall. However, there appears to be interaction between the cell wall and the adhesive during swelling.

4.5 Tables

Table 4.1 A summary of XCT scanning parameters for specimens in this study.

Scanning Parameters	Value
beam energy	Polychromatic beam 27 keV peak energy
detector distance	110 mm
exposure time	5 ms
number of views	1500
Resolution	1.1 µm

Table 4.2 DVC parameters used to calculate strain in this study.

Parameter	Value
Strain Filter Size	5
Step Size	30
Window Weights	Uniform
Interpolation	Optimized 4-tap
Correlation	NSSD
Consistency [pixels]	0.33
Confidence [pixels]	0.02
Matchiness [pixels]	0.01
Strain Calculation	LaGrange

Table 4.3 Summary of measured geometric parameters (Figure 4.6) and moisture-induced swelling coefficient (β) anisotropy for earlywood and latewood in Norway Spruce and Loblolly Pine.

Specimen	Angle (θ)	Aspect Ratio (ξ)	t/h	Model Predicted anisotropy (βT ? βR)	Observed anisotropy (βT / βR)
Norway Spruce earlywood (Derome et al. 2011)	0 – 15 degrees	0.5 – 2.0	-	βT > βR	2.53
Norway Spruce Latewood (Derome et al. 2011)	23 +/- 10 degrees	0.79	0.39	βT > βR	1.22
Loblolly Pine earlywood	20 +/- 9 degrees	0.85	0.14	βT > βR	3
Loblolly Pine latewood	30 – 45 degrees	0.62 – 0.69	0.70	βT < βR	0.6

Table 4.4 Summary of manual measurements taken of adhesive features to determine in situ volume expansion of the adhesive. Direction refers to orientation of wood structure.

Specimens	Feature	Direction	Mean strain (linear)	95% CI	Sample size
85	adhesive globule	Longitudinal	0.002	0.003	5
45	adhesive globule	Radial	0.125	0.009	3
85,115, 135,155	bubble volume	-	0.023	0.021	25

4.6 Figures
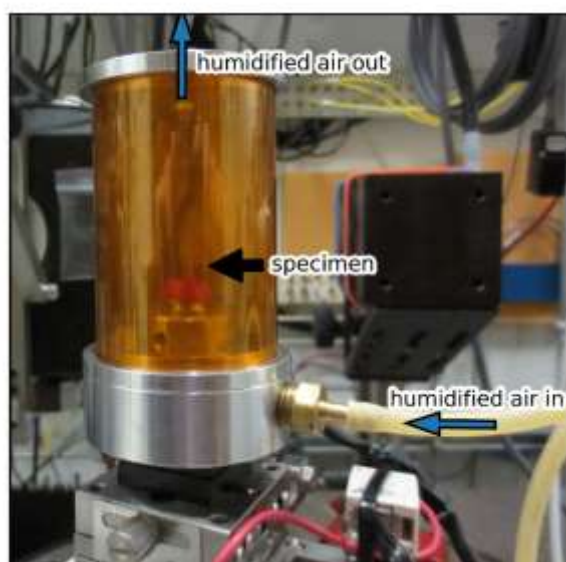
Figure 4.1 Image of the RH chamber installed at the beamline for this study.
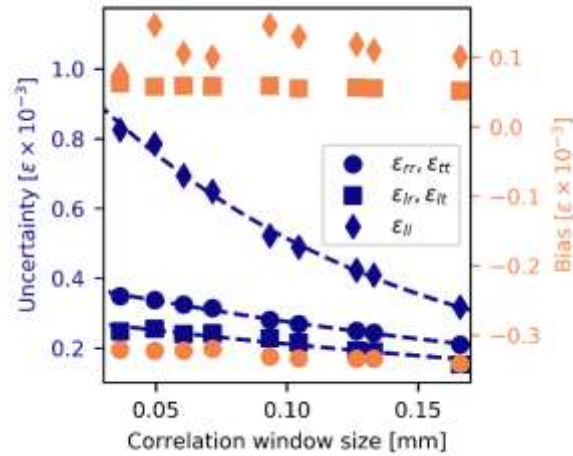
Figure 4.2 The measured strain uncertainty (one standard deviation of the error) and strain bias (mean error) of DVC at various correlation window sizes.
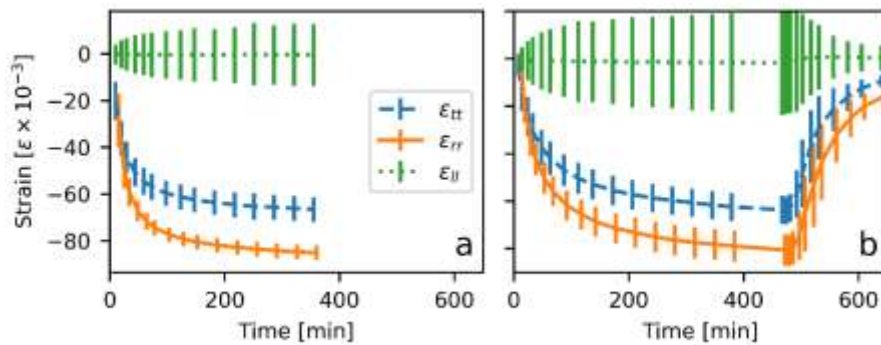
Figure 4.3 DVC measured strains in the (a) latewood loblolly pine specimen and (b) BrPF bonded specimen with adhesive condensation time of 135 min. Bars show ± one standard deviation.
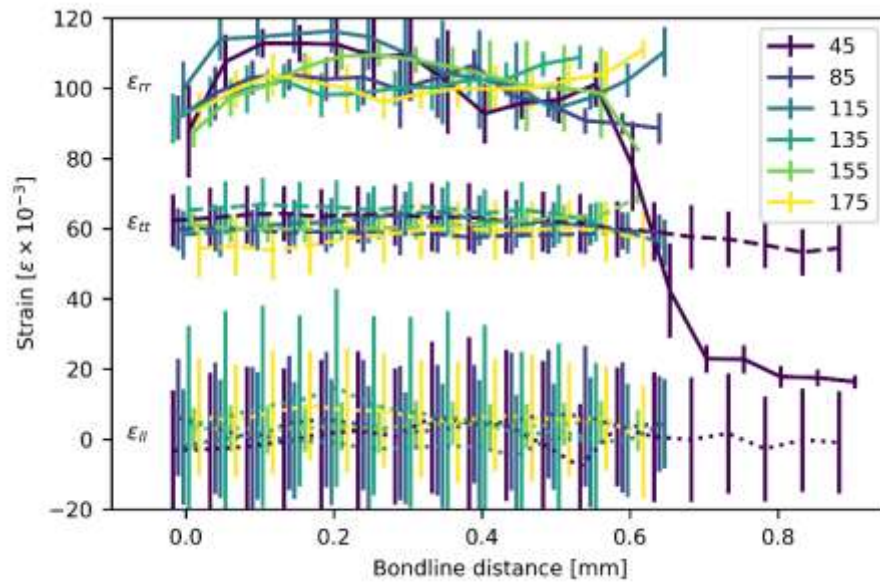
Figure 4.4 Strains of BrPF bonded specimens for condensation times from 45 to 175 min as a function of bondline distance. Radial strains of the 45-min specimen drop after 0.5 mm because it contains earlywood at the edge furthest from the bondline. Bars show ± one standard deviation.
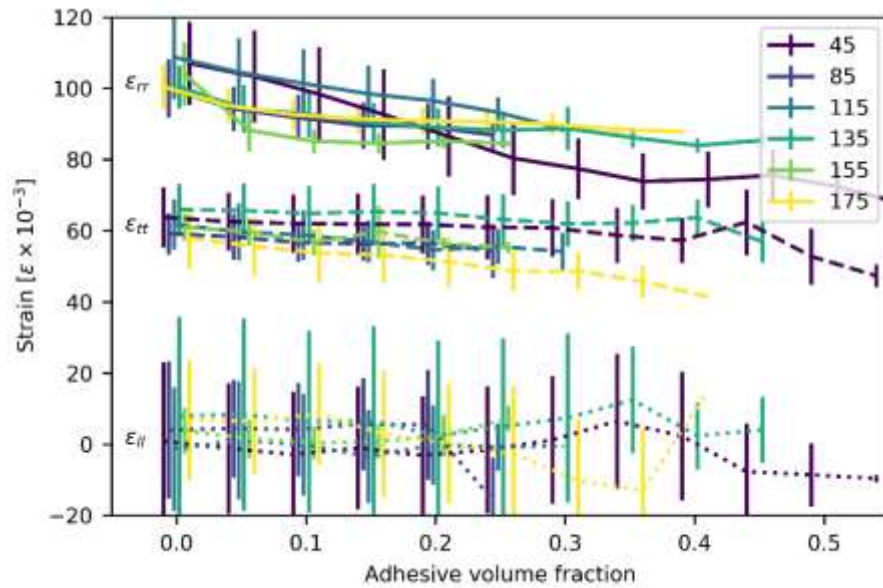
Figure 4.5 Strains of BrPF bonded specimens for condensation times from 45 to 175 min as a function of local adhesive volume fraction. Data from the earlywood region of the 45 min specimen is excluded. Bars show ± one standard deviation.
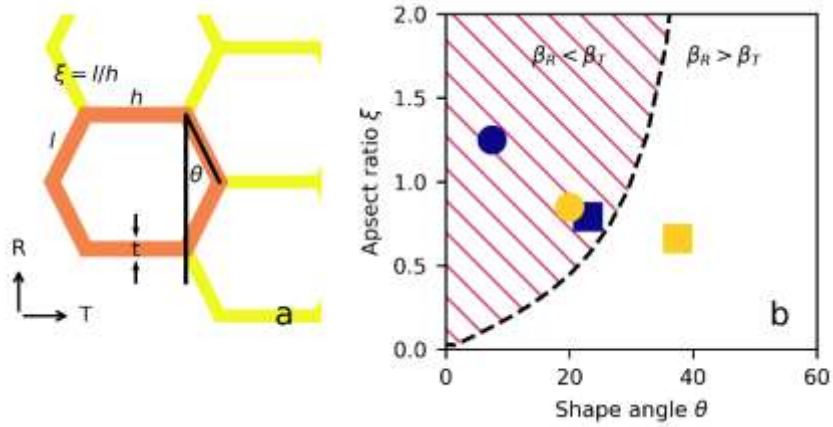
Figure 4.6 (a) Geometric parameters of cellular materials as defined by (Rafsanjani et al. 2013). (b) Summary of predicted swelling coefficient (β) anisotropy for specimens from two studies shown in Table 4.3. Dark shapes Norway spruce (Derome et al. 2011) and light shapes loblolly pine (Jakes et al. 2015). Earlywood circles and latewood squares.
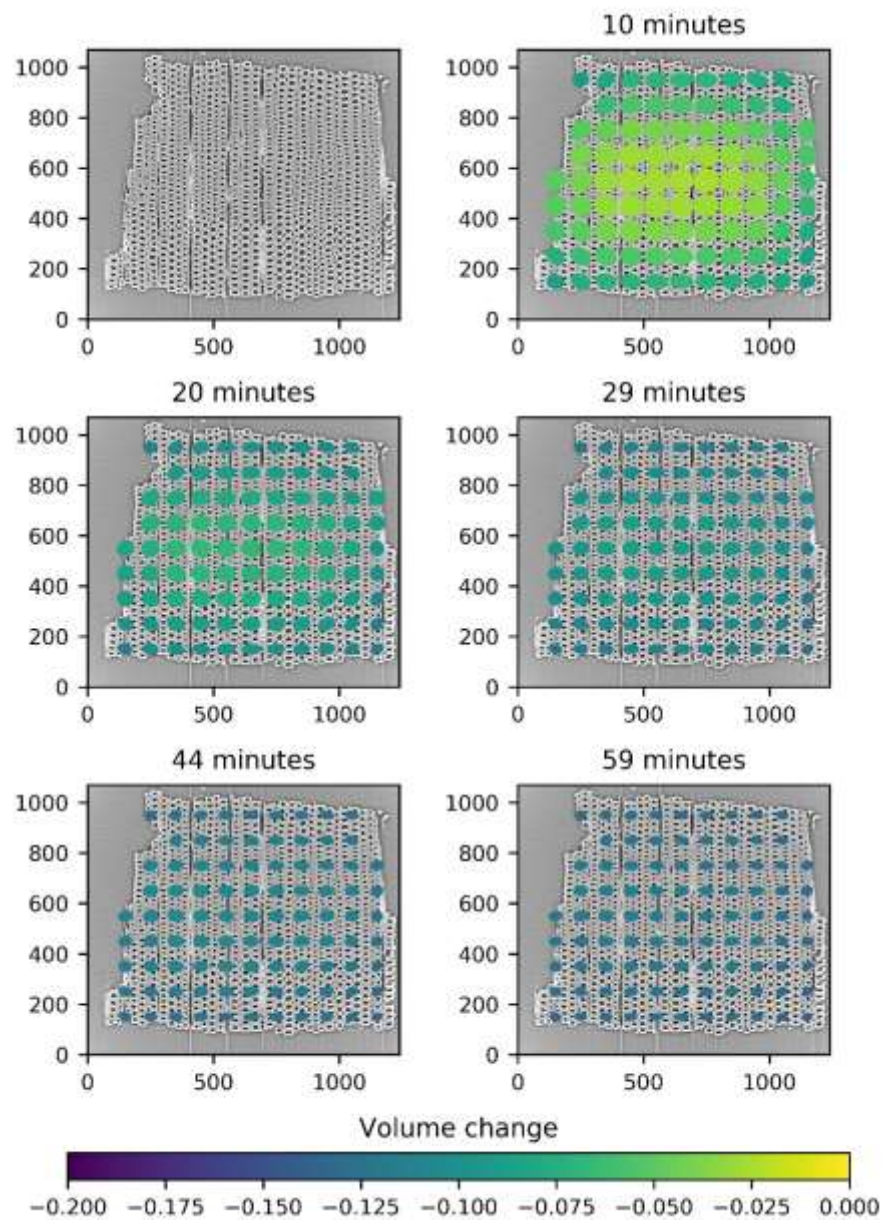
Figure 4.7 Elliptical glyphs showing strain development during drying (illustrated 10x measured strain) of the unbonded loblolly pine specimen averaged along the longitudinal direction. Colors show the magnitude of the actual proportional volume change.
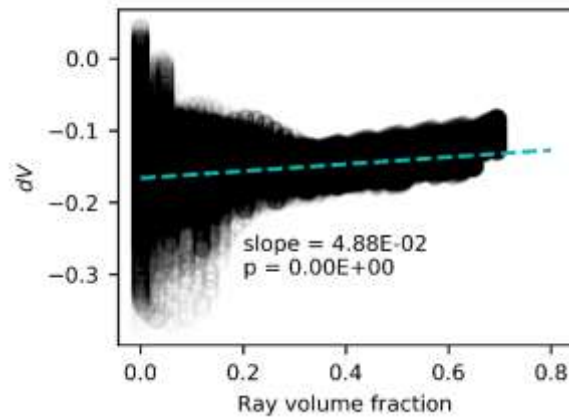
Figure 4.8 Dependence of DVC measured fractional volume change on the portion of correlation window filled with ray cell for loblolly pine specimen.
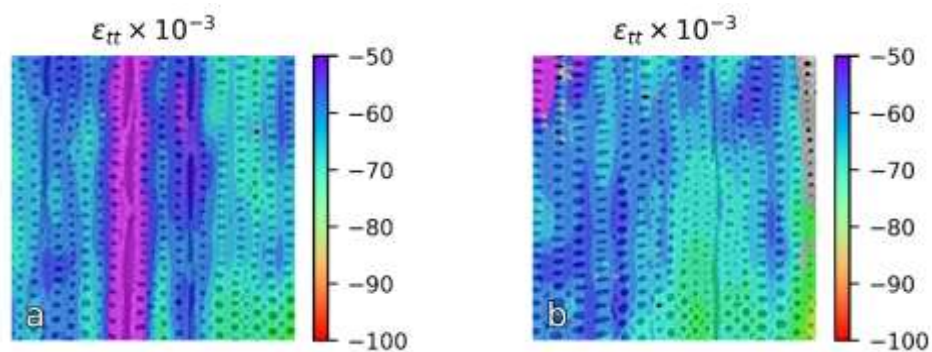
Figure 4.9 (a) Local effect of fusiform ray on moisture induced tangential strains in unbonded loblolly pine. (b) No visible effect from small ray cells in the same specimen.
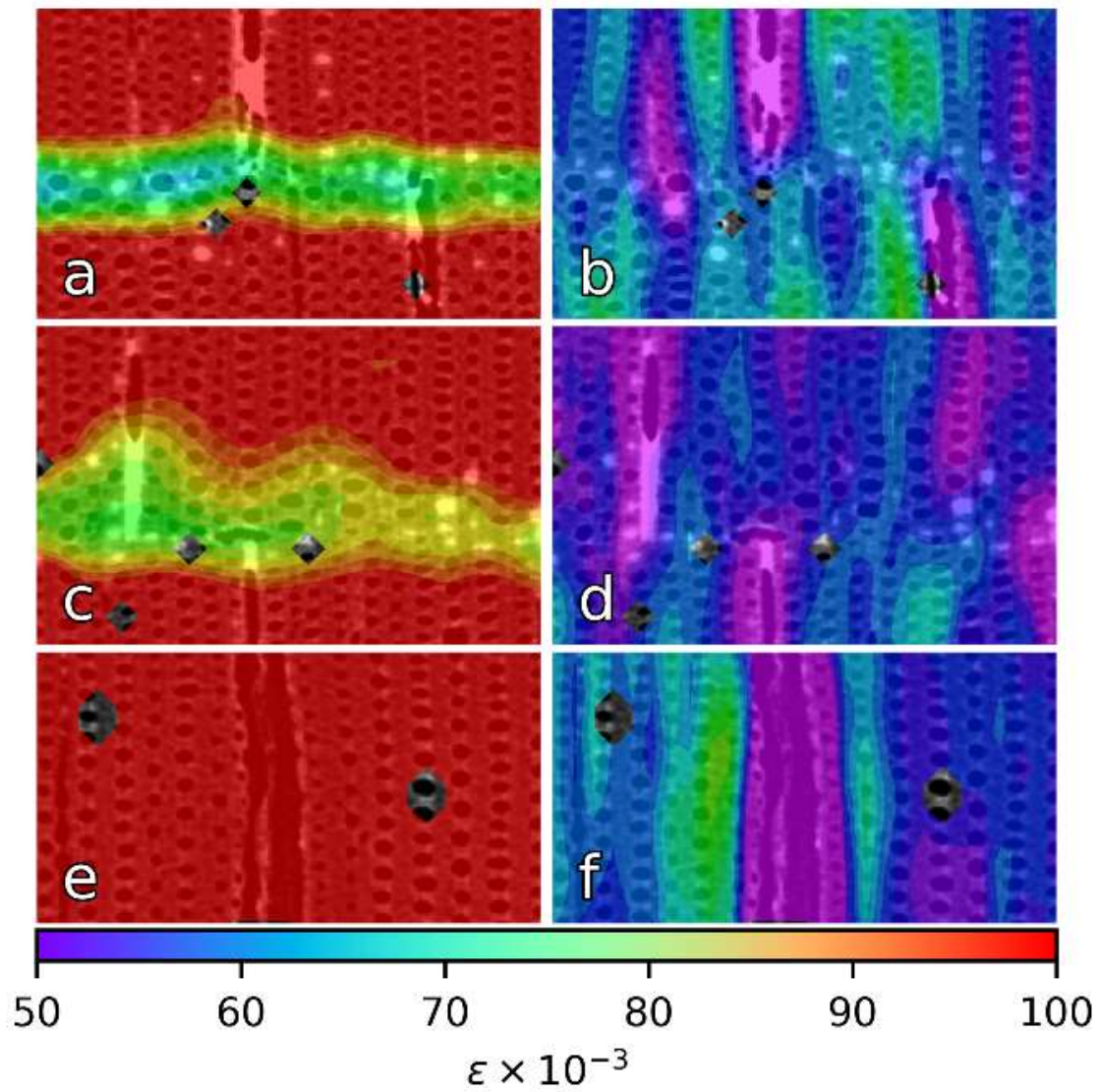
Figure 4.10 Radial strains (left) and tangential strains (right) in BrPF bonded specimens for (a, b) 45-min, (c, d) 85-min, and (e, f) 155-min specimens.
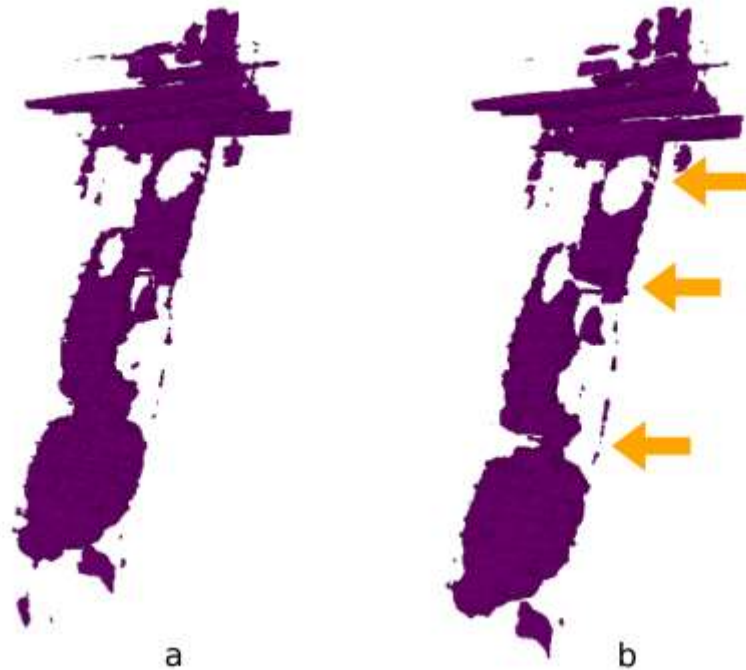
Figure 4.11 Dry and wet (left and right) 3D renderings of the same adhesive inside a ray cell. There are three visible breaks in the adhesive: one in the bubble closest to the bondline, one at the second bubble, and one two thirds of the way down the adhesive.
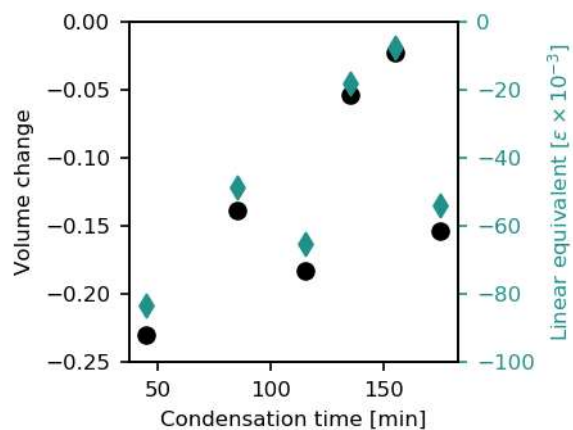
Figure 4.12 Volume change and equivalent linear strain of adhesive in BrPF bonded specimens as a function of condensation time of adhesive (increasing molecular weight). Results shown for calculations including only the region within 300 microns of the bondline.

5   XDESIGN: AN OPEN-SOURCE SOFTWARE PACKAGE FOR DESIGNING X-RAY IMAGING PHANTOMS

D. J. Ching and D. Gürsoy

The development of new methods or utilization of current X-ray computed tomography methods is impeded by the substantial amount of expertise required to design an X-ray computed tomography experiment from beginning to end. In an attempt to make material models, data acquisition schemes, and reconstruction algorithms more accessible to researchers lacking expertise in some of these areas, a software package is described here which can generate complex simulated phantoms and quantitatively evaluate new or existing data acquisition schemes and image reconstruction algorithms for targeted applications.

5.1 Introduction

Historically, X-ray imaging techniques have been developed by and for the medical imaging community and then adapted for other uses. However, this may be the cause of three common problems in synchrotron X-ray computed tomography (XCT) community: (1) the Shepp-Logan phantom (Shepp and Logan 1974) is still used as a standard phantom, but it does not represent the materials of a diverse synchrotron research community, (2) trying alternative acquisition schemes and experimental setups is difficult, especially for scanning probes, and (3) researchers are not quantitatively evaluating alternate reconstruction methods. These problems may still exist, in part, because developing the solution for each one requires developing solutions for the other two. However, since no one person is an expert materials scientist, physicist, and mathematician, these solutions have not been developed.

In order to bridge the gap between materials scientists, physicists, and mathematicians, we have created a modular software toolbox/framework (Figure 5.1) written in Python to help users and developers of synchrotron-based tomography to easily develop, validate, and share XCT experimental

methods. With XDesign, materials scientists can choose experimental methods based on phantoms they have created to resemble their actual materials of interest, physicists can optimize data acquisition methods using quantitative quality measures, and mathematicians can test their numerical algorithms on more diverse geometries and flexible input data.

This publication is organized as follows. Section 5.2 describes custom phantom generation capability. Section 5.3 describes data acquisition simulation. Section 5.4 describes reconstruction methods. Section 5.5 describes the quality metrics implemented in our toolbox. Section 5.6 describes features that are not implemented in the initial release but are planned pending community interest. Source code, documentation, and information on how to contribute are freely available through GitHub at tomography/xdesign.

All graphics are rendered using Matplotlib (Hunter 2007).

5.1.1 Why custom phantoms?

For many reconstruction studies, the simulated phantom of choice is the Shepp-Logan phantom, which is a piecewise constant model of a cross section of a human head, but for a majority of the materials community, this phantom does not represent the materials studied. For many of the same reasons that one acquisition setup does not fit all experiments, Shepp-Logan does not fit all simulations.

Using physical phantoms for quantitative procedural evaluation is not good practice because the exact dimensions or composition of the object are not known; this precision is important because researchers are already trying to resolve features and estimate quantities of interest at the limits of the tomographic instrument resolution and sensitivity.

Creating custom simulated phantoms is beneficial because it allows coupling of theoretical models with actual tomography. In fact, there are some

reconstruction methods which utilize an internal model material model as a key part of the reconstruction algorithm (Zanaga et al. 2016).

5.1.2 Related Works

There are open-source software tools for simulating data acquisition of non-X-ray systems: GATE (Jan et al. 2004), STIR (Thielemans et al. 2012), and k-Wave (Treeby and Cox 2010), and there are open-source tools that focus on different reconstruction methods: TXM wizard (Liu et al. 2012), MMX-I (Bergamaschi et al. 2016), ASTRA (van Aarle et al. 2015) and TomoPy (Gürsoy et al. 2014). However, most of these tools are not set up for custom data acquisition schemes for simulating streaming reconstructions. Some support different detection geometries such as cone- and parallel-beam geometries, but none support generic geometries for scanning probes. Materials properties which change over space-time can affect optimal data acquisition methods (Hsieh et al. 2006; Holman et al. 2016), and uniform spatio-temporal sampling is becoming undesirable as data sets become larger. Researchers are already developing streaming reconstruction systems with feedback to acquisition systems (Marchesini et al. 2016; Vogelgesang et al. 2016) because one acquisition setup may not fit the needs of all experiments or even a single experiment.

5.2 Phantom Generation

In XDesign, each phantom is a collection of multiple features. Features are represented by a geometry and some property functions which are valid within that geometry. A geometry is any sub-region of the phantom's ambient space. A property is what a probe measures in that geometry. It is best to think of a phantom as a piecewise property function in an N-dimensional (ND) space, and because in that way, features' properties such as density, attenuation, position, shape can be represented continuously in spacetime.

5.2.1 Building a Phantom

In the first release, XDesign supports 2D geometries including circles, triangles, and triangular meshes. It is possible to easily construct phantoms from the ground up by assembling geometry objects into features and then assigning them properties. The code below generates the phantom in Figure 5.3 and the structural hierarchy in Figure 5.2.

```python
# Create head
head = Feature(Circle(Point([0.5, 0.5]), radius=0.5))
head.mass_atten = 1
# Create left eye
eyeL = Feature(Circle(Point([0.3, 0.5]), radius=0.1))
eyeL.mass_atten = 1
# Create right eye
eyeR = Feature(Circle(Point([0.7, 0.5]), radius=0.1))
eyeR.mass_atten = 1
# Create mouth
mouth = Feature(Triangle(Point([0.2, 0.7]), Point([0.5, 0.8]), Point([0.8, 0.7])))
mouth.mass_atten = -1
# Assembly features to have a face phantom
face = Phantom() face.append([head, eyeL, eyeR, mouth])
```

5.2.2 Phantom Parameterization

You can parameterize phantom construction easily by defining a superclass of the Phantom class. For example, Figure 5.4 shows various outputs from the parameterized function below. This class randomly generates a foam-like phantom using void size range, gap, and target porosity as parameters.

```python
# Create a foam-like phantom from application specific parameters
foam_like_phantom = Foam(size_range, gap, porosity)
```

5.2.3 Structurally Complex Phantoms

The geometry module of XDesign has three main kinds of entities: simple entities (points and lines), curves (defined by a single equation), and polytopes (defined by multiple equations). We use the polytope library (Filippidis et al. 2016) for computational geometry because it made adding polygonal intersections and expansion into ND space easy. Curves and polytope meshes may be combined in the same phantom (Figure 5.5) in order to simulate complex structures like liquids wetting soils (Schlüter et al. 2014). Any number of properties can be added to the features in a phantom because Python allows for dynamic assignment of attributes to objects. Properties could be anything: attenuation, density, grain orientation, crystal structure, etc.

5.3 Data Acquisition Simulation

The XDesign data acquisition currently has one type of probe object. It takes measurements by integrating a property (e.g. linear attenuation) of the phantom over the space contained by probe. A single beam probe can simulate both scanning probes and area detectors because it can be moved and rotated to any position.

5.3.1 Generating a Sinogram

To simulate data acquisition, create a probe object and then code it through a procedure. The probe records data when the measure method is called, and it moves when translated or rotated. The example below simulates raster-scanning of the phantom from Section 5.2.1 with standard parallel beam over 180˚ rotation.

```python
# Define raster-scan parameters
sx, sy = 100, 100
# Step size of the probe for raster scanning
step = 1. / sy
# Initial probe creation
probe = Probe(Point([step / 2., -10]), Point([step / 2., 10]), 0.01)
# Step size of uniformly spaced projection angles
theta = np.pi / sx
# Initialize sinogram array
sinogram = np.zeros(sx * sy)
# Collect data
a = 0
for m in range(sx):
    for n in range(sy):
        # Calculate simulated data for measurement
        sinogram[a] = probe.measure(face)
        a += 1
        # Translate probe by step size
        probe.translate(step)
        # Translate probe back to original position
        probe.translate(-1)
        # Rotate probe by the angle step size around origin
        probe.rotate(theta, Point([0.5, 0.5]))
```

5.3.2 Implementation Details

Because scattering and other effects to the beam are not modeled at this time, there is no detector object. Equivalent sinograms can be generated by moving the phantom or the probe because all positions and movements are

described from a global reference frame. Streaming reconstruction can easily be simulated because simulated data is available as soon as it is calculated.

5.4 Reconstruction Algorithms

XDesign includes several unoptimized reconstruction algorithms for tinkering: ART, SIRT, and MLEM, but we expect for non-simulated experiments researchers will use more efficient implementations.

5.4.1 Reconstructing data

In XDesign, the Probe captures a snapshot of its geometry when it measures data and appends it in a list to be used for reconstruction. The example script below shows the use of built-in reconstruction methods in the package. Figure 5.6 demonstrates image reconstructions of the Soil phantom (Figure 5.7) on a uniformly spaced grid using Gridrec, PML, and SIRT algorithms.

```
# Reconstruction grid size
rx, ry = 100, 100
# Number of iterations
niter = 20
# Initial phantom estimate
init = np.zeros((rx, ry))
# Reconstruct using SIRT algorithm
recon = sirt(probe, sinogram, init, niter)
```

5.5 Image Quality Metrics

There are three classes of image quality metrics: full reference, partial reference, and no reference. Full reference metrics generally measure the amount of shared information between a reference and distorted image. The importance of different types of information: edge intensity, color, contrast is weighted differently in various methods, and the result is only applicable to a particular image. Partial reference metrics are used when the full reference

exists but is not reliably accessible. No-reference methods often try to measure the highest resolvable frequency or noise content of an image capturing system by using a standard test pattern; these quantities are believed to predict the quality of all images captured by a system. Our tool includes full reference and no reference metrics.

5.5.1 Full Reference Image Quality Metrics

This section briefly describes each of the available full-reference image quality metrics. For each of these metrics, scores closer to one are better. For full technical descriptions, the reader should refer to each method's original publication.

5.5.1.1 MS-SSIM

The multiscale structural similarity index (MS-SSIM) measures differences in "luminance, contrast, and structure" at multiple levels of detail (Wang, Simoncelli, and Bovik 2003). Each of these three qualities is calculated from a combination of the local mean, standard deviation, and covariance of images. Using local means and standard deviations calculated from Gaussian filters is possible to calculate a contour map of image quality at multiple resolution scales. Similarity overall is calculated by averaging the structural similarity index over the entire image and at each scale.

5.5.1.2 FSIM

The feature similarity index (FSIM) measures the similarity of images using gradient magnitude and Fourier phase congruency (Zhang et al. 2011). Because high phase congruency had been correlated with image features important to the human visual system (HVS), this method weights the importance of each gradient magnitude depending on phase congruency. Since the gradient magnitude is only a measure of edges, this method ignores

whether luminance is correctly captured, but that might not be important for some users.

5.5.1.3 VIFp

The visual information fidelity in the pixel domain (VIFp) measures shared information between a reference and distorted image using a framework based on natural scene statistics (Sheikh and Bovik 2006). It uses Gaussian scale mixtures and wavelet analysis. It directly compares the intensity information in the images at different scales by separating it into levels using Gaussian filters of different sizes. Because it uses wavelets, the accuracy of this quality metric is dependent on the depth of the wavelet transform.

5.5.2 No Reference Image Quality Metrics

These metrics use predetermined phantom geometries to estimate the noise characteristics and minimum resolvable spatial frequencies of a system (Hsieh and others 2009).

5.5.2.1 NPS

Noise power spectra (NPS) use a Fourier transform of uniform area in the reconstruction to give information about the frequency composition of the noise. This is better than SNR because it shows how coarse or fine the noise is. 2D images produce a 2D noise power spectrum, but the 2D spectrum can be reduced to a histogram by binning radially.

5.5.2.2 SFR and MTF

Spatial frequency response (SFR) and modulation transfer function (MTF) use commonly use a slanted edge or standard pattern of lines at increasingly smaller intervals to measure how the fidelity of an image decreases as the frequency of a signal increases. The ability of an imaging system to accurately capture high frequency signals is related to the sharpness of images it creates. We have implemented the MTF calculation described in (Friedman et al. 2013)

which does not normalize the zero frequency to unity in order to prevent artificially inflating responses at other frequencies.

5.5.3 Using Image Quality Metrics

In order to use the full reference quality metrics in XDesign you need to generate a reconstructed phantom, discretize the source phantom on a uniform grid to the same size, and choose a method for comparison. The compute quality function will generate average and local quality for a series of images.

```
# Create a discrete phantom of size 100
ref = discrete_phantom(a_phantom, 100)
# Compare true phantom with reconstructed values using MS-SSIM metric
metrics = compute_quality(ref, [rec_art, rec_sirt, rec_mlem], method="MSSSIM")
# Plot analysis results
plot_metrics(metrics)
```

For full-reference comparison, local quality information is calculated at multiple scales. Scale is the standard deviation of the filter size used to compute the local quality metric. In other words, the quality at scale = 5, tells you how well objects on the order of 10 pixels are represented. Figure 5.8 shows the result of compute_quality with the MS-SSIM metric applied to the "cameraman" test image which has been deformed in 4 different ways. The distorted image is plotted in the upper left and a sequence of contour plots of the quality metric are plotted for each scale. Larger plots show information about smaller scales and smaller plots show information about larger scales.

The combination of quality metrics at multiple scales and parameterized functions allows us to generate informative plots about an XCT experimental method. If we wanted to evaluate whether ART, SIRT, or MLEM, is optimal for reconstructing the Soil phantom (Figure 5.7), we can try each of the methods at different numbers of iterations and plot the results. Optimal tuning of configuration parameters of any iterative reconstruction algorithm (e.g.

regularization parameter, number of iterations, different updating schemes) can also be quantified by calculating this set of metrics.

In Figure 5.9, we can see that ART only scores best on smaller scales with few iterations. Beyond that, it creates its best reconstruction around 50 iterations before decreasing in quality again. MLEM is the best algorithm for this phantom because the quality reconstruction rapidly increases at all scales faster than ART and SIRT. The SIRT contour looks like the MLEM contour but the quality improves at a slower pace. SIRT might be a better option if its time per iteration is much smaller than that of MLEM.

We can also calculate no reference metrics using standard phantoms. In Figure 5.11, we have calculated the MTF for ART, SIRT, and MLEM at various numbers of iterations. In this comparison, it once again seems that MLEM is the best reconstruction method at higher numbers of iterations because the MTF most rapidly approaches unity.

5.6 Future Works and Proposed Features

5.6.1 Future Works

Here are some features which we are currently working on to add to XDesign.

5.6.1.1 Wave Propagation

XDesign only simulates beam attenuation, and it does not have a Detector object. Therefore, phase contrast and other reconstruction methods which use beam scattering or wave interference cannot be simulated at this time. In a future release, we are planning to simulate Fresnel multislice wave propagation.

5.6.1.2 Geometric flexibility

As a pre-release, XDesign only supports 2D geometries. We are currently working to enable the definition of higher dimensional Phantoms which will

enable freedom of problem definition and allow for more flexible data acquisition. e.g. 3D objects can be used to model 3D objects, but they can also be used for modeling a dynamic 2D object. We also plan to add a Component class to the phantom hierarchy. Components will spatially attach Features of different properties together to allow for easier geometric manipulation.

5.6.1.3 Performance

Python is slower than compiled languages. We are working to optimize computationally intensive portions of the data acquisition module for faster run-times. We plan to implement bottleneck functions in compiled languages such as C or Fortran and explore use of Graphical Processing Units for vectorizing and further speeding-up calculation of slow processes if needed.

5.6.2 Proposed Features

Here are some features which have been suggested but are not yet assigned to anyone for development. Features in this section are not currently planned because they either require greater involvement from the community or more man-hours. For additional feature suggestions or to participate in our development process, please head to our GitHub page and create an issue.

5.6.2.1 Distortions

Some processing methods are targeted at reducing a specific type of noise e.g. motion blur or beam drift. At this time, simulated distortions like these are not implemented, but they could be simulated by adding random noise to methods in the data acquisition module.

5.6.2.2 Materials definitions

Currently, Feature properties must be defined manually. We could define a materials superclass of Feature for common compounds such that materials properties of these compounds are auto populated from tabulated data of the

National Institute of Standards and Technology (Berger and Hubbell 1987) or the Center for X-ray Optics (Henke, Gullikson, and Davis 1993).

5.6.2.3 Interfaces

Import and export of experimentation acquisition systems for better determining collection parameters is important. We could implement import and export interfaces to common file formats like *stl* for 3D meshes and *svg* for 2D phantoms. This would improve portability of phantoms and acquisition geometry between researchers. It could also allow for the visualization of experimental setups by using third party commercial tools and make integration with existing tools easier.

5.6.2.4 Improved Quality measures

Some algorithms are specialized for reconstructing the shape only, and thus, the dynamic range of the phantom may not match the dynamic range of the reconstruction. Full reference quality metrics that can compare images of different dynamic ranges will be useful if they can be implemented. We could expand metrics library to evaluate special reconstructing methods based on community interest.

5.6.2.5 Community *Repository*

A collection of free to use materials phantoms generated by the community would help algorithms developers test their methods more robustly. We are working with synchrotron users to build up a parametrized phantoms library and encourage anyone to contribute their custom parameterized phantoms to the XDesign GitHub repository.

5.7 Figures
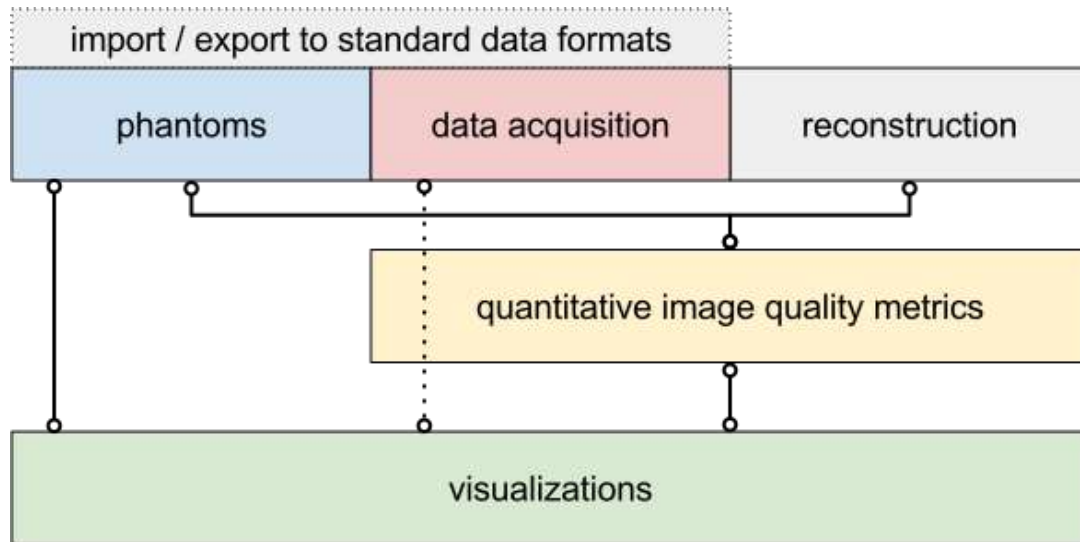
Figure 5.1 Modular schematic of XDesign. Implemented modules are drawn in solid boxes and proposed modules are drawn in dotted lines.
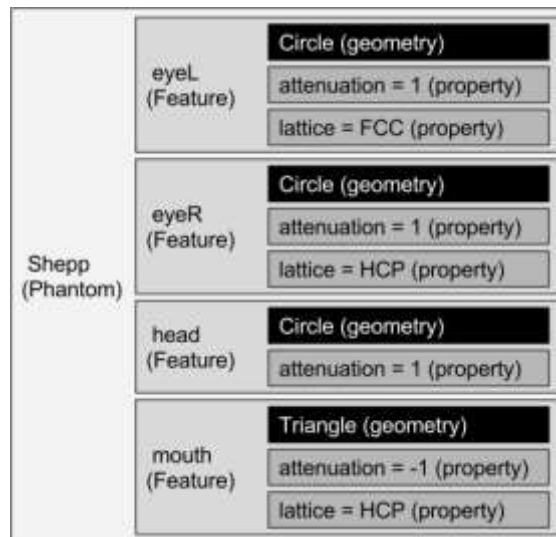
Figure 5.2 Example phantom data structure for phantom described in Section 2.1 and Figure 5.3.
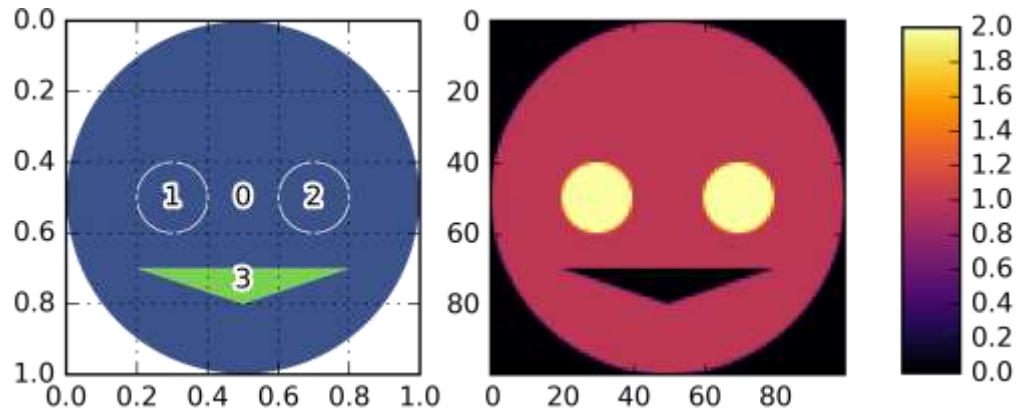
Figure 5.3 Geometry (left) attenuation property (right) of a simple phantom described in Figure 5.2 and Section 5.2.1.
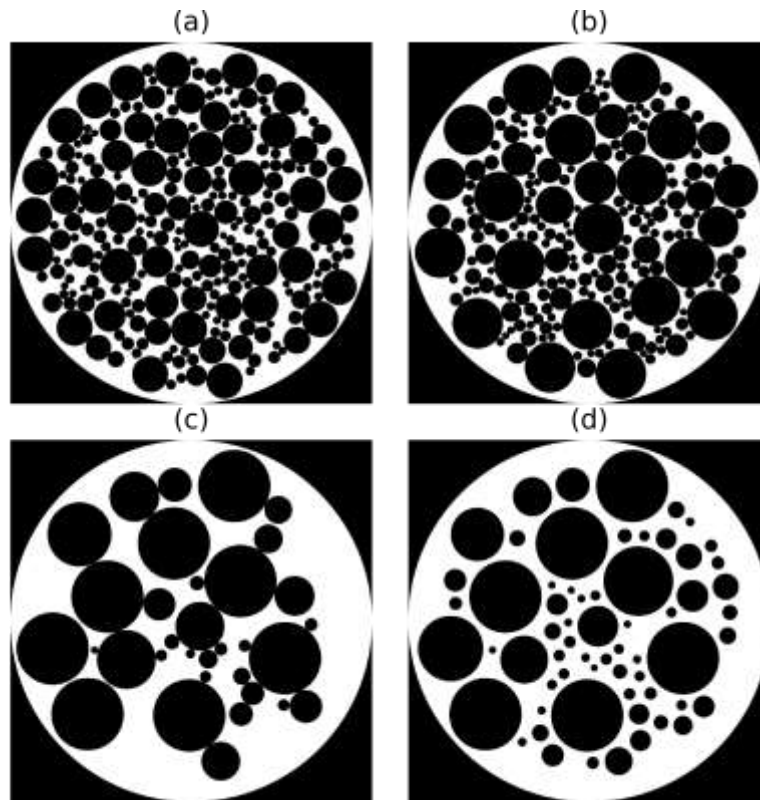
Figure 5.4 Four different foam-like phantoms generated from the parameterized function in section 2.2. (a) size range=[0.05, 0.01], gap=0, porosity=1; (b) size range=[0.07, 0.01], gap=0, porosity=0.75; (c) size range=[0.1, 0.01], gap=0, porosity=0.5; (a) size range=[0.1, 0.01], gap=0.015, porosity=1. Foams based on appearance of tomography collected by (Patterson et al. 2016).
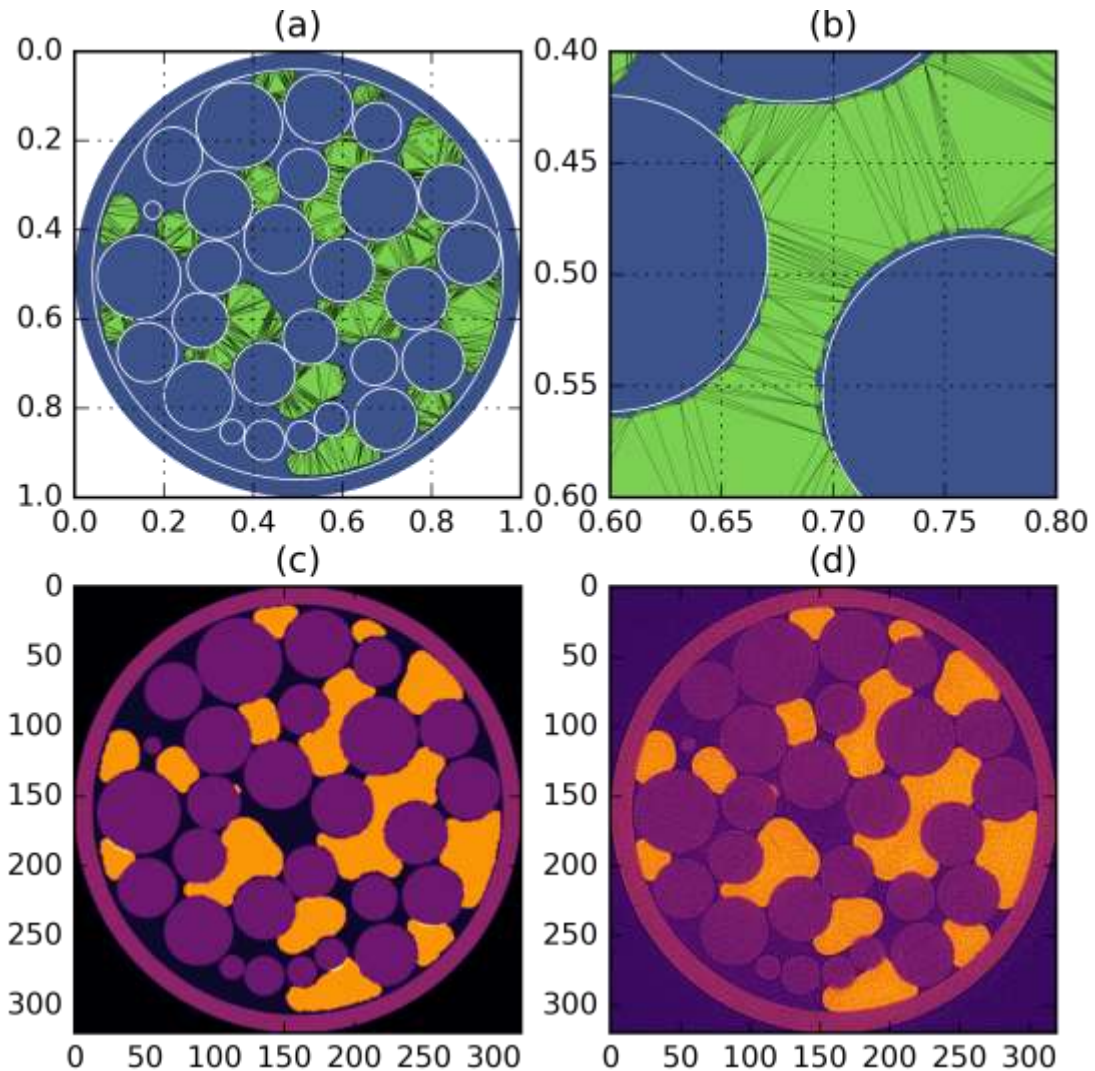
Figure 5.5 Soil-like phantom (a, c) with wetting phase constructed from triangular mesh (b) and two other phases constructed from circles to resemble a source image (d) as seen in (Narter and Brusseau 2010). The circles were extracted from the source image using canny edges and a Hough transform. The wetting phase was extracted from the source using simple thresholding, converted to a contour using the marching squares algorithm, and then converted to a triangular mesh using Python Triangle (Rufat 2013).
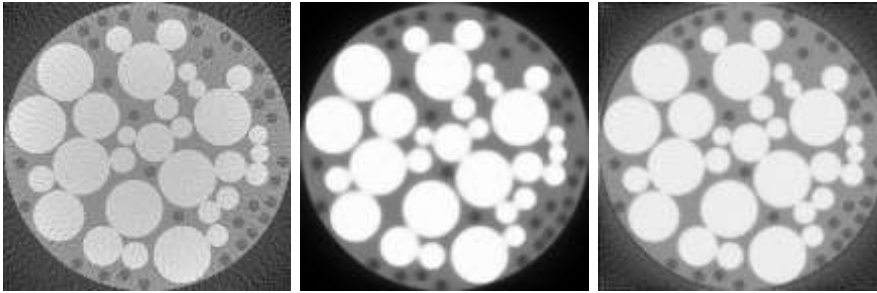
Figure 5.6 Image reconstructions of the soil phantom on a uniformly spaced grid using Gridrec, PML and SIRT algorithms. We employed TomoPy for obtaining Gridrec and PML reconstructions, and XDesign for obtaining SIRT reconstruction.
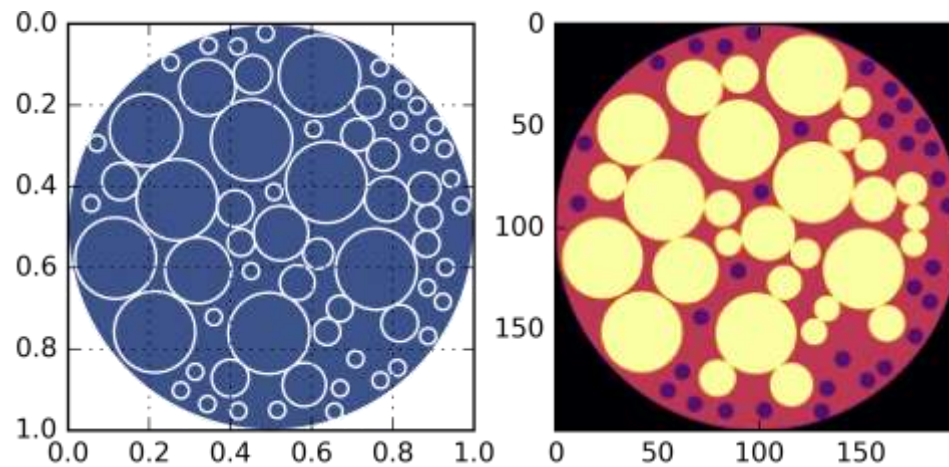
Figure 5.7 The Soil phantom geometry (left) and its discretization (right) are shown.
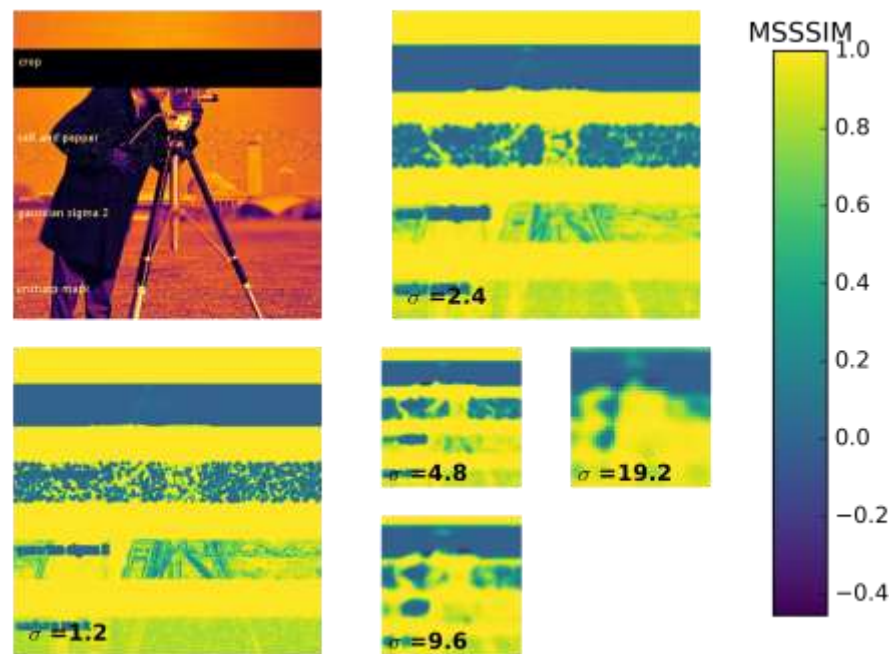
Figure 5.8 Example output from compute quality using MS-SSIM quality metric. The source image is the "camera man" image which has been distorted in 4 ways: crop, salt and pepper, Gaussian smoothing, and unsharp masking.
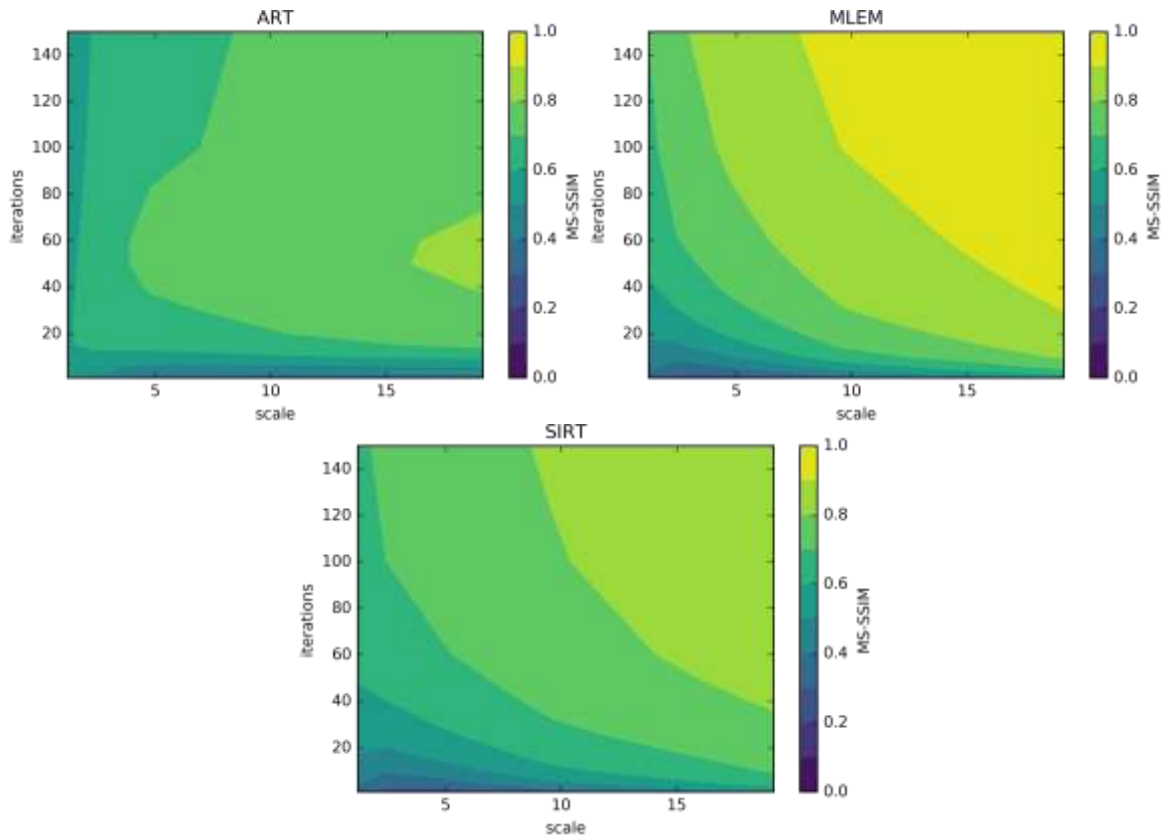
Figure 5.9 MS-SSIM quality contours for the reconstruction of the Soil phantom in Figure 5.7 using ART, MLEM, and SIRT reconstruction. 1.0 is the best score.
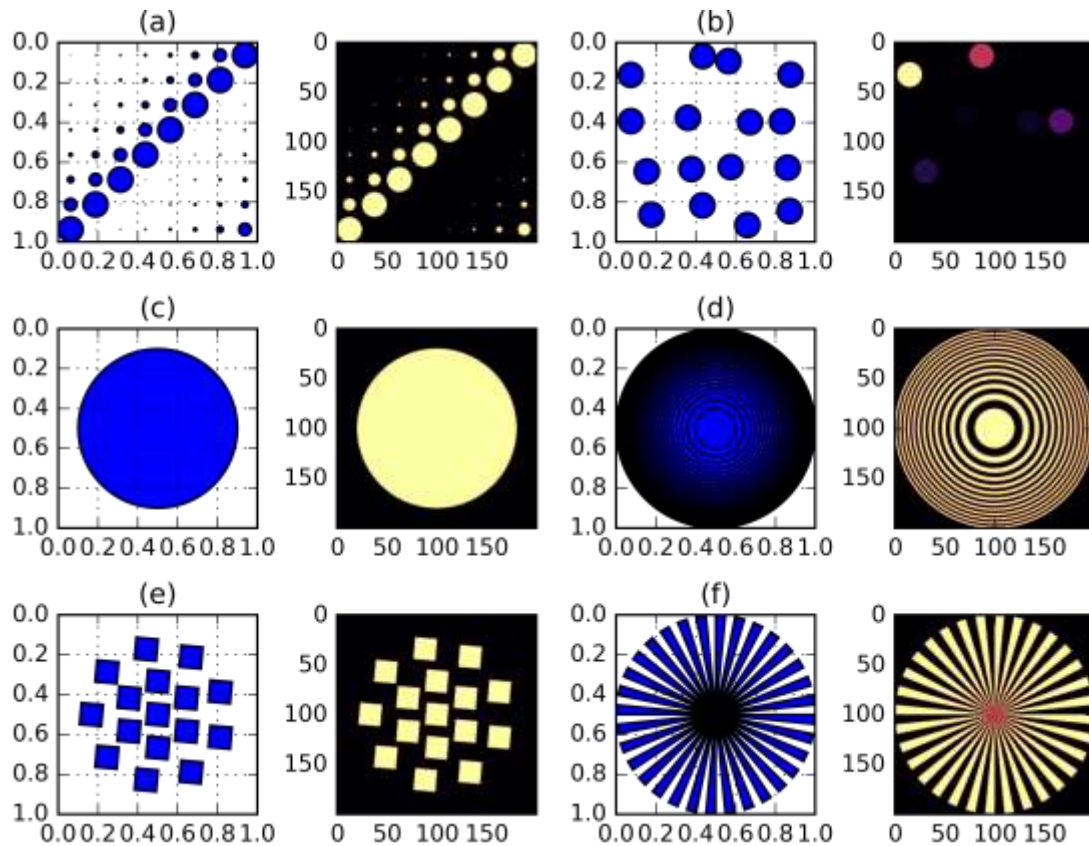
Figure 5.10 Other parameterized phantoms: (a) Latin square of different sizes, (b) random circles of varying levels of attenuation, (c) a unit circle, (d) lines of increasingly smaller width, (e) slanted squares, (f) Siemens star. (a, b, e) could be used for studying the effects of reconstruction on objects of different sizes and attenuation. (c) could be used for noise reduction studies. (d, f) could all be used to calculate the modulation transfer function (MTF).
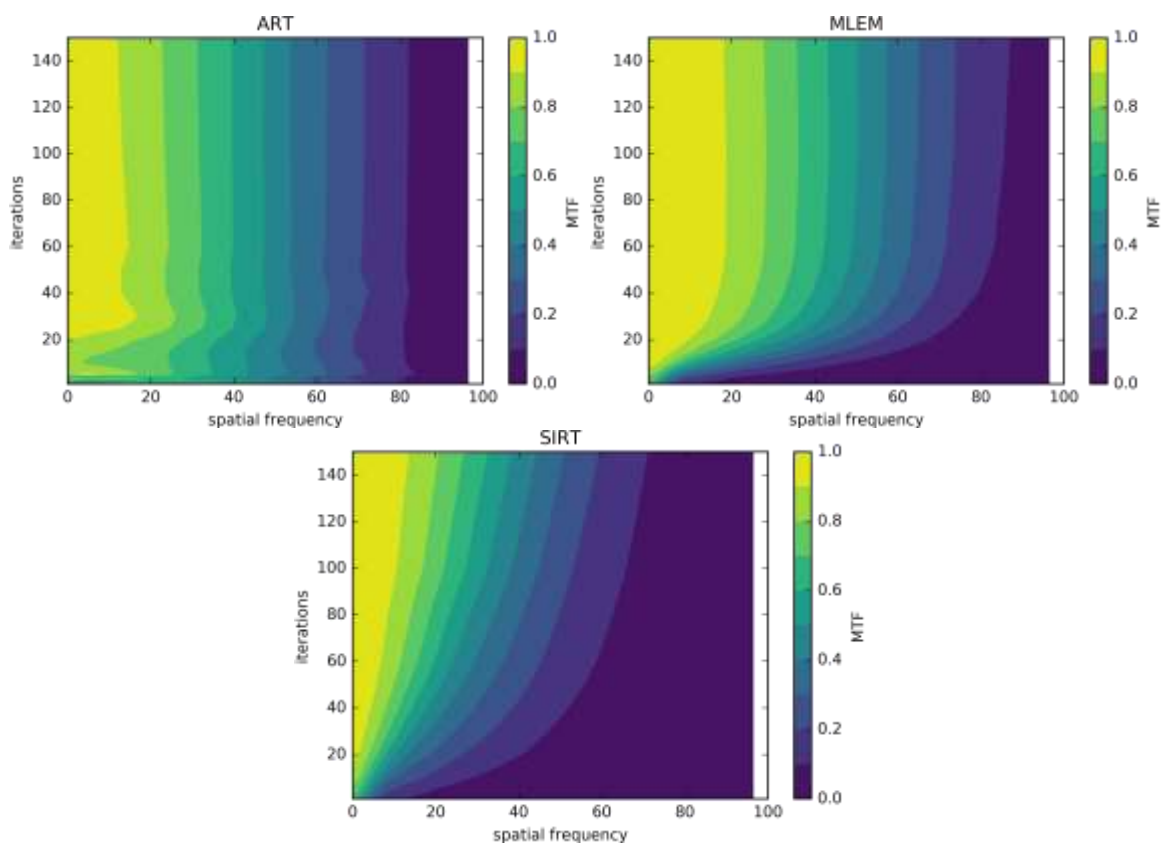
Figure 5.11 Modulation transfer function (MTF) quality contours from the unit circle phantom in Figure 5.10 using ART, MLEM, and SIRT reconstruction. MTF values at zero-frequency are not normalized to unity according to (Friedman et al. 2013). 1.0 is the best score.

6   THE EFFECT OF PROCEDURE COVERAGE ON TOMOGRAPHIC RECONSTRUCTION QUALITY OF SCANNING PROBE MICROSCOPY

D. J. Ching and D. Gürsoy

A tool was developed for visualizing the planar coverage of an arbitrary two-dimensional scanning probe procedure. The tool was used to compare the coverage maps of a conventional raster scanning procedure and two modified methods: meta-raster and random meta-raster. Using XDesign, a tool for benchmarking tomographic image reconstruction, the reconstruction quality of a simulated x-ray phantom was compared for the three scanning paradigms. The results show that for steps sizes much larger than the probe size, not only does conventional raster scan have blind spots on its coverage map which are never probed, but increasing the number of viewing angles does not improve the reconstruction quality. However, for the proposed meta-raster scanning procedure, increasing the number of viewing angles always increases the coverage uniformity and increases the reconstruction quality.

6.1 Introduction

X-ray microscopy techniques based on scanning a sample with a finite extent beam have been used extensively at synchrotron facilities and are becoming increasingly important in a growing number of research applications in the biological, environmental, and materials sciences. For example, X-ray fluorescence (XRF) microscopy can provide mappings of transition elements such as iron, copper, zinc, or other trace elements in specimens at high resolution: ranging from few microns down to tens of nanometers (de Jonge and Vogt 2010; Suhonen et al. 2012; Chen et al. 2014). Another scanning-based technique, X-ray ptychography, can provide the detailed morphology of specimens at diffraction-limited resolution (Dierolf et al. 2010). Scanning-probe systems that can simultaneously acquire fluorescence and diffraction signals have also been used for matching the elemental specificity with the underlying materials structure (Vine et al. 2012; Deng et al. 2015; Jones et al. 2016).

Despite their differences in acquisition speed and image contrast mechanisms, these techniques share the same sample scanning principle; typically, the specimen is raster-scanned with a finite extent probe while collecting measurements serially at discrete steps.

The step size for the probe is usually selected to be equal to the probe size such that all structural details in the specimen can be captured and conveyed in a planar image. Extension to tomography is possible by rotating the specimen around an axis perpendicular to optical axis. However, when the step size is equal to the probe size, imaging large samples with a small probe is challenging because, within a fixed time, obtaining full detail in the planar scan dominates data collection and leaves only a limited number of projections (rotations of the object) to be collected. In other words, the ratio of lateral shifts of the probe to the number of object rotations is usually high, and although each detail is captured on individual projections, the reconstruction quality of the object suffers from undersampling of the rotational axis. The dose fractionation theorem states that the total dose required to achieve statistical significance for each voxel of a computed three-dimensional (3D) reconstruction is the same as that required to obtain a single 2D image of that isolated voxel with the same level of statistical significance (Hegerl and Hoppe 1976). However, if the ratio of object rotations to lateral shifts of the probe is increased by adding gaps between probe positions, it is not clear whether all voxels of the sample would be recorded at desired level of significance.

This publication is an investigation of the effects of scanning procedure coverage on reconstruction quality. We define the term "coverage" as the expected number of times the probe touches an arbitrary point during the procedure. E.g., if the left half of a pixel is touched once, then the pixel coverage is 0.5. If the left half of a pixel is touched twice, then the pixel

coverage is 1. We are also interested in the effects of directional coverage anisotropy, e.g. if a pixel is covered four times, but always from the same view, how does this compare with a pixel that is covered from four different views? To the authors' knowledge, the literature contains no studies related to quantifying the effects of procedure coverage on the quality of tomographic reconstruction. Probably, the most similar discussion is (Hsieh et al. 2006), which proposes the reintroduction of step and shoot acquisition for helical scanning medical CT scanners in order to synchronize exposure times with the heart beats of living people while minimizing dose and not missing slices in the longitudinal direction. Any discussion of the point spread function and resolution is tangentially related, but it is not the same. Discussion about resolution asks about the smallest resolvable feature, whereas this discussion is about the degree to which each feature is exposed to the probe.

6.2 Methods

We used XDesign v0.4 (Ching and Gürsoy 2017) to simulate data acquisition of artificial 2D phantoms and calculate scanning procedure coverage. The procedure coverage is defined as the expected number of times the probe passes through an arbitrary voxel in the object during the scanning procedure. Two new raster-scanning procedures were proposed and compared with the conventional raster-scanning procedure for different step sizes, and numbers of projection angles. The data was reconstructed using simultaneous iterative reconstruction method (SIRT) as implemented in TomoPy v1.0 (Gürsoy et al. 2014; Pelt et al. 2016). Finally, the reconstructed data was graded using the multi-scale structural similarity index (MS-SSIM) (Wang, Simoncelli, and Bovik 2003), implemented in XDesign.

6.2.1 Validating the coverage function

In order to efficiently approximate and compute the intersection of the probe and each pixel on the coverage map, we used an approximation

commonly used for back-projection reconstruction methods (Kak and Slaney 2001). This approximation of intersection area between the probe and each pixel uses a sum of n Riemann rectangles as illustrated in Figure 6.1. However, since our coverage function in not exact, we needed to calibrate the parameters of the function and estimate the approximation error.

The uniformly covered area of a conventional raster scanning procedure is a circle in the center of the field of view; this region of the field of view has a constant coverage equal to the number of projection angles when the step size equals the probe size. We divided the largest inscribed square of this circle into a 23×23 grid, which provides 529 pixels for calculating statistics.

Using 127 projection angles around 360°, we characterized the accuracy (mean error) and precision (standard deviation of error) for our coverage approximation function for R_p and B_p, the ratio of the Riemann rectangle width to the pixel size, and the ratio of the probe size to the pixel size, respectively. The results in Figure 6.1 show that the approximation is insensitive to the probe size, and if the Riemann rectangles are less than 1/16 of the pixel size, then the expected error drops below 0.01%. Therefore, we used Riemann rectangles of size 1/16 of the pixel size for calculating the coverage maps and performing the analysis through the rest of the paper.

6.2.2 Three rastering procedures

In the conventional raster scan, the translation step size is a full probe width such that there is no overlap and no space between probes. Then the specimen or probe rotates to a different view and repeats the raster. This procedure uniformly samples a circular field of view where the measurements from all viewing angles overlap.

For this study, we were interested in the effects of choosing a step size larger than the probe size (for the purpose of scanning faster or reducing radiation dose). This larger step size creates a gap in the translation space and

destroys the measurement uniformity of the circular field of view, so we investigated two modified rastering procedures to combat the effects of this gap. The first is called meta-raster; in this paradigm, after each rotation, the starting position of the first scan is bumped by a preselected width. This scanning paradigm was recently proposed as a way to reduce scanning times for X-ray fluorescence tomography (de Jonge et al. 2017) and as a way to alleviate the overlapping probe constraints in 3D ptychography (Gürsoy 2017). The second, random meta-raster, is the same except the starting offsets of each raster are randomly ordered. The layout of each of these scanning procedures in the angle-raster space is shown in Figure 6.2.

6.2.3 Coverage maps

First, we calculated probe coverage maps to compare which pixels each paradigm favors as data collection becomes sparser (Figure 6.3). For each procedure, the probe took views of a circular region of diameter 1cm from 101 angles around $360°$. The probe size and pixel size were $1/256$cm while the step size varied from twice the probe size to 16 times the probe size. The coverage maps only show the 0.25cm^2 area in the center of the field of view.

Next, we created a series of maps (Figure 6.4) to show how many angles are needed to regain uniform coverage for procedures with a gap between probes. Again, the field of view is limited to the center most 0.25cm^2. The step size was 8 times the probe size, and the probe size was $1/256$cm. The number of rotations ranged from 11 to 1009. We chose prime numbers of rotation angles to avoid redundant probe trajectories. We also used elliptical tensor glyphs (Schultz and Kindlmann 2010) to visualize the directional anisotropy of each scanning paradigm (Figure 6.5). Each glyph represents from which directions the given pixel has been probed. If the glyph is very round, then it has been equally probed from many directions. If the glyph is very anisotropic, then it has been probed only from one direction.

Finally, we simulated the data acquisition of a phantom for each of the three paradigms for step sizes 2 through 16 and numbers of rotation angles 11 through

1009. The pixel size was 1/256cm. The phantom was reconstructed with SIRT using 50 iterations, and the quality of the reconstructions was measured with the MS-SSIM index at 6 levels. The mean SSIM index for each reconstruction at each combination of step size and rotation angles was combined into a contour plot (Figure 6.6) to show how each parameter affected the reconstruction quality.

6.3 Results

As step-to-probe-size increases, the quality drops for all three procedures (Figure 6.7). However, meta and random meta-raster paradigms provide more uniform coverage than the conventional raster scan (Figure 6.3), so for them, the quality loss can be compensated by increasing the number of rotations (Figure 6.8). For conventional raster the quality does not improve (Figure 6.6) by increasing the number of projection angles.

The conventional raster scan leaves a hole in the middle of the field of view and unsampled periodic concentric rings around this hole; anything inside this hole is never probed. In contrast, meta-raster and random meta-raster provide, at higher numbers of angles, provide a region of near uniform coverage. For meta-raster, this region spreads out from the center of the field of view, and for random meta, coverage uniformity increases slowly everywhere at the same time (Figure 6.4). At more than 100 angles, meta and random perform better than conventional raster at all combinations and especially at large step sizes (Figure 6.6) with meta-raster being marginally better.

Notably, for sparse probing, the regions of high coverage in the conventional raster scan are biased towards tangential scanning directions,

whereas for meta-raster, the regions of high coverage are more directionally isotropic (Figure 6.5).

The coverage standard deviation and MS-SSIM index of the simulated reconstructions appear to be correlated. This implies the standard deviation of the coverage could be can be used directly to assess any acquisition protocol instead of performing a complete reconstruction quality analysis.

6.4 Conclusions

Meta-raster outperforms both conventional raster scan and random meta-raster in reconstruction quality tests for large step sizes and especially when many projection angles are used. However, even without analyzing reconstruction quality, we could have predicted that meta-raster would perform better by looking at the coverage maps of each of the three scanning procedures. The coverage of meta-raster is the most uniform, and it does not have any blind spots.

The relative importance of the quantity of projection angles for the meta-raster procedure is also fortuitous because continuous stage rotation is very fast compared to the motion of a sliding raster. In fact, the meta-raster procedure is the only one of the three proposed methods which may be collected with a continuous motion from both rotation stage and sliding stage.

6.5 Figures
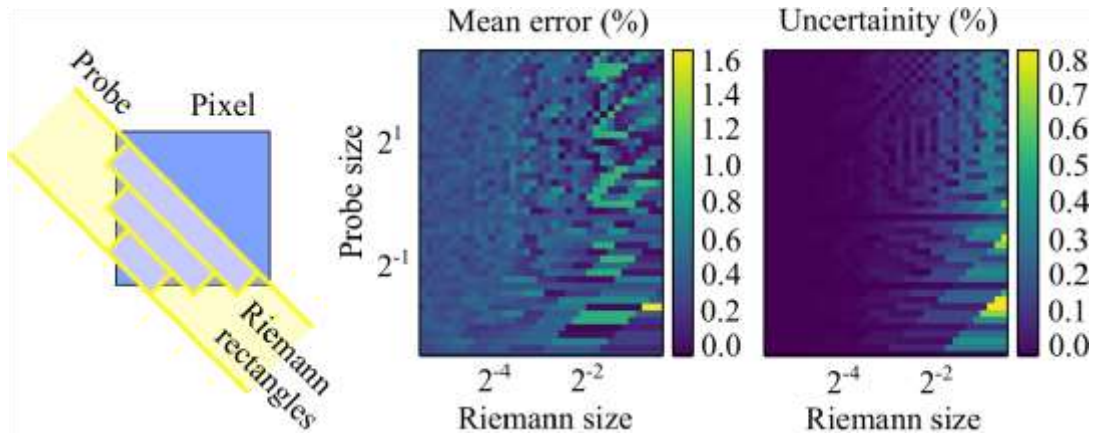
Figure 6.1 An illustration of probe approximation using Riemann rectangles (left). Percentage absolute mean error and uncertainty of coverage approximation for 127 projection angles (right).
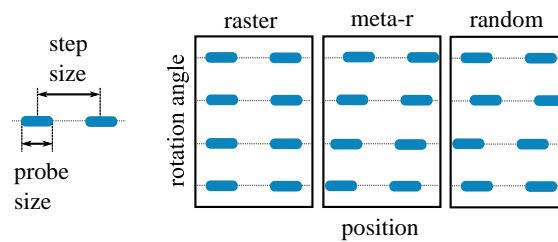
Figure 6.2 Comparison of spatial sampling for three scanning procedures: raster, meta-raster, and random.
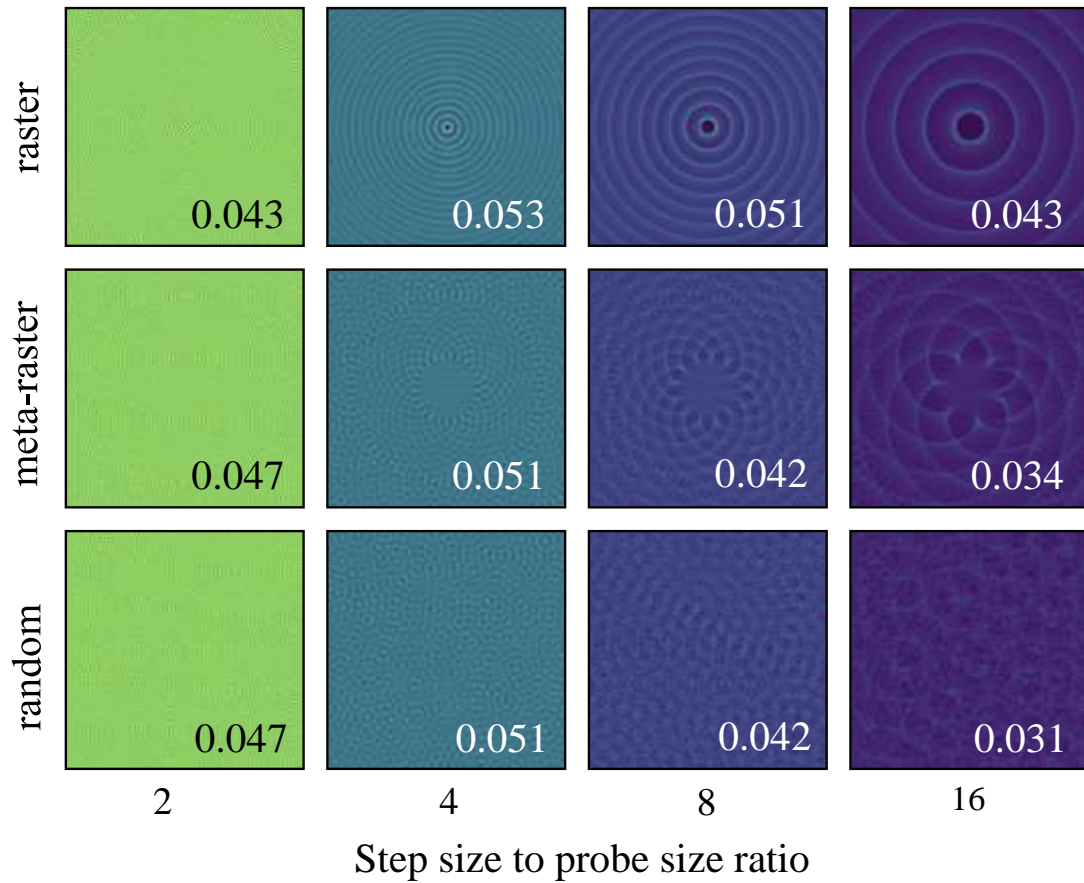
Figure 6.3 Procedure coverage for 101 projection angles and different step-to-probe-sizes. Each coverage map here is normalized to the most covered pixel of *all* maps. One standard deviation of coverage is shown in the lower corner of each panel.
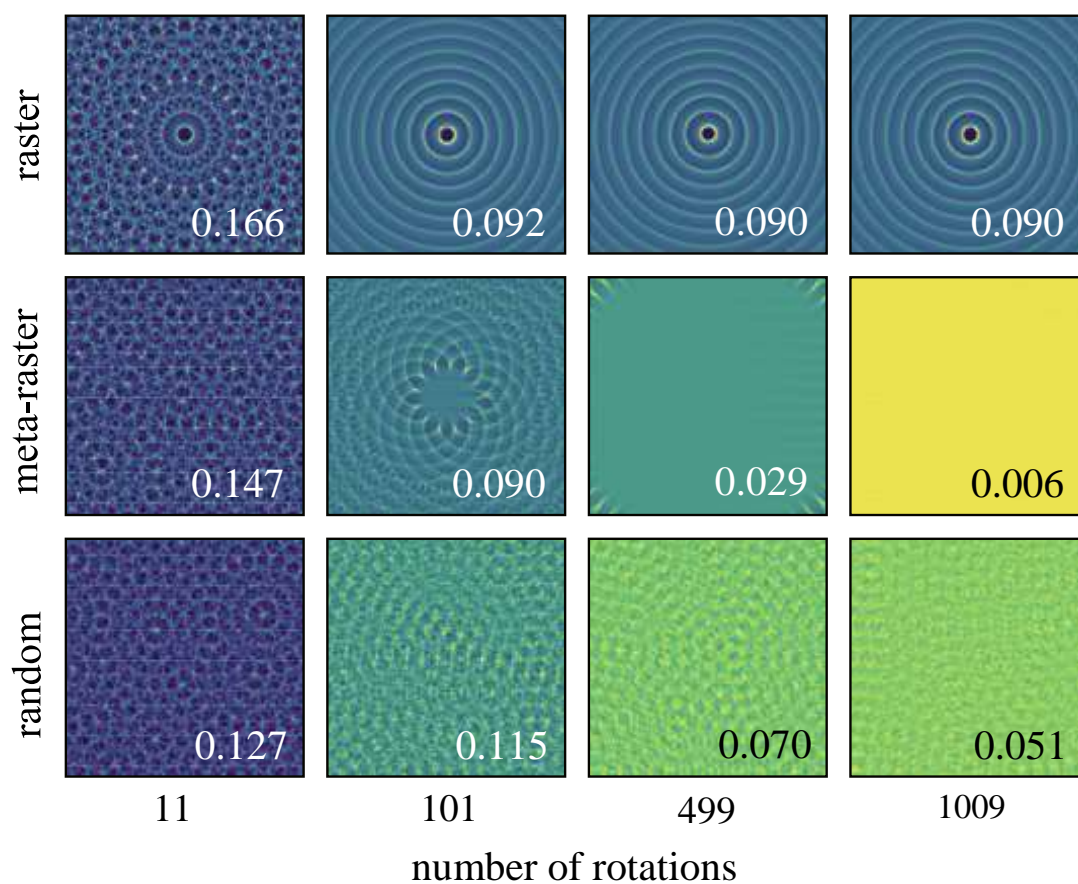
Figure 6.4 Procedure coverage for step-to-probe-size 8 and different numbers of projection angles. Each map is normalized to its *own* maximum coverage value. One standard deviation of coverage is shown in the lower corner of each panel.
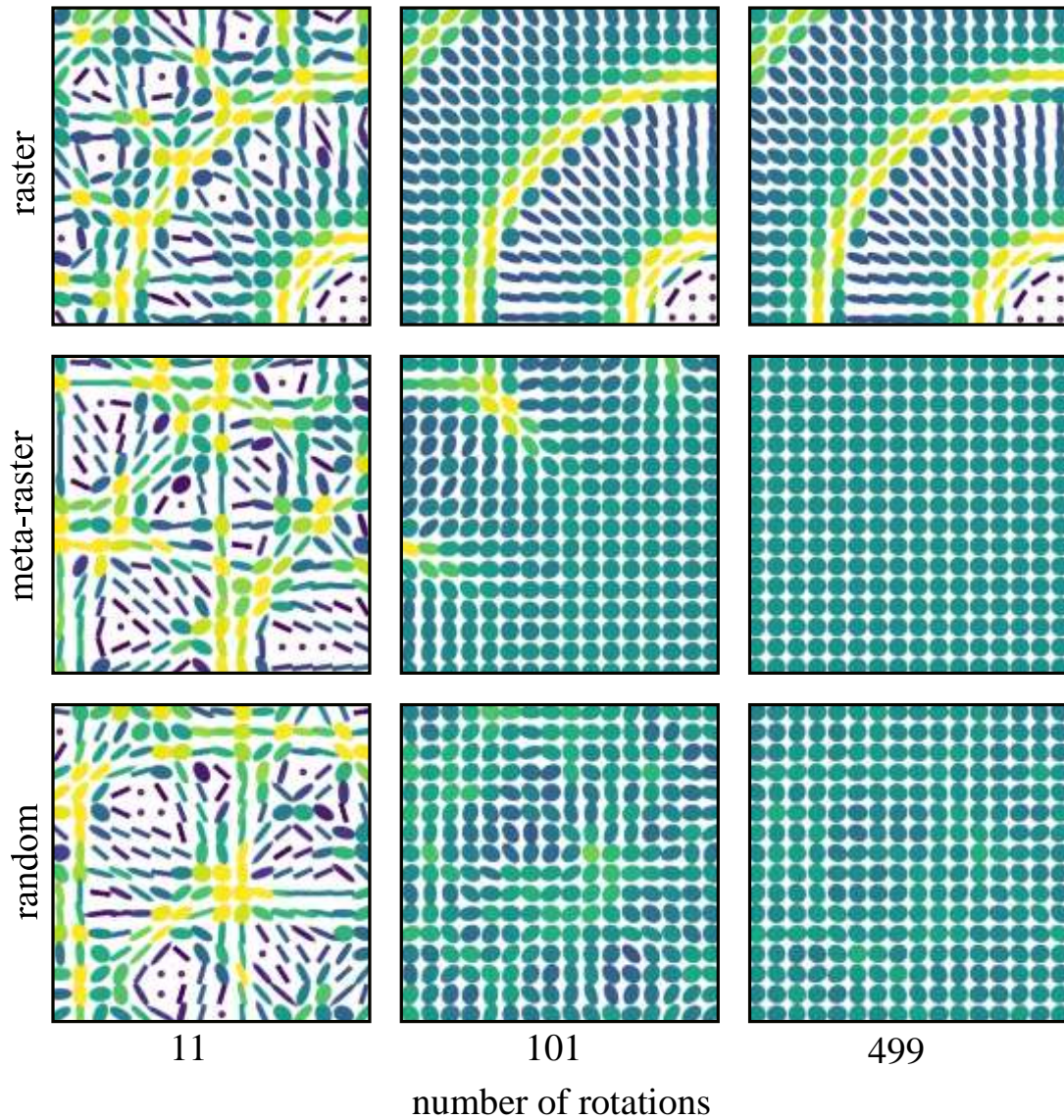
Figure 6.5 Coverage anisotropy comparison between three proposed scanning paradigms. The shape of the glyph shows the coverage anisotropy, the color shows the coverage. The same parameters are used for Figure 6.4 except the field of view here is reduced to $\frac{1}{61}$ of the former. Maps of the same number of projection angles are normalized to the same values.
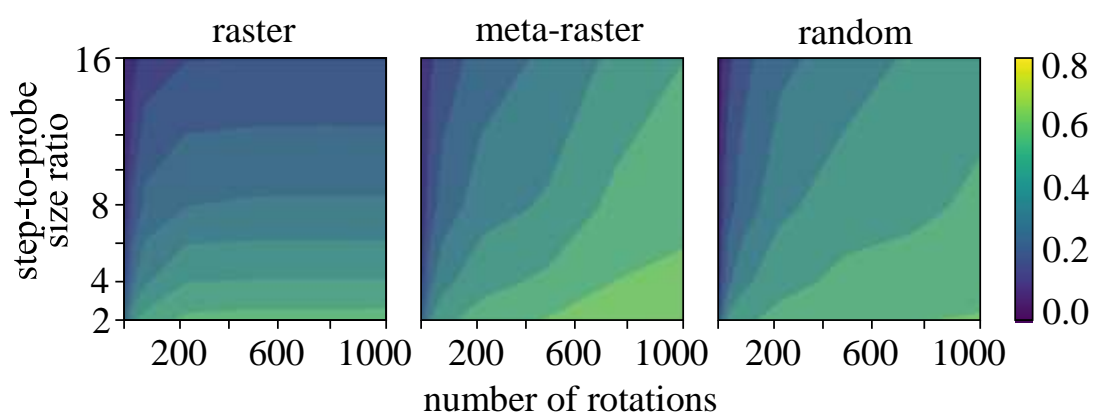
Figure 6.6 MS-SSIM index for tomographic reconstructions as a function of step-to-probe size ratio and number of rotations for each acquisition procedure.
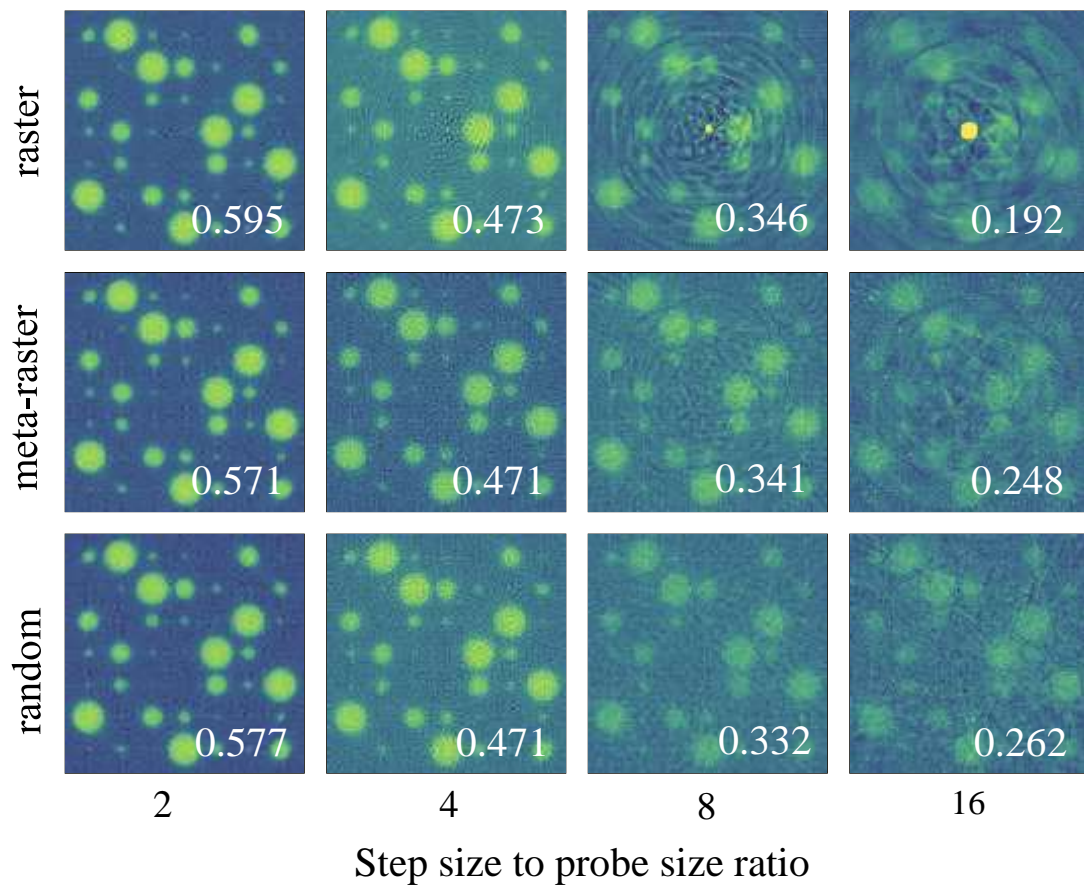
Figure 6.7 Reconstructions of DogaCircles using the acquisition procedures in Figure 6.3. MSSSIM index shown in the lower right of each panel.
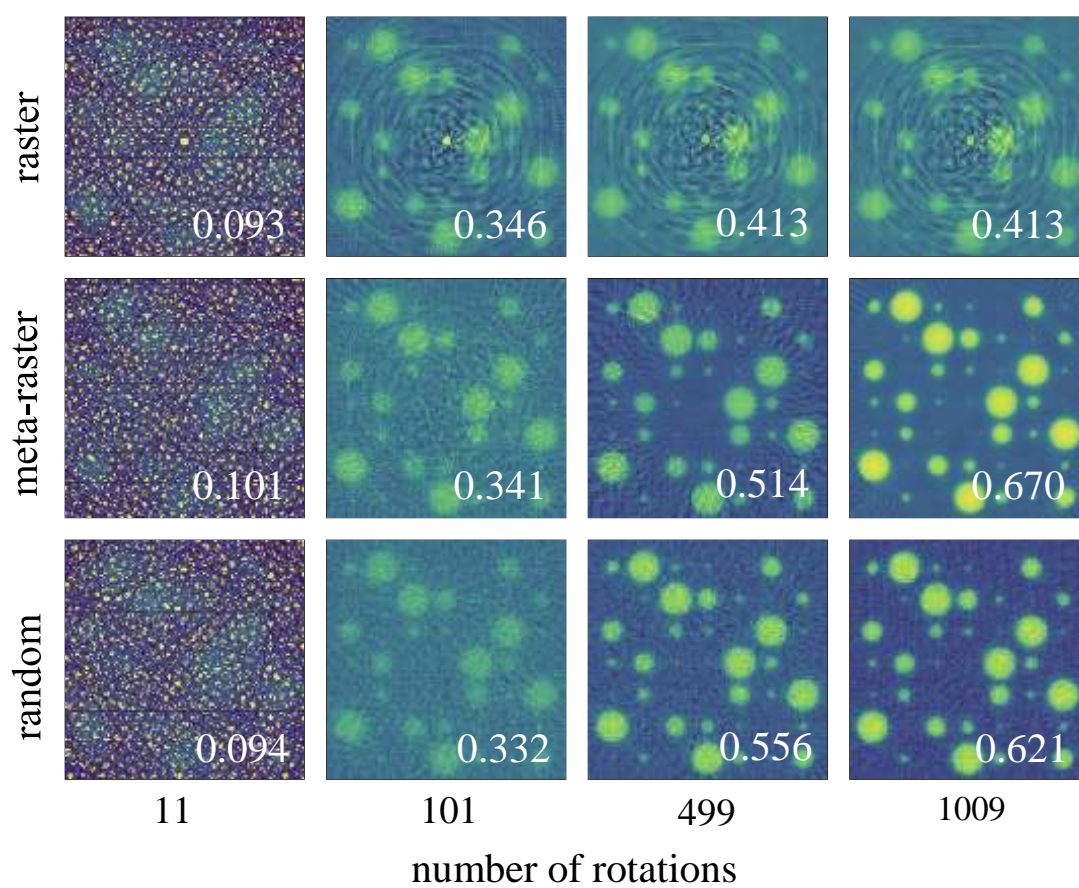
Figure 6.8 Reconstructions of simulated x-ray phantom using the acquisition procedures in Figure 6.4. MS-SSIM index shown in the lower right of each panel.

7 GENERAL CONCLUSIONS

7.1 Measurement uncertainty of digital volume correlation for micro x-ray computed tomography of wood adhesive bonds

Figure 3.2b shows the strain measurement uncertainty as a function of square correlation window size and measurement direction. This data was calculated by correlating two clear wood volumes of the same undeformed softwood specimen.

Two key observations of the measurement uncertainty are that first, the measurement uncertainty was found to be orthotropic because the natural wood texture is orthotropic and second, the measurement uncertainty was found to be inconsistent across the specimen. These obstacles might be mitigated by employing correlation windows whose shape adapts to the anisotropy of the texture to both decrease measurement anisotropy and improve consistency across a specimen as the texture changes in earlywood, latewood, bondline, and interphase regions.

Sources of measurement uncertainty for digital volume correlation have not been studied extensively, so there may be ways to generally decrease measurement uncertainty during scanning by reducing motion or improving reconstruction methods. Simulation of XCT experiments could provide estimates of the contributions of each sources of error to the total error and provide a way to compare different data collection and reconstruction methods with the aim of reducing DVC measurement uncertainty. Preliminary simulation results suggest that iterative methods, such as SIRT and MLEM, may be quantitatively better reconstruction methods; however, the trade-offs of longer reconstruction time versus any actual impact on DVC measurement uncertainty are not yet quantified. Ultimately, even with reductions in measurement uncertainty, the spatial resolution of the measurements is still limited by the

texture of the wood which is larger in scale (20 μm) than the desired spatial resolution (1 μm).

7.2 Best data acquisition practices for x-ray computed tomography of wood adhesive bonds which is to be used for digital volume correlation

Several sources of error for characterizing wood adhesive bonds were identified in this work.

First, specimens should have been more thoroughly controlled. The quality of studied specimens may be improved by meticulously screening specimens to ensure that edges are cut parallel to the bond and, notches sever the bond plane. Specimens may be protected from contamination by wrapping them in tape before they are mounted. Final screening may take place at the beamline by looking at specimens with the live x-rays projections before scanning them.

Second, specimens could have been better positioned in the field of view. On some specimens, the field of view did not contain as much of the region of interest as possible; sometimes this is due to specimen movement from its initial position, other times it was poor placement by the operator. Painting the outside of the specimen with references marks (e.g. dots of metallic paint) could be helpful.

Third, collecting a low-resolution wide-view scan of each specimen before focusing on a smaller region of interest or collecting a lower resolution scan with an overall larger field of view could be helpful for generating boundary conditions in a finite element model of the specimen. Models starting with XCT of the entire specimen can implement accurate geometry of the specimen and account for differences in the behavior between earlywood and latewood. Reducing the scan resolution to increase the field of view by 2-3 times would

likely not affect the DVC results because the features being correlated are very large compared to the 1.3 micron voxels size of the present study.

Fourth, the phase contrast effect from additional specimen to detector distance did not make up for the loss in attenuation contrast which results from the wood cell and adhesive becoming more transparent to x-rays at higher beam energies.

Fifth, specimens in changing relative humidity conditions should be paired with similar specimens to collect average moisture content.

7.3 The effect of macro adhesive penetration on the load transfer performance of wood adhesive bonds

The effect of adhesive penetration on load transfer across the bonding interface is inconclusive. It is unclear if the results were inconclusive due to lack of a relationship between adhesive penetration and stress transfer, or if the natural variability of wood texture, less than optimum specimen preparation, and small number of specimens obscured a relationship.

Also, the proposed metrics in Section 3.2.5 for measuring stress transfer are questionable. The appendix contains a preliminary a simulative study comparing different methods of quantifying the load transfer from only strain observations. However, it may be that this approach of trying to parameterize bond quality as a single value is flawed, and multi-parameter mechanical models, such as MPM, will provide better insights into the relationship between adhesive flow penetration and bond quality.

7.4 The effect of macro adhesive penetration on moisture swelling of wood adhesive bonds

The effect of adhesive bond lines on the local moisture-induced swelling of latewood loblolly pine was observed. Specifically, the Br-doped PF-based adhesives used to bond the specimens suppressed radial swelling near the

bond line and tangentially away from the bond line in ray cells filled with adhesive. Regardless of adhesive content, large fusiform ray cells were observed to have a tangential suppression effect on the surrounding wood. The tomography and strain fields suggest that the reason that radial suppression of swelling was limited was due to bubbles and swelling induced breaks of the adhesive, which prevented the adhesive from suppressing swelling away from the bonded interface.

8 BIBLIOGRAPHY

Aarle, Wim van, Willem Jan Palenstijn, Jan De Beenhouwer, Thomas Altantzis, Sara Bals, Kees Joost Batenburg, and Jan Sijbers. 2015. "The ASTRA Toolbox: A Platform for Advanced Algorithm Development in Electron Tomography." *Ultramicroscopy* 157:35–47. https://doi.org/10.1016/j.ultramic.2015.05.002.

Arias-Castro, Ery, and David L. Donoho. 2009. "Does Median Filtering Truly Preserve Edges Better than Linear Filtering?" *Annals of Statistics* 37 (3):1172–1206. https://doi.org/10.1214/08-AOS604.

Baensch, Franziska. 2015. "Damage Evolution in Wood and Layered Wood Composites Monitored in Situ Bay Acoustic Emission, Digital Image Correlation and Synchrotron Based Tomographic Microscopy." ETH Zurich. https://doi.org/10.3929/ethz-a-010411928.

Bar-Kochba, E., J. Toyjanova, E. Andrews, K. S. Kim, and Christian Franck. 2015. "A Fast Iterative Digital Volume Correlation Algorithm for Large Deformations." *Experimental Mechanics* 55 (1). Springer US:261–74. https://doi.org/10.1007/s11340-014-9874-2.

Bay, Brian K. 2008. "Methods and Applications of Digital Volume Correlation." *The Journal of Strain Analysis for Engineering Design* 43 (8):745–60. https://doi.org/10.1243/03093247JSA436.

Bay, Brian K., T. S. Smith, D. P. Fyhrie, and M. Saad. 1999. "Digital Volume Correlation: Three-Dimensional Strain Mapping Using X-Ray Tomography." *Experimental Mechanics* 39 (3). Kluwer Academic Publishers:217–26. https://doi.org/10.1007/BF02323555.

Bergamaschi, Antoine, Kadda Medjoubi, Cédric Messaoudi, Sergio Marco, and Andrea Somogyi. 2016. "MMX-I: Data-Processing Software for Multimodal X-Ray Imaging and Tomography." *Journal of Synchrotron Radiation* 23 (3). International Union of Crystallography:783–94.

https://doi.org/10.1107/S1600577516003052.

Berger, Martin J., and J. H. Hubbell. 1987. "XCOM: Photon Cross Sections on a Personal Computer."

Boas, F. Edward, and Dominik Fleischmann. 2012. "CT Artifacts: Causes and Reduction Techniques." *Imaging in Medicine* 4 (2):229–40. https://doi.org/10.2217/iim.12.13.

Bornert, M., F. Brémand, Pascal Doumalin, Jean Christophe Dupré, M. Fazzini, M. Grédiac, F. Hild, et al. 2009. "Assessment of Digital Image Correlation Measurement Errors: Methodology and Results." *Experimental Mechanics* 49 (3). Springer US:353–70. https://doi.org/10.1007/s11340-008-9204-7.

Boutelje, J. B. 1962. "The Relationship of Structure to Transverse Anisotropy in Wood with Reference to Shrinkage and Elasticity." *Holzforschung* 16 (2). Walter de Gruyter, Berlin / New York:33–46. https://doi.org/10.1515/hfsg.1962.16.2.33.

Brandt, Björn, Cordt Zollfrank, Oliver Franke, Jörg Fromm, Mathias Göken, and Karsten Durst. 2010. "Micromechanics and Ultrastructure of Pyrolysed Softwood Cell Walls." *Acta Biomaterialia* 6 (11). Elsevier:4345–51. https://doi.org/10.1016/j.actbio.2010.05.026.

Brault, R., A. Germaneau, Jean Christophe Dupré, Pascal Doumalin, S. Mistou, and M. Fazzini. 2013. "In-Situ Analysis of Laminated Composite Materials by X-Ray Micro-Computed Tomography and Digital Volume Correlation." *Experimental Mechanics* 53 (7). Springer US:1143–51. https://doi.org/10.1007/s11340-013-9730-9.

Bucur, Voichita. 2011. *Delamination in Wood, Wood Products and Wood-Based Composites. Delamination in Wood, Wood Products and Wood-Based Composites.* https://doi.org/10.1007/978-90-481-9550-3.

Chen, Si, Junjing Deng, Y. Yuan, C. Flachenecker, R. Mak, B. Hornberger, Qiaoling Jin, et al. 2014. "The Bionanoprobe: Hard X-Ray Fluorescence

Nanoprobe with Cryogenic Capabilities." *Journal of Synchrotron Radiation* 21 (1). International Union of Crystallography:66–75. https://doi.org/10.1107/S1600577513029676.

Ching, Daniel J., and Doǧa Gürsoy. 2017. "XDesign: An Open-Source Software Package for Designing X-Ray Imaging Phantoms and Experiments." *Journal of Synchrotron Radiation* 24 (2):537–44. https://doi.org/10.1107/S1600577517001928.

Deng, Junjing, David J Vine, Si Chen, Youssef S.G. Nashed, Qiaoling Jin, Nicholas W. Phillips, Tom Peterka, Rob Ross, Stefan Vogt, and Chris J Jacobsen. 2015. "Simultaneous Cryo X-Ray Ptychographic and Fluorescence Microscopy of Green Algae." *Proceedings of the National Academy of Sciences* 112 (8). National Academy of Sciences:2314–19. https://doi.org/10.1073/pnas.1413003112.

Derome, Dominique, Michele Griffa, Matthias Koebel, and Jan Carmeliet. 2011. "Hysteretic Swelling of Wood at Cellular Scale Probed by Phase-Contrast X-Ray Tomography." *Journal of Structural Biology* 173 (1):180–90. https://doi.org/10.1016/j.jsb.2010.08.011.

Dierolf, Martin, Andreas Menzel, Pierre Thibault, Philipp Schneider, Cameron M. Kewish, Roger Wepf, Oliver Bunk, and Franz Pfeiffer. 2010. "Ptychographic X-Ray Computed Tomography at the Nanoscale." *Nature* 467 (7314). Nature Publishing Group:436–39. https://doi.org/10.1038/nature09419.

Dufresne, Alain. 2013. "Nanocellulose: A New Ageless Bionanomaterial." *Materials Today* 16 (6):220–27. https://doi.org/10.1016/j.mattod.2013.06.004.

EFunda. 2018. "Properties of Phenolic {unfilled, Casting Resins}." 2018. http://www.efunda.com/materials/polymers/properties/polymer_datasheet .cfm?MajorID=phenolic&MinorID=10.

Estrada, Jonathan B., and Christian Franck. 2015. "Intuitive Interface for the

Quantitative Evaluation of Speckle Patterns for Use in Digital Image and Volume Correlation Techniques." *Journal of Applied Mechanics* 82 (9). American Society of Mechanical Engineers:95001. https://doi.org/10.1115/1.4030821.

Faul, Franz, Edgar Erdfelder, Albert-Georg Lang, and Axel Buchner. 2007. "G*Power 3: A Flexible Statistical Power Analysis Program for the Social, Behavioral, and Biomedical Sciences." *Behavior Research Methods* 39 (2):175–91. https://doi.org/10.3758/BF03193146.

Filippidis, Ioannis, Sumanth Dathathri, Scott C Livingston, Necmiye Ozay, and Richard M Murray. 2016. "Control Design for Hybrid Systems with TuLiP: The Temporal Logic Planning Toolbox." In *Control Applications (CCA), 2016 IEEE Conference on*, 1030–41.

Forsberg, F., M. Sjödahl, R. Mooser, E. Hack, and P. Wyss. 2010. "Full Three-Dimensional Strain Measurements on Wood Exposed to Three-Point Bending: Analysis by Use of Digital Volume Correlation Applied to Synchrotron Radiation Micro-Computed Tomography Image Data." *Strain* 46 (1). Blackwell Publishing Ltd:47–60. https://doi.org/10.1111/j.1475-1305.2009.00687.x.

Friedman, Saul N., George S.K. Fung, Jeffrey H. Siewerdsen, and Benjamin M.W. Tsui. 2013. "A Simple Approach to Measure Computed Tomography (CT) Modulation Transfer Function (MTF) and Noise-Power Spectrum (NPS) Using the American College of Radiology (ACR) Accreditation Phantom." *Medical Physics* 40 (5). https://doi.org/10.1118/1.4800795.

Frihart, Charles R., and James M. Wescott. 2008. "Why Do Some Wood-Adhesive Bonds Respond Poorly to Accelerated Moisture-Resistant Tests?" *9th Pacific Rim Bio-Based Composites Symposium*, 51–58. http://www.treesearch.fs.fed.us/pubs/33198.

Gates, M., J. Lambros, and M. T. Heath. 2011. "Towards High Performance

Digital Volume Correlation." *Experimental Mechanics* 51 (4):491–507. https://doi.org/10.1007/s11340-010-9445-0.

Gereke, Thomas, Stefan Hering, and Peter Niemz. 2016. "Finite Element Analysis of Wood Adhesive Joints." *Pro Ligno* 12 (1):3–14. http://www.proligno.ro/en/articles/2016/201601.htm.

Germaneau, Arnaud, Pascal Doumalin, and Jean Christophe Dupré. 2008. "Comparison between X-Ray Micro-Computed Tomography and Optical Scanning Tomography for Full 3D Strain Measurement by Digital Volume Correlation." *NDT and E International* 41 (6):407–15. https://doi.org/10.1016/j.ndteint.2008.04.001.

Gilbert, Peter. 1972. "Iterative Methods for the Three-Dimensional Reconstruction of an Object from Projections." *Journal of Theoretical Biology* 36 (1):105–17. https://doi.org/10.1016/0022-5193(72)90180-4.

Gillard, F., R. Boardman, M. Mavrogordato, D. Hollis, I. Sinclair, F. Pierron, and M. Browne. 2014. "The Application of Digital Volume Correlation (DVC) to Study the Microstructural Behaviour of Trabecular Bone during Compression." *Journal of the Mechanical Behavior of Biomedical Materials* 29:480–99. https://doi.org/10.1016/j.jmbbm.2013.09.014.

Gindl-Altmutter, W., Ulrich Müller, and Johannes Konnerth. 2012. "The Significance of Lap-Shear Testing of Wood Adhesive Bonds by Means of Volkersen's Shear Lag Model." *European Journal of Wood and Wood Products* 70 (6). Springer-Verlag:903–5. https://doi.org/10.1007/s00107-012-0621-z.

Glass, Samuel V., and Samuel L. Zelinka. 2010. "Moisture Relations and Physical Properties of Wood." *Wood Handbook - Wood as an Engineering Material*, 4.1-4.19. https://doi.org/General Technical Report FPL-GTR-190.

Gordon, Richard, Robert Bender, and Gabor T. Herman. 1970. "Algebraic Reconstruction Techniques (ART) for Three-Dimensional Electron

Microscopy and X-Ray Photography." *Journal of Theoretical Biology* 29 (3):471–81. https://doi.org/10.1016/0022-5193(70)90109-8.

Gürsoy, Doǧa. 2017. "Direct Coupling of Tomography and Ptychography." *Optics Letters* 42 (16). Optical Society of America:3169. https://doi.org/10.1364/OL.42.003169.

Gürsoy, Doǧa, Francesco De Carlo, Xianghui Xiao, and Chris J Jacobsen. 2014. "TomoPy: A Framework for the Analysis of Synchrotron Tomographic Data." *Journal of Synchrotron Radiation* 21 (5). International Union of Crystallography:1188–93. https://doi.org/10.1107/S1600577514013939.

Hashash, Youssef M A, John I-Chiang Yao, and Donald C Wotring. 2003. "Glyph and Hyperstreamline Representation of Stress and Strain Tensors and Material Constitutive Response." *International Journal for Numerical and Analytical Methods in Geomechanics* 27 (7). John Wiley & Sons, Ltd.:603–26. https://doi.org/10.1002/nag.288.

Hegerl, R., and W. Hoppe. 1976. "Influence of Electron Noise on Three-Dimensional Image Reconstruction." *Zeitschrift Für Naturforschung A* 31 (12). Verlag der Zeitschrift für Naturforschung:1717–21. https://doi.org/10.1515/zna-1976-1241.

Henke, Burton L., Eric M. Gullikson, and John C. Davis. 1993. "X-Ray Interactions: Photoabsorption, Scattering, Transmission, and Reflection at E= 50-30,000 eV, Z= 1-92." *Atomic Data and Nuclear Data Tables* 54 (2). Elsevier:181–342.

Hoadley, R Bruce. 1990. *Identifying Wood: Accurate Results with Simple Tools*. Taunton Press.

Holman, Beverley F., Vesna Cuplov, Brian F. Hutton, Ashley M. Groves, and Kris Thielemans. 2016. "The Effect of Respiratory Induced Density Variations on Non-TOF PET Quantitation in the Lung." *Physics in Medicine and Biology* 61 (8). IOP Publishing:3148.

Hsieh, Jiang, John Londt, Melissa Vass, Jay Li, Xiangyang Tang, and Darin Okerlund. 2006. "Step-and-Shoot Data Acquisition and Reconstruction for Cardiac X-Ray Computed Tomography." *Medical Physics* 33 (11). American Association of Physicists in Medicine:4236–48. https://doi.org/10.1118/1.2361078.

Hsieh, Jiang, and others. 2009. "Computed Tomography: Principles, Design, Artifacts, and Recent Advances." In .

Hunter, John D. 2007. "Matplotlib: A 2D Graphics Environment." *Computing in Science and Engineering* 9 (3):99–104. https://doi.org/10.1109/MCSE.2007.55.

Jakes, Joseph E., Christopher G. Hunt, Daniel J. Yelle, Linda Lorenz, Kolby Hirth, Sophie-Charlotte Gleber, Stefan Vogt, Warren Grigsby, and Charles R. Frihart. 2015. "Synchrotron-Based X-Ray Fluorescence Microscopy in Conjunction with Nanoindentation to Study Molecular-Scale Interactions of Phenol–Formaldehyde in Wood Cell Walls." *ACS Applied Materials & Interfaces* 7 (12). American Chemical Society:6584–89. https://doi.org/10.1021/am5087598.

Jan, S., G. Santin, D. Strul, S. Staelens, K. Assié, D. Autret, S. Avner, et al. 2004. "GATE: A Simulation Toolkit for PET and SPECT." *Physics in Medicine and Biology* 49 (19). IOP Publishing:4543–61. https://doi.org/10.1088/0031-9155/49/19/007.

Jones, Michael W.M., Nicholas W. Phillips, Grant A. Van Riessen, Brian Abbey, David J. Vine, Youssef S.G. Nashed, Stephen T. Mudie, et al. 2016. "Simultaneous X-Ray Fluorescence and Scanning X-Ray Diffraction Microscopy at the Australian Synchrotron XFM Beamline." *Journal of Synchrotron Radiation* 23 (5). International Union of Crystallography:1151–57. https://doi.org/10.1107/S1600577516011917.

Jonge, Martin D. de, Andrew M. Kingston, Nader Afshar, Jan Garrevoet, Robin

Kirkham, Gary Ruben, Glenn R. Myers, et al. 2017. "Spiral Scanning X-Ray Fluorescence Computed Tomography." *Optics Express* 25 (19). Optical Society of America:23424. https://doi.org/10.1364/OE.25.023424.

Jonge, Martin D. de, and Stefan Vogt. 2010. "Hard X-Ray Fluorescence Tomography—an Emerging Tool for Structural Visualization." *Current Opinion in Structural Biology* 20 (5). Elsevier Current Trends:606–14. https://doi.org/10.1016/j.sbi.2010.09.002.

Kak, Avinash C., and Malcolm Slaney. 2001. *Principles of Computerized Tomographic Imaging*. Society for Industrial and Applied Mathematics. https://doi.org/10.1137/1.9780898719277.

Kamke, Frederick A., and Jong N. Lee. 2007. "Adhesive Penetration in Wood: A Review." *Wood and Fiber Science* 39 (2):205–20.

Kamke, Frederick A., Paige Elizabeth McKinley, Daniel J. Ching, Michaela Zauner, C. Hammerquist, and John A. Nairn. 2016. "Influence of Microstructure on Adhesive Penetration and Bond Performance." In *WCTE 2016 - World Conference on Timber Engineering*.

Kamke, Frederick A., John A. Nairn, Lech Muszyń ski, Jesse L. Paris, Matthew Schwarzkopf, and Xianghui Xiao. 2014. "Methodology for Micromechanical Analysis of Wood Adhesive Bonds Using X-Ray Computed Tomography and Numerical Modeling." *Wood and Fiber Science* 46 (1):15–28.

Ketcham, Richard A., and William D. Carlson. 2001. "Acquisition, Optimization and Interpretation of X-Ray Computed Tomographic Imagery: Applications to the Geosciences." *Computers and Geosciences* 27 (4):381–400. https://doi.org/10.1016/S0098-3004(00)00116-3.

Leclerc, H., J. N. Périé, S. Roux, and F. Hild. 2011. "Voxel-Scale Digital Volume Correlation." *Experimental Mechanics* 51 (4). Springer US:479–90. https://doi.org/10.1007/s11340-010-9407-6.

Levkowitz, Haim, and Gabor T. Herman. 1992. "Color Scales for Image Data."

IEEE Computer Graphics and Applications 12 (1):72–80.
https://doi.org/10.1109/38.135886.

Limodin, N., J. Réthoré, J. Adrien, J. Y. Buffière, F. Hild, and S. Roux. 2011.
"Analysis and Artifact Correction for Volume Correlation Measurements
Using Tomographic Images from a Laboratory X-Ray Source." *Experimental
Mechanics* 51 (6):959–70. https://doi.org/10.1007/s11340-010-9397-4.

Liu, Yijin, Florian Meirer, Phillip A. Williams, Junyue Wang, Joy C. Andrews, and
Piero Pianetta. 2012. "TXM-Wizard: A Program for Advanced Data Collection
and Evaluation in Full-Field Transmission X-Ray Microscopy." *Journal of
Synchrotron Radiation* 19 (2). International Union of Crystallography:281–
87. https://doi.org/10.1107/S0909049511049144.

Marchesini, Stefano, Hari Krishnan, Benedikt J. Daurer, David A. Shapiro, Talita
Perciano, James A. Sethian, and Filipe R. N. C. Maia. 2016. "SHARP: A
Distributed GPU-Based Ptychographic Solver." *Journal of Applied
Crystallography* 49 (4). International Union of Crystallography:1245–52.

Marone, F., and M. Stampanoni. 2012. "Regridding Reconstruction Algorithm for
Real-Time Tomographic Imaging." *Journal of Synchrotron Radiation* 19
(6):1029–37. https://doi.org/10.1107/S0909049512032864.

McKinley, Paige Elizabeth, Daniel J. Ching, Frederick A. Kamke, Michaela Zauner,
and Xianghui Xiao. 2016. "Micro X-Ray Computed Tomography of Adhesive
Bonds in Wood." *Wood and Fiber Science* 905 (2013):2–16.
https://wfs.swst.org/index.php/wfs/article/view/2291.

McKinley, Paige Elizabeth, Frederick A. Kamke, Arijit Sinha, Vincent De Andrade,
and Joseph E. Jakes. 2018. "Analysis of Adhesive Penetration into Wood
Using Nano-X-Ray Computed Tomography." *Wood and Fiber Science* 50
(1):66–76.

Münch, Beat, Pavel Trtik, Federica Marone, and Marco Stampanoni. 2009. "Stripe
and Ring Artifact Removal with Combined Wavelet-Fourier Filtering." *EMPA*

Activities, no. 2009–2010 EMPA ACTIVITIES:34–35. https://doi.org/10.1364/OE.17.008567.

Nairn, J. A. 2013. "Modeling Imperfect Interfaces in the Material Point Method Using Multimaterial Methods." *CMES - Computer Modeling in Engineering and Sciences* 92 (3):271–99.

Nairn, John A. 2014. "NairnFEA." 2014. http://osupdocs.forestry.oregonstate.edu/index.php/NairnFEA.

Narter, Matt, and Mark L. Brusseau. 2010. "Comparison of Interfacial Partitioning Tracer Test and High-Resolution Microtomography Measurements of Fluid-Fluid Interfacial Areas for an Ideal Porous Medium." *Water Resources Research* 46 (8). Wiley Online Library.

Ormarsson, Sigurdur, and Óskar V. Gíslason. 2016. "Moisture-Induced Stresses in Glulam Frames." *European Journal of Wood and Wood Products* 74 (3):307–18. https://doi.org/10.1007/s00107-016-1006-5.

Palanca, Marco, Gianluca Tozzi, Luca Cristofolini, Marco Viceconti, and Enrico Dall'Ara. 2015. "Three-Dimensional Local Measurements of Bone Strain and Displacement: Comparison of Three Digital Volume Correlation Approaches." *Journal of Biomechanical Engineering* 137 (7). American Society of Mechanical Engineers:71006. https://doi.org/10.1115/1.4030174.

Pan, Bing. 2013. "Bias Error Reduction of Digital Image Correlation Using Gaussian Pre-Filtering." *Optics and Lasers in Engineering* 51 (10):1161–67. https://doi.org/10.1016/j.optlaseng.2013.04.009.

Paris, Jesse L., Frederick A. Kamke, Reginald Mbachu, and Sara Kraushaar. 2014. "Phenol Formaldehyde Adhesives Formulated for Advanced X-Ray Imaging in Wood-Composite Bondlines." *Journal of Materials Science* 49 (2):580–91. https://doi.org/10.1007/s10853-013-7738-2.

Paris, Jesse L., Frederick A. Kamke, and Xianghui Xiao. 2015. "X-Ray Computed

Tomography of Wood-Adhesive Bondlines: Attenuation and Phase-Contrast Effects." *Wood Science and Technology* 49 (6). Springer Berlin Heidelberg:1185–1208. https://doi.org/10.1007/s00226-015-0750-8.

Patera, Alessandra, Jan van Den Bulcke, Matthieu N. Boone, Dominique Derome, and Jan Carmeliet. 2017. "Swelling Interactions of Earlywood and Latewood across a Growth Ring: Global and Local Deformations." *Wood Science and Technology*, September. Springer Berlin Heidelberg, 1–24. https://doi.org/10.1007/s00226-017-0960-3.

Patera, Alessandra, Dominique Derome, Michele Griffa, and Jan Carmeliet. 2013. "Hysteresis in Swelling and in Sorption of Wood Tissue." *Journal of Structural Biology* 182 (3):226–34. https://doi.org/10.1016/j.jsb.2013.03.003.

Patterson, Brian M., Nikolaus L. Cordes, Kevin Henderson, Jason J. Williams, Tyler Stannard, Sudhanshu S. Singh, Angel Rodriguez Ovejero, Xianghui Xiao, Mathew Robinson, and Nikhilesh Chawla. 2016. "In Situ X-Ray Synchrotron Tomographic Imaging during the Compression of Hyper-Elastic Polymeric Materials." *Journal of Materials Science* 51 (1):171–87. https://doi.org/10.1007/s10853-015-9355-8.

Pelt, Daniël M., Doğ a Gürsoy, Willem Jan Palenstijn, Jan Sijbers, Francesco De Carlo, and Kees Joost Batenburg. 2016. "Integration of TomoPy and the ASTRA Toolbox for Advanced Processing and Reconstruction of Tomographic Synchrotron Data." *Journal of Synchrotron Radiation* 23 (3). International Union of Crystallography:842–49. https://doi.org/10.1107/S1600577516005658.

"Phenol Formaldehyde (PF, Phenolic)." n.d. Accessed October 21, 2016. http://www.makeitfrom.com/material-properties/Phenol-Formaldehyde-PF-Phenolic.

Rafsanjani, Ahmad, Dominique Derome, and Jan Carmeliet. 2012. "The Role of

Geometrical Disorder on Swelling Anisotropy of Cellular Solids." *Mechanics of Materials* 55:49–59. https://doi.org/10.1016/j.mechmat.2012.08.002.

Rafsanjani, Ahmad, Dominique Derome, Robert A. Guyer, and Jan Carmeliet. 2013. "Swelling of Cellular Solids: From Conventional to Re-Entrant Honeycombs." *Applied Physics Letters* 102 (21):211907–101. https://doi.org/10.1063/1.4807844.

Rafsanjani, Ahmad, Michael Stiefel, Konstantins Jefimovs, Rajmund Mokso, Dominique Derome, and Jan Carmeliet. 2014. "Hygroscopic Swelling and Shrinkage of Latewood Cell Wall Micropillars Reveal Ultrastructural Anisotropy." *Journal of The Royal Society Interface* 11 (95):20140126–20140126. https://doi.org/10.1098/rsif.2014.0126.

Reu, Phillip L. 2013. "Uncertainty Quantification for 3D Digital Image Correlation." In *Imaging Methods for Novel Materials and Challenging Applications, Volume 3: Proceedings of the 2012 Annual Conference on Experimental and Applied Mechanics*, 3:311–17. https://doi.org/10.1007/978-1-4614-4235-6_43.

Reu, Phillip L., Michael Sutton, Yanqing Wang, and Timothy J. Miller. 2009. "Uncertainty Quantification for Digital Image Correlation." In *SEM Annual Conference*, 311–17. Albuquerque, New Mexico, USA.

Roberts, Bryant C., Egon Perilli, and Karen J. Reynolds. 2014. "Application of the Digital Volume Correlation Technique for the Measurement of Displacement and Strain Fields in Bone : A Literature Review." *Journal of Biomechanics* 47 (5). Elsevier:923–34. https://doi.org/10.1016/j.jbiomech.2014.01.001.

Ropinski, Timo, Steffen Oeltze, and Bernhard Preim. 2011. "Survey of Glyph-Based Visualization Techniques for Spatial Multivariate Medical Data." *Computers and Graphics (Pergamon)* 35 (2):392–401. https://doi.org/10.1016/j.cag.2011.01.011.

Rufat, Dzhelil. 2013. "Python Triangle." http://dzhelil.info/triangle/.

Sasov, Alexander, Xuan Liu, and Pl Salmon. 2008. "Compensation of Mechanical Inaccuracies in Micro-CT and Nano-CT." *Proceedings of SPIE* 7078:70781C–70781C–9. https://doi.org/10.1117/12.793212.

Sause, Markus G. R. 2016. *In Situ Monitoring of Fiber-Reinforced Composites: Theory, Basic Concepts, Methods, and Applications*. Vol. 242. Springer. https://doi.org/10.1007/978-3-319-30954-5.

Schlüter, Steffen, Adrian Sheppard, Kendra Brown, and Dorthe Wildenschild. 2014. "Image Processing of Multiphase Images Obtained via X-Ray Microtomography: A Review." *Water Resources Research* 50 (4). Wiley Online Library:3615–39. https://doi.org/10.1002/2014WR015256.

Schulgasser, K., and A. Witztum. 2015. "How the Relationship between Density and Shrinkage of Wood Depends on Its Microstructure." *Wood Science and Technology* 49 (2):389–401. https://doi.org/10.1007/s00226-015-0699-7.

Schultz, Thomas, and Gordon L. Kindlmann. 2010. "Superquadric Glyphs for Symmetric Second-Order Tensors." *IEEE Transactions on Visualization and Computer Graphics* 16 (6):1595–1604. https://doi.org/10.1109/TVCG.2010.199.

Schwarzkopf, M., Lech Muszyński, Jesse L. Paris, John A. Nairn, and Frederick A. Kamke. 2016. "Integrating Optical Measurement and Modelling for Quantitative Analysis of the Micromechanical Load Transfer in the Wood-Adhesive Bond Interphase." *International Wood Products Journal* 7 (4). Taylor & Francis:231–34. https://doi.org/10.1080/20426445.2016.1204515.

Schwarzkopf, Matthew, and Lech Muszyński. 2015. "Stereomicroscopic Optical Method for the Assessment of Load Transfer Patterns across the Wood-Adhesive Bond Interphase." *Holzforschung* 69 (5):653–60. https://doi.org/10.1515/hf-2014-0098.

Sernek, M., J. Resnik, and Frederick A. Kamke. 1999. "Penetration of Liquid

Urea-Formaldehyde Adhesive into Beech Wood." *Wood and Fiber Science* 31 (1):41–48.

Shams, Shahriar, Kashif Mahmud, and Md. Al-Amin. 2011. "A Comparative Analysis of Building Materials for Sustainable Construction with Emphasis on CO2 Reduction." *International Journal of Environment and Sustainable Development* 10 (4):364. https://doi.org/10.1504/IJESD.2011.047767.

Sheikh, H R, and Alan C Bovik. 2006. "Image Information and Visual Quality." *IEEE Transactions on Image Processing* 15 (2):430–44. https://doi.org/10.1109/TIP.2005.859378.

Shepp, L. A., and B. F. Logan. 1974. "The Fourier Reconstruction of a Head Section." *IEEE Transactions on Nuclear Science* 21 (3):21–43. https://doi.org/10.1109/TNS.1974.6499235.

Siau, John Finn. 1984. *Transport Processes in Wood. Springer Series in Wood Science.* Vol. 2. Springer Series in Wood Science. Berlin, Heidelberg: Springer Berlin Heidelberg. https://doi.org/10.1007/978-3-642-69213-0.

Smith, Tait S., Brian K. Bay, and Mark M. Rashid. 2002. "Digital Volume Correlation Including Rotational Degrees of Freedom during Minimization." *Experimental Mechanics* 42 (3):272–78. https://doi.org/10.1177/001448502321548346.

Stoeckel, Frank, Johannes Konnerth, and W. Gindl-Altmutter. 2013. "Mechanical Properties of Adhesives for Bonding Wood — A Review." *International Journal of Adhesion and Adhesives* 45:32–41. https://doi.org/10.1016/j.ijadhadh.2013.03.013.

Strauss, W. 2000. "Digital Signal Processing." *IEEE Signal Processing Magazine* 17 (2):52–56. https://doi.org/10.1109/79.826412.

Suhonen, Heikki, Feng Xu, Lukas Helfen, Claudio Ferrero, Pavel Vladimirov, and Peter Cloetens. 2012. "X-Ray Phase Contrast and Fluorescence Nanotomography for Material Studies." *International Journal of Materials*

Research (Formerly Zeitschrift Fuer Metallkunde) 103 (2):179–83. https://doi.org/10.3139/146.110664.

Thielemans, Kris, Charalampos Tsoumpas, Sanida Mustafovic, Tobias Beisel, Pablo Aguiar, Nikolaos Dikaios, and Matthew W. Jacobson. 2012. "STIR: Software for Tomographic Image Reconstruction." *Physics in Medicine and Biology* 57 (4). IOP Publishing:2006–8. https://doi.org/10.1088/0031-9155/57/4/867.

Time, Berit. 1998. "Hygroscopic Moisture Transport in Wood." Norwegian University of Science and Technology. http://www.ivt.ntnu.no/docs/bat/bm/phd/AvhandlingBeritTime.pdf.

Tozzi, Gianluca, Enrico Dall'Ara, Marco Palanca, Marco Curto, Federica Innocente, and Luca Cristofolini. 2017. "Strain Uncertainties from Two Digital Volume Correlation Approaches in Prophylactically Augmented Vertebrae: Local Analysis on Bone and Cement-Bone Microstructures." *Journal of the Mechanical Behavior of Biomedical Materials* 67:117–26. https://doi.org/10.1016/j.jmbbm.2016.12.006.

Tran, H., Pascal Doumalin, C. Delisee, Jean Christophe Dupré, J. Malvestio, and A. Germaneau. 2013. "3D Mechanical Analysis of Low-Density Wood-Based Fiberboards by X-Ray Microcomputed Tomography and Digital Volume Correlation." *Journal of Materials Science* 48 (8). Springer US:3198–3212. https://doi.org/10.1007/s10853-012-7100-0.

Treeby, Bradley E., and B. T. Cox. 2010. "K-Wave: MATLAB Toolbox for the Simulation and Reconstruction of Photoacoustic Wave Fields." *Journal of Biomedical Optics* 15 (2). International Society for Optics and Photonics:21314. https://doi.org/10.1117/1.3360308.

Vine, D. J., D. Pelliccia, C. Holzner, S. B. Baines, A. Berry, I. McNulty, S. Vogt, A. G. Peele, and K. A. Nugent. 2012. "Simultaneous X-Ray Fluorescence and Ptychographic Microscopy of Cyclotella Meneghiniana." *Optics Express* 20

(16). Optical Society of America:18287.
https://doi.org/10.1364/OE.20.018287.

Vogelgesang, Matthias, Tomas Farago, Thilo F. Morgeneyer, Lukas Helfen, Tomy dos Santos Rolo, Anton Myagotin, and Tilo Baumbach. 2016. "Real-Time Image-Content-Based Beamline Control for Smart 4D X-Ray Imaging." *Journal of Synchrotron Radiation* 23 (5). International Union of Crystallography:1254–63.

Wang, Zhou, Eero P. Simoncelli, and Alan C. Bovik. 2003. "Multiscale Structural Similarity for Image Quality Assessment." In *Signals, Systems and Computers, 2004. Conference Record of the Thirty-Seventh Asilomar Conference on*, 2:1398–1402.
https://doi.org/10.1109/ACSSC.2003.1292216.

Zanaga, Daniele, Folkert Bleichrodt, Thomas Altantzis, Naomi Winckelmans, Willem Jan Palenstijn, Jan Sijbers, Bart de Nijs, et al. 2016. "Quantitative 3D Analysis of Huge Nanoparticle Assemblies." *Nanoscale* 8 (1). Royal Society of Chemistry:292–99.

Zauner, Michaela, Daniel Keunecke, Rajmund Mokso, Marco Stampanoni, and Peter Niemz. 2012. "Synchrotron-Based Tomographic Microscopy (SbTM) of Wood: Development of a Testing Device and Observation of Plastic Deformation of Uniaxially Compressed Norway Spruce Samples." *Holzforschung* 66 (8):973–79. https://doi.org/10.1515/hf-2011-0192.

Zauner, Michaela, and Peter Niemz. 2014. "Uniaxial Compression of Rotationally Symmetric Norway Spruce Samples: Surface Deformation and Size Effect." *Wood Science and Technology* 48 (5). Springer Berlin Heidelberg:1019–32.
https://doi.org/10.1007/s00226-014-0658-8.

Zhang, Lin, Lei Zhang, Xuanqin Mou, and David Zhang. 2011. "FSIM: A Feature Similarity Index for Image Quality Assessment." *IEEE Transactions on Image Processing* 20 (8):2378–86. https://doi.org/10.1109/TIP.2011.2109730.

9   APPENDICES

9.1 Statistical sample size analysis for single laps shear study

One of the questions in Chapter 3, was whether there is no effect of the adhesive penetration on the bond performance or if it was just overshadowed by the variability of the wood. Assuming that the shear drop metric is a valid measure of bond performance, G*Power (Faul et al. 2007) was used to compute *a priori* the necessary sample size to observe the measured multiple linear regression effect of both EP and WP together on the shear drop for each wood species and also the group of 14 specimens with 95% confidence. This computation is shown in Figure 9.1, and the estimated required sample size is 39. However, the minimum detectable effect for k, the shear drop coefficient, as a function of EP or WP separately is also plotted as a function of number of samples in Figure 9.2 and Figure 9.3.
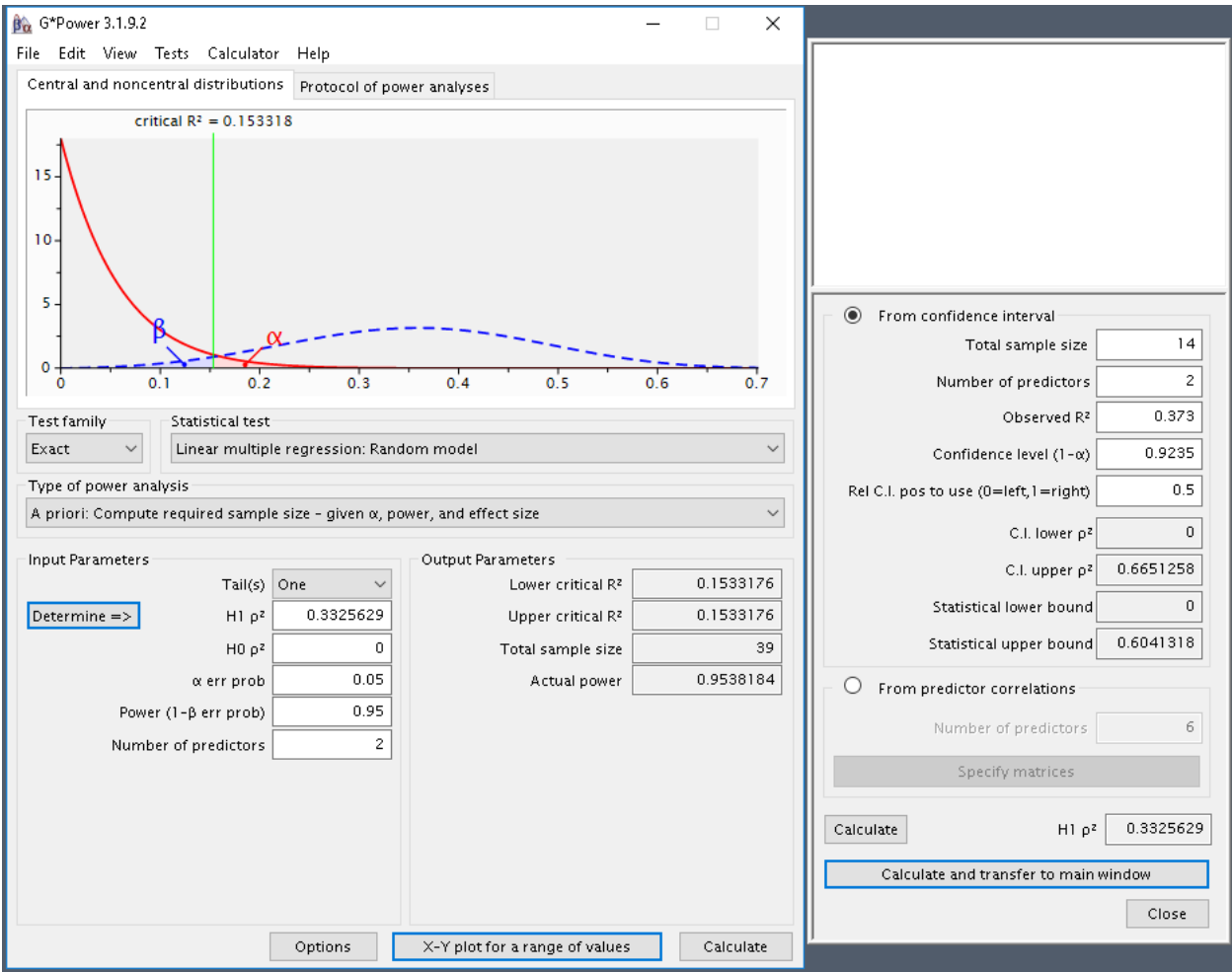
9.1.1 Figures

Figure 9.1 Panel showing computation of possibly required sample size for lap-shear experiment to observe an effect.
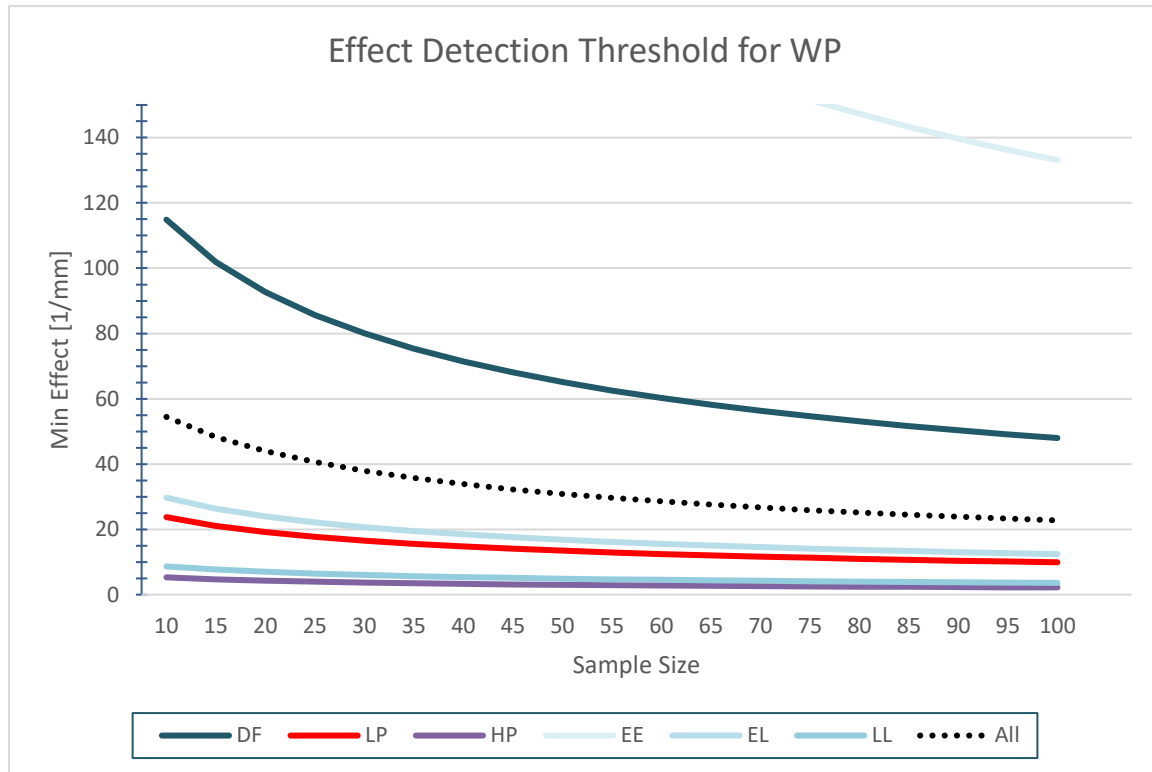
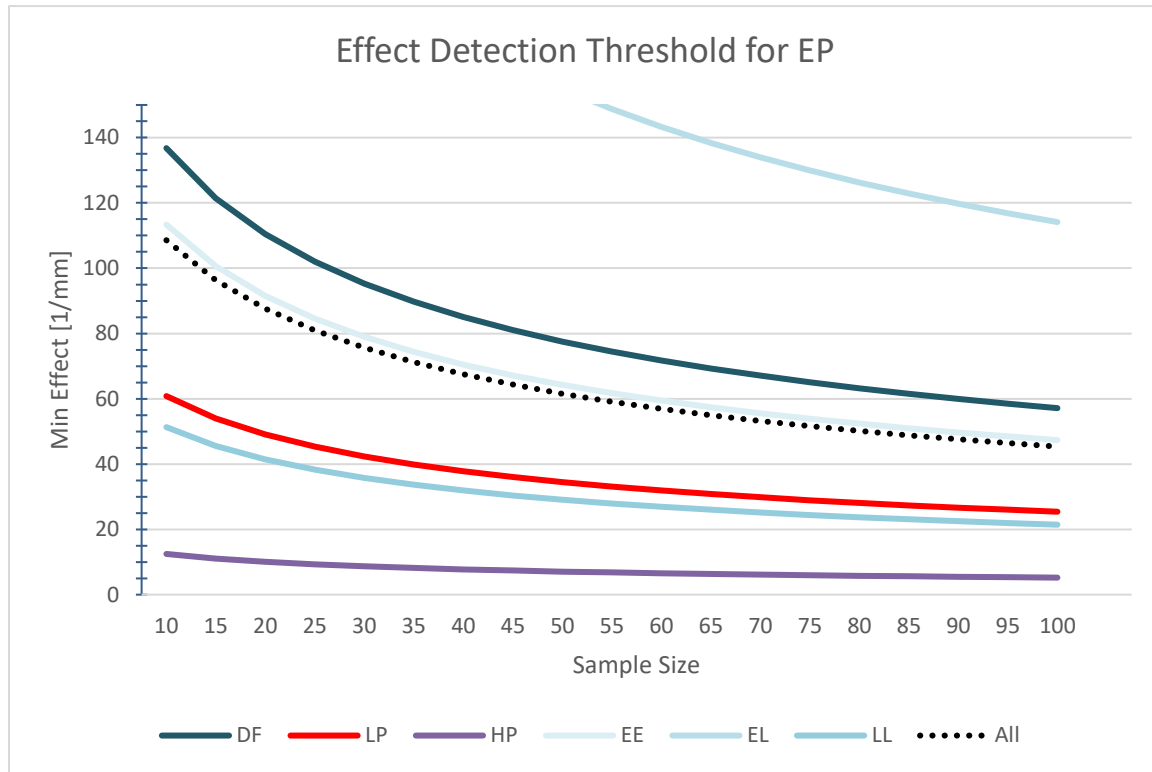Figure 9.2 Minimum detectable effect vs sample size calculated by G*Power for WP.

Figure 9.3 Minimum detectable effect vs sample size calculated by G*Power for EP.

9.2 Comparing methods for quantifying the load transfer performance of the adhesive bonds

9.2.1 Introduction

We are interested in rating the interfacial properties of the single lap shear specimen from specimen geometry and strain measurements of the specimen alone. The stress inside a specimen and the interfacial properties cannot be directly measured; only the strain distribution in response to an applied load can be measured. Three methods were proposed for evaluating the bond performance in Section 3.2.5, but they were given without proof of their efficacy. However, by modeling specimens with known interfacial properties, a more meaningful link between the observed strain distribution in a single lap shear specimen and the properties of the interface may be established.

In this appendix, some preliminary material point method (MPM) simulations were conducted to compare the proposed metrics for rating the interfacial properties of single lap shear specimens using only measured strains.

9.2.1.1 Single-lap shear bond performance metrics

Gindl-Altmutter, Müller, and Konnerth (2012) investigated specimen size effects and adhesive stiffness on the measured shear strength of specimens using the stress concentration factor (SCF), the ratio between the peak stress and minimum stress inside the overlap (Equation 3-1). They assumed linear elastic behavior and used their strain measurements to directly compute the SCF. Their strain measurements were collected from the surface of their specimens using electronic speckle pattern interferometry (ESPI) which is like image correlation, but the pattern is generated by using lasers to track the movement of surface roughness. The reasoning behind this metric may be that bonds with a lower stress concentration factor are better because distributed

stresses instead of concentrated stresses are less likely to cause failure. For this modeling work, the distance between the peak and minimum strain between the notches will also be used as metric; this metric will be referred to as the period.

Another work measuring the strain distribution at the notch of a single lap shear specimens using image correlation was conducted by Schwarzkopf and Muszyński (2015); this study proposed using the shear strain histogram around the notch as a metric for bond quality (Equation 3-2). Specimens whose distributions have less material with strains above some threshold are deemed more efficient. This reasoning is like that of Gindl-Altumutter et al. (2012), in that higher strains are bad, but in this case, the threshold is absolute instead of relative.

The metric proposed in this dissertation is the exponential coefficient from a power law equation, k, fitting the shear strain, ε_{xy}, drop from the notch in a single lap shear to the center of the lap (Equation 3-5). The power law was fit to the mean of the shear strains within 0.5 mm of the bond plane. Although this parameter enables a comparison between specimens of the same dimensions, it hasn't been calibrated, compared against any meaningful parameters of bond cohesion, or proven to be a good metric. Thus, it is impossible to say what size of change in k is meaningful if at all.

9.2.1.2 Previous computational models of single-lap wood composites

Previous work has modeled single laps of wood using finite elements (Gereke, Hering, and Niemz 2016). In this work, variations of the annual ring angle, the fiber angle, and the elasticity and thickness of the interface zone were tested to see if they influenced the stresses occurring in the adhesive bond line. Most relevant to this study is that they made changes to the elasticity of the adhesive and interface (interphase) zone; however, the finite element model they used was not capable of modeling imperfect interfaces. Instead,

they had perfect interfaces with a discrete adhesive region. In the present model, the interphase is not modeled, but the adherence of the interface is imperfect.

9.2.2 Material Point Method Model Description

MPM was chosen as a model because it provides opportunity for imperfect interface modeling and, arguably, better damage mechanics than FEA. MPM also offer plastic yielding. The ability to model an imperfect interface is important because this property is essentially what we are trying to measure in the real bonds. Also, MPM offers the ability, in the future, to increase the complexity of the model from uniform solid materials to cellular structure.

The measurement spacing for digital image correlation used in Chapter 3 for data was 0.02 mm, and the correlation window size was about 0.15 mm. Therefore, a grid size of 0.1 mm for the MPM model seems to be an appropriate match for the scale of the MPM model and the image correlation measurements. The simulations were conducted on a 1.5 GHz AMD A6-3420M APU with Radeon HD Graphics and 6GB RAM. Grid sizes smaller than 0.1 mm would overrun the java heap during visualization and take longer than 30 minutes to complete. A grid size vs computation time analysis for this laptop computer is shown in Figure 9.4.

The present model (Figure 9.5) approximates the single lap shear specimens used for the study in Chapter 3. The virtual specimen has 1 mm thick adherends and a 5 mm overlap. The adherend total length is 12 mm. Each notch is 0.5 mm wide. The lap is off center by 1 mm because that is how specimens were mounted in the specimen holders for the real experiment described in Chapter 3. In this 2D model, the x-axis runs along the bondline, and the origin is in the center of specimen. However, the origin is not in the center of the lap because of the offset. Material parameters for the wood are

shown in Table 1. Values were estimated from the Wood Handbook values for coastal Douglas-fir.

The analysis mode is plane strain MPM with GIMP and USAVG. Motion is damped to prevent oscillation because the experiment is supposed to be quasi-static. The right clamp moves at 0.5 m/s until it reaches a maximum displacement of 0.05 mm. This motion in the simulation is orders of magnitude faster than the real experiment because shortening the simulation shortens computation time. Regardless of the unreal loading speed, the model still may be effectively quasi-static the material properties of the Douglas-fir. The clamps are modeled as rigid materials. The model uses contact material mode between the two wood adherends to simulate the imperfect interface. The interface is characterized by two interface parameters, normal traction, D_n and tangential traction, D_t. These can range from zero, a debonded interface with no tractions, to infinity, a perfect interface (J. A. Nairn 2013). The interface in these models has a perfect normal traction, but tangential traction varies between models. Simulations were conducted with D_t ranging from 10^3 to 10^{18}, then the resulting strain fields were analyzed.

9.2.3 Results and Discussion

The average shear strain within ± 0.1 mm of the bondline for different magnitudes of D_t is shown in Figure 9.6 as a function of position along the x-axis. The left edge of the chart is the center of the overlap; the right notch is at 2 mm. The simulations show a different behavior of strain at the interface for low and high tangential traction and a transition between the two behaviors around 10^{11}. Similar plots from the real specimens (Figure 3.6b), mostly have strain distributions like those where $D_t \geq 10^{11}$. Models where D_t is less than 10^{11} show the shear strain dipping below zero near the notch before rising again towards the center of the overlap. This difference in behavior between low and high tangential traction interfaces was unexpected as was the non-differentiable

shape of the strain distribution; however, it is not impossible. Because the sign of the shear strain flips on opposite sides of the interface and the sample is non-symmetric, the negative shear areas may comprise most of the ± 0.1 mm region of interest immediately before the notch. Clearly the region of interest choice is influential, and perhaps, a larger region of interest may provide a better metric.

Each of the proposed metrics was applied to the data of the modeled specimens. The *power law shear drop metric, k,* is shown in Figure 9.7. This metric picks up the transition of the interface traction from low to high, so it is possibly useful for separating specimens into low and high traction categories. In this case, low traction specimens would have a *k* of around 10^4 and high traction specimens would have a *k* of around 10. However, there is ambiguity in the transition region since *k* does not increase or decrease monotonically with the traction parameter of the interface. Assuming this metric can be used to sort specimens into high and low traction, then all the specimens in Figure 3.7 would be high traction.

The *stress concentration factor* (SCF) and *period* are shown in Figure 9.8; we will define the *period* as the distance between the minimum strain and peak strain used to calculate the SCF. The SCF also does not correlate well with the traction because it doesn't monotonically increase or decrease. The *period* seems to be monotonically increasing with the tangential traction because the minimum strain point moves from the notch to the center of the lap as the traction increases, but it also has a sharp transition from the low to high traction behavior. Like the power law metric, the SCF divides the models into two regimes: low and high traction. However, in this case, it is even harder to divide the specimens because the SCF ratings are all within the same magnitude.

The third proposed metric (Matthew Schwarzkopf and Muszyński 2015) requires counting the fraction of points in histograms above a threshold. This metric was reformatted as a cumulative density function (CDF). Because choosing a threshold is arbitrary, we can look at all possible thresholds by looking at the CDF instead. Figure 9.9 shows that this method may be the most promising one; if you choose a high enough threshold, the models may be ordered by interface traction. Additionally, the behavior of the two CDFs is unique between the high and low traction. There are some caveats however: because this method uses absolute strains, all the specimens must be measured at the same displacement or load and the shape of the CDF depends on the size of the region of strains that are included.

9.2.4 Conclusions

Simulations of single lap shear specimens with different tangential interface traction parameters were run. The shape of the shear strain distribution was unexpected. It consists of two regimes of behavior: low and high traction. Low traction characterized by a non-differentiable minimum in the shear strain adjacent to the maximum shear strain at the notch.

Next, three types of metrics were applied to the data to determine whether they can predict the interface traction. Although all the metrics can show the difference between 'low' and 'high' traction interfaces, only the CDF based metric appeared to be a good predictor of the traction parameter because it could be used to plausibly order specimens according to their interface traction.

Further research is needed to determine how to best apply the CDF based metric including what area of the specimens should be included in the analysis and whether it applies in 2D. One caveat is that these metrics were tested on a simulation of equivalent crosshead displacements. They should be tested on simulations with the equivalent loads as well.

9.2.5 Future Work

The interface could also be modeled with a crack. In personal correspondence with John Nairn in 2017 he said that sometimes his cracks model does normal contact better because it uses a different method than was used here.

Single lap shears specimens experience peel stresses (stress perpendicular to the bond) in addition to shear stresses at the interface because the non-symmetric loading causes a moment. Thus, an logical extension would be to make D_n imperfect in tension but perfect in compression (i.e., nonlinear). Peel stress might affect bond performance and could be important for these metrics.

9.2.6 Tables

Table 9.1 Material properties used for Douglas-fir in this model.

Douglas-fir Properties	
E_x [Pa]	1.08E+10
E_y [Pa]	7.34E+08
E_z [Pa]	5.40E+08
G_{xy} [Pa]	6.91E+08
G_{xz} [Pa]	8.42E+08
G_{yz} [Pa]	7.56E+07
yieldxx [Pa]	3.45E+07
yieldyy [Pa]	1.73E+07
yieldzz [Pa]	1.73E+07
nu_{xy}	0.292
nu_{xz}	0.449
nu_{yz}	0.39
rho [kg/m^3]	530

9.2.7 Figures
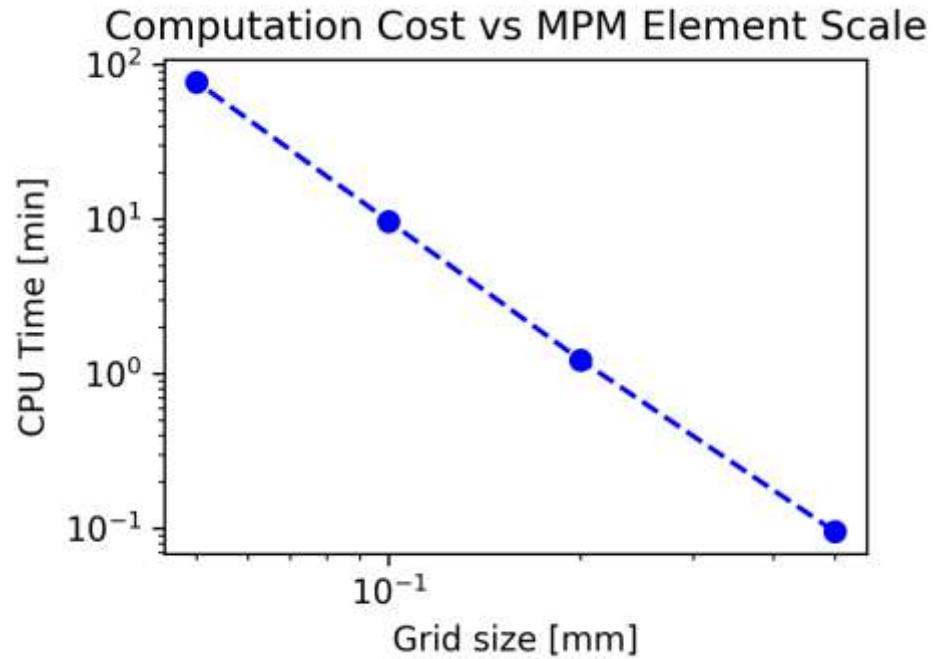
Figure 9.4 The computational cost of running the MPM model in Figure 9.5 on four 1.5 GHz cores at different grid sizes.
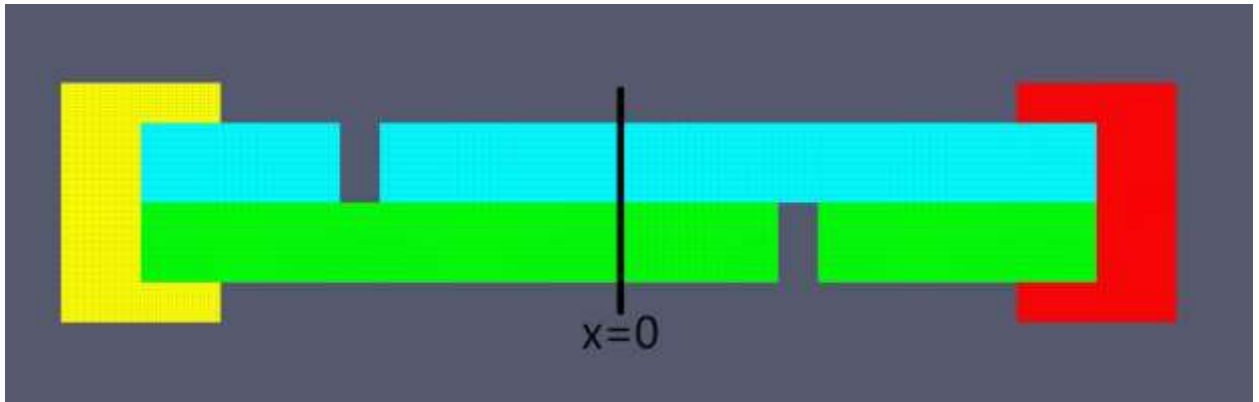
Figure 9.5 The MPM model of the single lap shear specimens. Two adherends (blue, green) are connected by an imperfect interface. Two rigid materials (yellow, red) pull on the adherends in tension. Position x = 0 matches with the position in Figure 9.6.
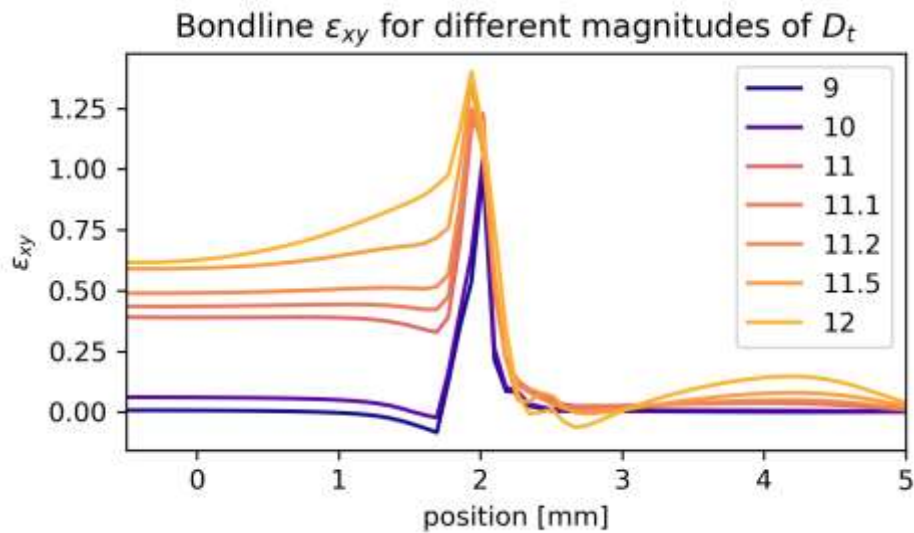

Figure 9.6 Plot of the shear strain, ε_{xy}, along the interface between the adherends at different magnitudes of the tangential traction, D_t. Magnitudes are powers of 10.
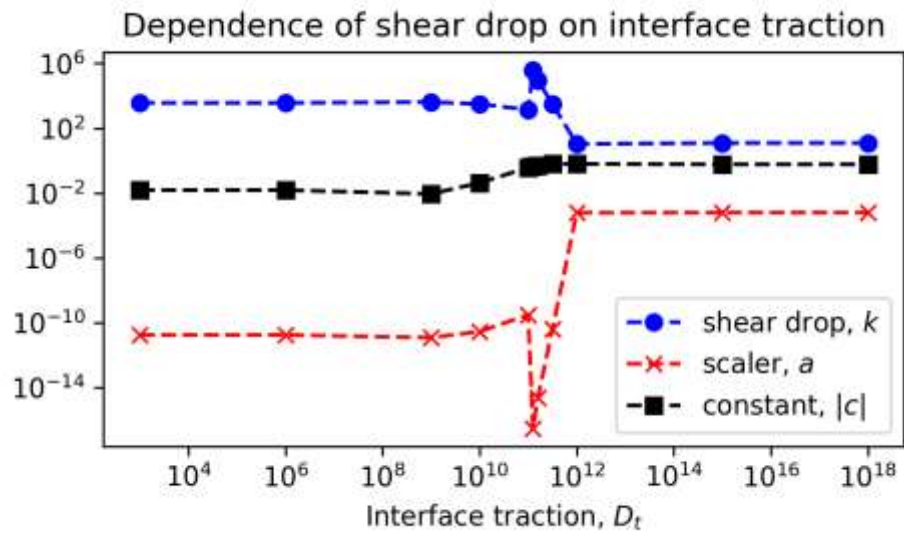
Figure 9.7 Components of the power law shear drop fit to the MPM model at different magnitudes of tangential traction.
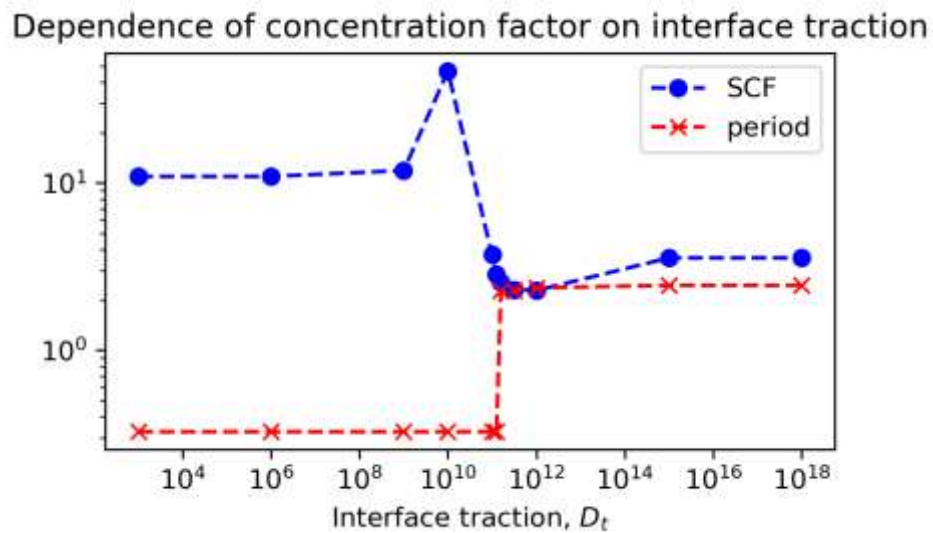

Figure 9.8 Stress concentration factor and the period (distance) between the minimum and maximum shear strain in the MPM model as a function of interface traction.
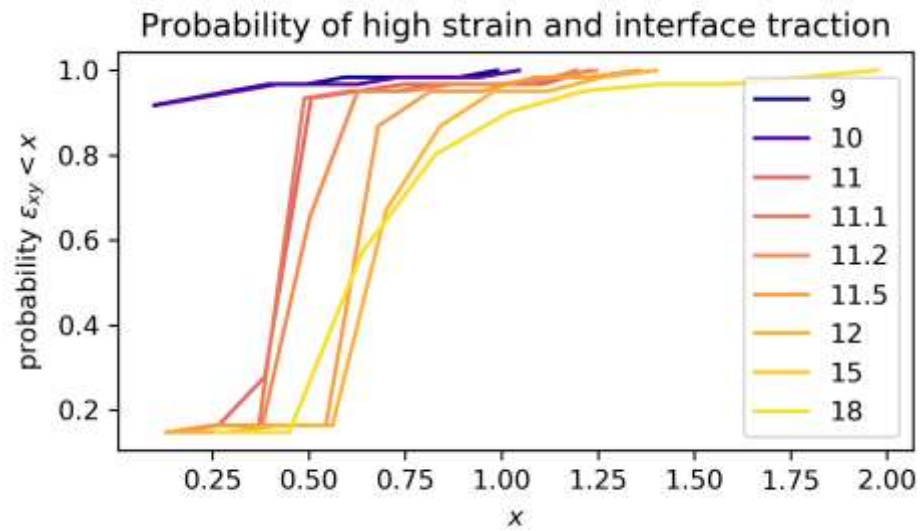
Figure 9.9 Cumulative distribution of strain between -2 mm and 3 mm along the interface for various orders of magnitude of interface traction.